Contribution à la modélisation biofidèle de l'être humain par la prise en compte des interactions fluide-structure

Benoît Fontenier

Thèse de doctorat

Pour obtenir le grade de Docteur de l'Université de

VALENCIENNES ET DU HAINAUT CAMBRESIS

Discipline : Génie Mécanique

Présentée et soutenue par Benoît, FONTENIER.

Le 01/12/2016, à Valenciennes

Ecole doctorale :

Sciences Pour l'Ingénieur SPI

Laboratoire :

Laboratoire d'Automatique, de Mécanique et d'Informatique Industrielles et Humaines (LAMIH)

Contribution à la modèlisation biofidèle de l'être humain par la prise en compte des interactions fluide-structure

JURY

Rapporteurs

- Ruben, Rui Miguel Barreiros. Professeur Institut Polytechnique de Leiria.
- Lefrançois, Emmanuel. Professeur. UTC Compiègne.

Examinateurs

- Verlinden, Olivier. Professeur. Faculté Polytechnique de Mons (Président du jury)
- Richert, Julien. Docteur. Daimler Sindelfingen
- Naceur, Hakim. Professeur. LAMIH Valenciennes
- Hault-Dubrulle, Audrey. Maitre de conférence. LAMIH Valenciennes

Co-directeurs

- Drazetic, Pascal. Professeur. LAMIH Valenciennes
- Fontaine, Christian. Professeur. Université Lille 2

Si vous trouvez que l'éducation coûte cher, essayez l'ignorance.

Abraham Lincoln

Acknowlegments

Dans un temps, je souahite remercier touts les membres du juri qui ont accépté de prendre part à ces travaux. Les discussions que nous avons pu avoir ont été très enrichissantes m'ont permis d'avoir une vision plus large plus sujet.
Après trois années, la fin de la thèse est un moment propice pour regarder derrière soi, prendre conscience du travail accompli et remercier tous les acteurs.

Ces trois années ont été effectuées sous la direction de Messieurs les Professeurs Pascal Drazetic et Christian Fonataine. Je remercie Pr.Pascal Drazetic pour toute la confiance et la liberté qu'il m'a laissé. Il est une chance que d'avoir un directeur comme Pr Christian Fontaine, directeur du laboratoire d'anatomie de Lille 2 et chirurgien, il a apporté à cette thèse un regard extérieur affuté, ses questions toujours pertinentes m'ont permis de garder un esprit critique envers mes travaux, pour cela je vous remercie.

Deux personnes ont assuré un suivi proche de ces travaux, Professeur Hakim Naceur et Docteure Audrey Hault-Dubrulle. Je remercie Audrey qui, a toujours été présente pour répondre à mes appréhensions, doutes et interrogations. Je suis revenu d'Allemagne pour travailler avec le Pr Hakim Naceur, jamais déçu de nos discussions toujours très instructives je n'ai qu'un regret, qu'elles aient toutes une fin.

Certaines personnes ne sont pas officiellement impliquées mais ô combien importantes. Je remercie, le Docteur Remy Delille qui m'a permis d'effectuer de nombreuses manipulations expérimentales tout en me faisant réfléchir sur leurs bien-fondés. Je remercies sincèrement le Professeur Laurent Kreilsbulck et Monsieur Anthony Graziani qui m'ont permis d'acquérir de réelles connaissances dans le domaine de la mécanique des fluides sans quoi cette thèse aurait été bien plus fade.

Dans ce laboratoire de nombreuses personnes m'ont laissé leur prendre du temps afin de discuter sur des sujets diverses, au delà de satisfaire ma curiosité scientifique, elles ont apportées à ces trois années bon nombre de soutiens et de plaisirs. Pour cela je pense notamment à remercier les Drs Christophe Maréchal, Frédéric Robache, Hervé Morvan, Cédric Hubert, Michel Watremez, Pr Franck Lauro ainsi que Monsieur Denis Lesueur.
La partie administrative ne peut être évitée, mais devient tellement plus agréable lorsque nous

travaillions avec Mesdames Catherine Foucart et Sabine Guilain que je remercie.

La thèse est un bateau dans lequel nous ne sommes pas seul à tirer des bords et ramer. J'ai toujours pu compter sur mes compagnons de voyage : Julie Chalon, Kevin Lemercier, Jérémy Wouts, Andrès Malo-Estepa, Maxime Baligant, Dr Colin Debras, Dr Yannick Senecaut, Manaf Karkar, Amina Laouira.
La thèse est un exercise dans lequel de façon égoïste nous impliquons nos proches. Je ne remercierai donc jamais assez ma femme Sandra Wosynski mon frére et ma soeur, Antoine et Marie Fontenier.
Enfin, la thèse est l'aboutissement un travail de longue haleine, celui de nos parents que je tiens à remercier chaleureusement pour leurs soutiens et leur aide inébranlable.

Abstract

The purpose of this work is to improve the biofidelity of the human body models. The work is focused on the human head as it is one of the most injured part. In order to improve the traumatic brain injury onset and mechanism, the biofidelity of the head models has to be increased, thus, the fluids embedded inside the head has to be taken into account. Nevertheless, the modelling of the interactions occurring between the viscous corporal fluids and the soft matter as the brain remains a challenge. This study intends to investigate the fluid-structure interactions between a soft structure and a fluid.

Firstly, in order to found the most relevant methods to solve the problem, a deep literature survey has pointed-out all the numerical methods available nowadays.

Secondly, in a previous PhD work an experimental test has been carried-out to demonstrate the influence of the cerebrospinal fluid on the brain kinematics under dynamical load case. On one hand, the Silicon Sylgard 527 gel used as brain substitut has been characterized . Subsequently the partitioned coupling methods available in LS-Dyna ICFD have been assessed to model the experiment. Although, the previous characterized gel model has been used, the experiment has been unsuccessfully completed. Accordingly, it has been decided to develop an in-house coupling code.

Thirdly, a partitioned coupling code has been developed. It is a middleware in C++ between two well establishing solvers OpenFOAM and LS-Dyna respectively for the fluid and the solid. Because there is very few experimental tests for the coupling code validation, it has been carried-out in this work a fluid-structure interaction experiment involving a soft plate in a wind channel. This appealing experiment allows the scientific community to validate easily their coupling algorithms. Subsequently, the developed coupling code is used to model the wind channel.

The results depict a good overall agreement between the experiment and the simulation. Nonetheless, in order to get validated results further investigation are required mainly about the flow modelling.

Résumé

Ces travaux visent à améliorer la biofidélité des modéles virtuels de l'être Humain. Les statistiques montrent que la tête humaine est fréquemment sujette à des traumatismes cérébraux, des lésions et autres blessures. Une attention particulière sera donc donnée à la modélisation de la tête. Afin de mieux prédire les mécanismes lésionnels de la tête, la biofidélité des modèles doit être améliorée, pour cela les effets du fluide situé à l'intérieur de la tête doivent être pris en compte. Cependant, la modélisation des interactions entre un fluide corporel visqueux et un matériau mou comme le cerveau reste un verrou scientifique. Il est proposé d'étudier en détail la modélisation des interactions fluide-structure entre un fluide et un corps mou.

Premièrement, un étude bibliographique détaillée sur les méthodes numériques de modélisation des interactions fluides-structure a permis d'évaluer chacune d'elles et de juger de celle qui est la mieux adaptée pour la résolution de la problématique.

Deuxièmement, lors de travaux de thèse précédents, une expérience a été réalisée montrant l'influence du liquide cérébrospinal sur la cinématique du cerveau lors d'un chargement dynamique. Cette expérience est utilisée dans un premier temps pour caractériser numériquement le gel silicone Sylgard 527 utilisé comme substitut de cerveau. Dans un second temps des méthodes de couplage partitionnée disponible dans le code commercial LS-Dyna ICFD sont utilisées pour modéliser l'expérience. Bien que les modèles de gel précédemment caractérisés ont été utilisés, la version avec fluide n'a pas pu être modélisée avec succès.

Troisièmement, un code de couplage partitionné est donc développé. Il consiste en un middleware écrit en C++ couplant deux codes éprouvés, OpenFOAM et LS-Dyna pour la modélisation du fluide et du solide respectivement. De plus, parce que très peu d'essais expérimentaux utilisables pour la validation de code d'interaction fluide-structure sont disponibles dans la littérature, une expérience permettant cela a été réalisé dans une soufflerie.

La comparaison des prédictions numériques avec les résultats expérimentaux sont prometteurs et donnent des résultats globaux satisfaisants. Les points qui ne peuvent pas être validés nécessitent de plus amples investigations et permettront d'améliorer les techniques de modélisations et le développement du code.

Contents

1 Introduction

The injury was defined by [Baker, 1992] as a wound "resulting from acute exposure to various kinds of energy: mechanical, thermal, electrical, chemical or radiant in amounts that exceed the threshold of physiologic tolerance". This definition was used by [Ricard et al., 2010] who categorized the injuries in two groups, the intentional and unintentional. The unintentional injuries represent 4% of total deaths in France and can be divided in three groups: the work accidents, the road accidents and the life accidents. All statistics given in this section deal with the metropolitan France and are based on the works of the "Institut de veille sanitaire" and the "Observatoire national interministériel de la sécurité routière".

The work accidents count for 1,000 deaths per year. Furthermore, among the 10-12 millions of estimated life accidents occurred each year [Ricard et al., 2010], 5 millions of hospitalisations and 20,000 deaths per year are recorded. Two-thirds of life accidents involve people older than 75 years often because of falls and remain the first cause of death for the people younger than 15 years.

The road accident statistics were carried-out by the European law of August 09, 2016. It reported the number of hospitalisations which require more than 24 hours and the number of deaths which happened during the first thirty days. Following the report [Salathé and Rosseau, 2015] subsequently to a continuous reduction, the number of hospitalisations and deaths has increased in 2015, with 27,715 hospitalisations and 3,616 deaths. Based on the results of [Salathé and Rosseau, 2015], figure 1.1 highlights an overview of the repartition of human body wounded parts for the most vulnerable people. The selection criterion of injuries is the belonging to the fourth and upper level of the international traumatic scale the "Abbreviated Injury Scale" (AIS). It can be observed that the head of the pedestrian and cyclist is particularly subjected to injuries while the thorax of the motorcyclist is the most frequently

injured. For the motorcycles, the head protection is highly performed by the helmets, this explains why the head is not the most injuried body part.

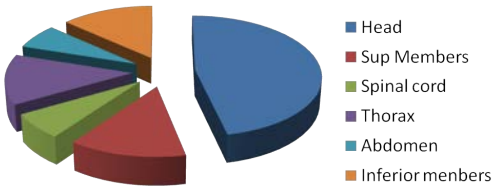

(a) Pedestrian

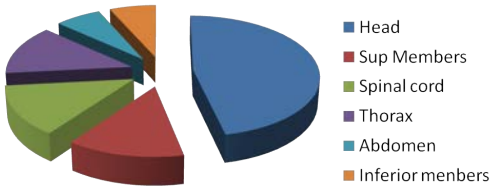

(b) Cyclist

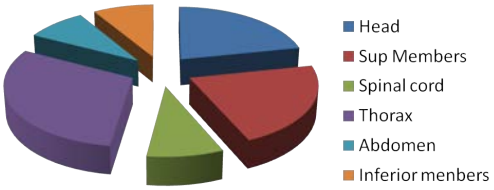

(c) Motorcyclist

Figure 1.1: Wounds repartition for various road users

The age is also an important factor. Road traffic users who are between 18 and 29 years old sustain the highest amount of death and hospitalisation. For the 18-19 years old, 136 deaths and 994 hospitalisations per million of habitants have been reported in 2015 which is largely higher that the national average.

Injuries sustained are a real social burden regarding the number of death and all the disabilities resulting from the unintentional injuries. In addition the injuries are a real societal cost. The number of interventions, prevention campaigns and hospitalisations have to be supported by the society. Furthermore, owing to the disabilities, the people, often youth, can suffer from difficulties to continue to work in the same conditions and has to adapt all their daily life with particular house safety devices, car adaptation, transportation, etc.

In order to alleviate the number of injury several actions were undertaken. Concerning the life accidents, prevention campaigns to inform about the risks have been often published. In addition, houses are becoming more and more safe mainly for the elderly peoples with the possibility to make availability of numerous devices aimed to improve their safety. The traffic accidents and mainly the automotive crashes have attracted numerous researchers and

developments. The active and passive safeties are expanding over the last years such as the seatbelts or airbags.

Nevertheless, the development of the most optimal safety devices necessitate a deep understanding of the human body injury onset and the injury mechanisms. Accordingly to ethical issues, wounds cannot be imposed to living people, thus methods have to be developed. In the transport and more particularly in the automotive field the first studies aimed to understand the human body behaviour in case of automotive crash had been conducted using post-mortem subjects. Although the geometry of the body are well respected, the living ton of the human had not been taking into account. In addition, the tissue behaviour depicts a great evolution between living people and post-mortem subjects. As, a critical issue is the specificity of the experiment as each body involves specific geometry and material properties furthermore once the body has been injured it cannot be reused.

Lately a second method has been used, the human subject is substituted by dummies. The surrogate is constant regarding the geometry as well as the material properties. But dealing with the dummies the experiments is still being not easily reproducible as the automotive structure is out of order after the crash test. In addition, it is not able to show accurately the local behaviour of biological organs or tissues and thus the injury assessment of specific parts is still a challenge. Nonetheless, the dummies remain today a choice widely used by car manufacturers for the prediction and the validation of their vehicles regarding the norms like the US-NCAP or EURO-NCAP.

The most recent method used in the safety research field is the numerical modelling of human body. The numerical models lead to assess the human body behaviour in both a globally and a locally manner, thus the onset of the injuries can be observed. The geometry can be accurately fitted. In addition, the numerical models overcome the repeatability issues and even more can perform various loading conditions and parametric studies readily. Nevertheless, the full biofidelic human body models are still not fully developed and certain issues have to be still studied to improve biofidelity at a highest degree. One possibility to improve the numerical modelling is the introduction of the corporal fluid effects. In fact the human body in constituted of approximately 60% of water, the related effects have therefore to be taken into account on the local and global behaviours. The fluid is found in large quantity in the whole body; the heart and the related vascular circulation, the lungs with the air breathing

but also the head and the bone marrow are only some instances of biomechanical situations involving fluid-structure interactions.

The objective of this work is to contribute to improve the accuracy of parts of the human body model predictions. As, the human head is one of the most injured part, it has been chosen to be studied. The numerical human head models are improved by enhancing fluid structure interactions dealing with viscous fluid and soft material which are respectively in the head the cerebrospinal fluid and the brain matter. In order to find the most adapted modelling technique, a detailed description of the fluid-structure interactions modelling methods available nowadays in the literature will be presented in chapter 2.

In chapter 3, in order to asses the playing role of the fluid inside the head structure under dynamical load cases an experiment has been carried-out in a previous PhD work. This experiment has been used in two situations without water and with water: firstly a very soft silicon gel has been used as brain matter substitute, its mechanical characterization is completed by a special developed characterization method. Secondly, using the previous gel model, the fluid-structure interactions are modelled dealing with viscous fluid and soft matter. It has been shown that the instabilities can be avoided by using commercial solvers and the development of a in-house computational coupling code has been undertaken.

In chapter 4, the in-house coupling code is developed using two well known fluid and structure codes, respectively OpenFOAM and LS-Dyna. In order to validate the first step of this new coupling code and to overcome the lack of experiments for the coupling code validation, a fluid-structure interaction experiment especially designed for the code validation has been carried-out in a wind channel.

2 Fluid-structure interaction modelling methods

Contents

2.1 Introduction

The LAMIH laboratory of the university of Valenciennes investigated since several years the development of a numerical model of the human body. This numerical human body model aims to take into account the inter and intra diversities, and has to be enable to be customised. The human body model is developed towards accidentology and traumatology applications. This problematic has already been studied through several PhD works [Delille, 2002], [Delille, 2007], [Auperrin, 2009], [Mayeur, 2013], [Bry, 2015], [Vandenbulcke, 2015].

In this context, each of the model parts have to be as biofidelic as possible, i.e. it must mimics the behaviour of the real living tissues, organs, bones,... . In order to be as biofidelic as possible, several studies have pointed out the necessity to take into account the corporal fluids as there are important interactions between the fluid and the living tissues [Halgrin, 2009], [Rungen, 2004], [Hault-Dubrulle, 2007].

Nonetheless, the understanding and the modelling of such phenomenon is still not mastered. Firstly because the living tissues are non-linear and could be viscous. Secondly, the fluid flows sustained often dynamical load cases. Finally, the coupling of the fluid and solid are multi-field and multi-scale problems involving important interactions. The modelling of such interactions is still a challenge.

The modelling of the fluid-structure interactions is the main focus of this thesis. In order to give a global survey and accurate explanations of the fluid-structure interactions, this chapter is divided in six sections. The formulation of the fluid-structure problems is presented. Because the problem involves several media, various descriptions of continuum are employed and thus each of them are detailed. The coupling schemes are then investigated, the spatial and temporal coupling techniques available nowadays are explained. Finally, the applications and validation tests currently found in the literature are detailed.

2.2 Fluid-structure problem formulations

The coupling problems involve a fluid and solid parts. Each media is monitored by the mass continuity and the momentum equations, in addition a constitutive equation is added regarding the material. Because the two media interact together, data has to be transferred. This data exchanges are carried-out by a set of coupling conditions which are detailed hereafter.

The solid domain is called Ω_s, the fluid domain is Ω_f. They are separated by the fluid structure interface Γ_{fs} called wet boundary (see Figure 2.1)

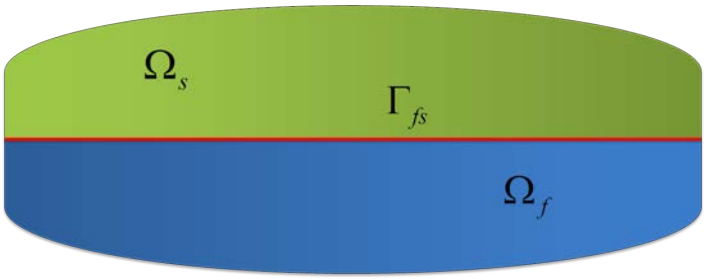

Figure 2.1: Fluid structure domains

2.2.1 Solid equations

The governing equations for a linear elastic isotropic material are expressed by the equations 2.1,2.2, 2.3 and 2.4.

$$\frac{d\rho_s}{dt} + \rho_s div\overrightarrow{V_s} = 0 \tag{2.1}$$

$$\rho_s \frac{d^2\overrightarrow{U_s}}{dt^2} = \overrightarrow{div}\overline{\overline{\sigma_s}} + \rho_s \overrightarrow{f} \tag{2.2}$$

$$\overline{\overline{\sigma_s}} = \lambda Tr\left(\overline{\overline{\epsilon_s}}\right)\overline{\overline{I}} + 2\mu\overline{\overline{\epsilon_s}} \tag{2.3}$$

$$\overline{\overline{\epsilon_s}} = \frac{1}{2}\left(\overline{\overline{grad}}\overrightarrow{U_s} + \overline{\overline{grad}}^T\overrightarrow{U_s}\right) \tag{2.4}$$

where $\rho_s, U_s, V_s, \overline{\overline{\sigma_s}}, \overline{\overline{\epsilon_s}}, \overrightarrow{f}$ are respectively the density, the displacement, the velocity, the stress tensor, the infinitesimal strain tensor and the external forces of the solid. The linear elastic isotropic material is defined by the lamé constants λ and μ.

If the equation 2.3 is injected is the equation 2.2 the Navier equations are derived as:

$$\rho_s \frac{d^2\overrightarrow{U_s}}{dt^2} - (\lambda+\mu)\overrightarrow{grad}\left(div\left(\overrightarrow{U_s}\right)\right) - \mu\overrightarrow{\Delta}\overrightarrow{U_s} - \rho_s\overrightarrow{f} = \overrightarrow{0} \tag{2.5}$$

In order to be able to solve the problem, boundary and initial conditions have to be added.

2.2.2 Fluid equations

The governing equations for a Newtonian fluid are expressed by the following set of equations 2.6, 2.7, 2.8, 2.9 and 2.10.

$$\frac{d\rho_f}{dt} + \rho_f div\overrightarrow{V_f} = 0 \tag{2.6}$$

$$\rho_f \frac{d\overrightarrow{V_f}}{dt} = \overrightarrow{div}\overline{\overline{\sigma_f}} + \rho_f \overrightarrow{f} \tag{2.7}$$

$$\overline{\overline{\sigma_f}} = -p_f \overline{\overline{I}} + \overline{\overline{\tau}} \tag{2.8}$$

$$\overline{\overline{\tau}} = 2\nu_f \left(\overline{\overline{\epsilon_f}} - \frac{1}{3} Tr\left(\overline{\overline{\epsilon_f}}\right) \overline{\overline{I}} \right) \tag{2.9}$$

$$\overline{\overline{\epsilon_f}} = \frac{1}{2} \left(\overrightarrow{\overline{\overline{grad}}} \overrightarrow{V_f} + \overrightarrow{\overline{\overline{grad}}}^T \overrightarrow{V_f} \right) \tag{2.10}$$

where $\rho_f, V_f, \overline{\overline{\sigma_f}}, \overline{\overline{\epsilon_f}}, \overrightarrow{f}$ are respectively the density, the velocity, the stress tensor, the strain tensor and the external forces of the fluid. The Newtonian viscous fluid is described by the Stockes law where τ is the deviatoric stress.

If equations 2.8 and 2.9 are injected in equations 2.7 the Navier-Stockes equations can be stated as:

$$\rho_f \frac{d\overrightarrow{V_f}}{dt} + \overrightarrow{grad}\left(p_f\right) - \nu_f \overrightarrow{\Delta} \overrightarrow{V_f} - \frac{1}{3} \nu \overrightarrow{grad}\left(div\left(\overrightarrow{V_f}\right)\right) - \rho_f \overrightarrow{f} = \overrightarrow{0} \tag{2.11}$$

In order to complete this equations, boundary and initial conditions have to be included. In addition, in the case of a compressible fluid an additional state equation linking the pressure

variation and the fluid density is required.

2.2.3 Coupling conditions

In the fluid-structure problems, the fluid and the solid are driven by the Navier-Stockes and the Navier equations respectively. Additionally, the fluid and structure behaviours are coupled by a set of coupling conditions.
Upon the wet boundary the local equilibrium is enforced by the dynamical coupling condition which states that:

$$\overline{\sigma_s}\,\overrightarrow{n} - \overline{\sigma_f}\,\overrightarrow{n} = \overrightarrow{0} \tag{2.12}$$

where $\overrightarrow{n} = \overrightarrow{n_f} = \overrightarrow{n_s}$ $\overrightarrow{n}$ is the external normal of the wet boundary λ_{fs}.
Secondly, the kinematic condition states that the fluid and the solid have the same motion, through the wet boundary as neither gap nor overlap can appear, their velocities are therefore enforced to be matching.

$$\overrightarrow{V_s} - \overrightarrow{V_f} = \overrightarrow{0} \tag{2.13}$$

If the fluid is assumed to be inviscid, the kinematic coupling condition is imposed only along the normal direction as:

$$\overrightarrow{V_s}\,\overrightarrow{n} - \overrightarrow{V_f}\,\overrightarrow{n} = 0 \tag{2.14}$$

Thus the normal velocities remains equal and no gap nor overlap can appear but only the tangential parts of the fluid velocity is free to flow.

The resolution of the coupling problems implies to the resolution of differential equations which cannot be solve analytically, thus only numerical methods may be used. One crucial point of the numerical methods is the kinematic description of the continuum.

2.3 Kinematic formulations

When a numerical computational code is either developed or simply used, the description of the Kinematics is a key element which has to be investigated and carefully adapted to the modelling of physical phenomenon. Three kinematic formulations are used: the Lagrangian, the Eulerian and the Arbitrary Lagrangian Eulerian (ALE) formulations. In this section each formulation is described and the governing equations are expressed in the appropriate formulation.

2.3.1 Lagrangian

In the Lagrangian description the particular derivatives are simply turned into partial derivative, i.e. $\frac{d}{dt} = \frac{\partial}{\partial t}$, thus the mass continuity 2.1 and the Navier equations 2.5 of a solid in the Lagrangian description are respectively

$$\frac{\partial \rho_s}{\partial t} + \rho_s div \overrightarrow{V_s} = 0 \tag{2.15}$$

$$\rho_s \frac{\partial^2 \overrightarrow{U_s}}{\partial t^2} - (\lambda + \mu) \overrightarrow{grad} \left(div \left(\overrightarrow{U_s} \right) \right) - \mu \overrightarrow{\Delta} \overrightarrow{U_s} - \rho_s \overrightarrow{f} = \overrightarrow{0} \tag{2.16}$$

The Lagrangian description associates one material particle on each node which is tracked during the motion. This method allows to know the displacement history for each material particle and to follow accurately the interfaces between several materials. However, when the situation deals with important displacements, the mesh cells sustain large distortion and cannot provide further accurate results. Then, in spite of the method is time efficient, one or several remeshing procedures may be necessary. The Lagrangian method is well suited for the structural modelling.

2.3.2 Eulerian

In the Eulerian description the particular derivative involves the material velocity V_f in a convective term, i.e. $\frac{d}{dt} = \frac{\partial}{\partial t} + \left(\overrightarrow{V_f} \cdot \overrightarrow{grad} \right)$, thus the fluid mass continuity equation 2.6 and the Navier-Stockes equation 2.11 in the Eulerian description are stated as follows: equations 2.17

and 2.18

$$\frac{\partial \rho_f}{\partial t} + \left(\overrightarrow{V_f} \cdot \overrightarrow{grad}\right) \rho_f + \rho_f div \overrightarrow{V_f} = 0 \tag{2.17}$$

$$\rho_f \frac{\partial \overrightarrow{V_f}}{\partial t} + \rho_f \left(\overrightarrow{V_f} \cdot \overrightarrow{grad}\right) \overrightarrow{V_f} + \overrightarrow{grad} p_f - \nu_f \overrightarrow{\Delta} \overrightarrow{V_f} - \frac{1}{3} \nu_f \overrightarrow{grad} \left(div \left(\overrightarrow{V_f}\right)\right) - \rho_f \overrightarrow{f} = \overrightarrow{0} \tag{2.18}$$

Contrary to the Lagrangian formulation, the Eulerian formulation is well adapted to the flow modelling. It is composed of a fixed grid and leads the media to flow trough the cells. The very large deformations could be therefore easily investigated whereas the tracking of the interfaces need additional works. Finally, all the material laws based on the deformation history cannot be used because the history of the material is unknown.

The previous conclusions about the kinematics of the continuum media could be used to achieve a modelling strategy of fluid-structure interactions. Indeed, regarding the deformation sustained by the fluid, it is clear that it is not relevant to use the Lagrangian formulation. Nevertheless, the Eulerian formulation is not efficient because an accurate interface between both medias must be tracked. A third formulation had been therefore developed called "Arbitrary Lagragian Eulerian"(ALE).

2.3.3 Arbitrary Lagrangian Eulerian

According to the pointed-out restrictions, a third fundamental description attempting to take into account the advantages of the Lagrangian and Eulerian formulations is completed by [Donea et al., 1982], [Hughes et al., 1981],[Hirt et al., 1974], [Margolin, 1997]. This description is called "Arbitrary Lagragian Eulerian"(ALE) method and is widely employed in the fluid structure interactions modelling.

The particular derivative in the ALE description involves the mesh velocity V_m and the material velocity V_f in a convective term, i.e. $\frac{d}{dt} = \frac{\partial}{\partial t} + \left(\left(\overrightarrow{V_f} - \overrightarrow{V_m}\right) \cdot \overrightarrow{grad}\right)$, thus the mass continuity equation 2.6 and the Navier-Stockes equation 2.11 in the ALE description are rewritten as

follows, equations 2.19 and 2.20.

$$\frac{\partial \rho_f}{\partial t} + \left(\left(\overrightarrow{V_f} - \overrightarrow{V_m}\right) \cdot \overrightarrow{grad}\right) \rho_f + \rho_f div \overrightarrow{V_f} = 0 \tag{2.19}$$

$$\rho_f \frac{\partial \overrightarrow{V_f}}{\partial t} + \rho_f \left(\left(\overrightarrow{V_f} - \overrightarrow{V_m}\right) \cdot \overrightarrow{grad}\right) \overrightarrow{V_f} + \overrightarrow{grad} p_f - \nu \overrightarrow{\lambda} \overrightarrow{V_f} - \frac{1}{3} \nu_f \overrightarrow{grad} \left(div \left(\overrightarrow{V_f}\right)\right) - \rho_f \overrightarrow{f} = \overrightarrow{0} \tag{2.20}$$

The basic principal of the ALE method is to purpose a formulation wherein the mesh velocity is not restricted to a binary choice: either equal to zero (Eulerian point of view) or equal to the material velocity (Lagrangian point of view). As a matter of fact, the ALE method is a generalisation of the two previous descriptions. Hence the ALE method is restricted to the Lagrangian one, the mesh velocity must be equal to the material velocity, i.e. $V_m = v_f$. In addition, the convective velocity is zero, i.e. no convective terms appeared in the conservatives law in a Lagrangian description. Conversely, if the grid velocity is imposed to be equal to zero, i.e.$V_m = 0$, an Eulerian approach is carried out and the convective velocity is the material velocity. Nonetheless usually, the mesh velocity is neither the material velocity nor equal to zero but is rather computed by special algorithms which will be investigated in the paragraph 2.5.2.

2.4 Fluid-structure modelling

2.4.1 Monolithic

Using the above governing equations the resolution of the fluid-structure problem may be studied.

The most reliable approach is to solve the coupled system monolithically. The monolithic approach treats the fluid, the solid and the continuity conditions in the same mathematical framework. It means that all the FSI equations are merged in a single set of equations which are solved simultaneously. In order to be able to complete the resolution, it is highly recommended to deal with the same discretization method in space as well as in time for the two media: Finite Volume method, finite difference method, finite element method, ALE or

fictitious domain could be cited among others. Commonly, the finite volume is used for fluid modelling, but some authors applied for structure [Demirdžić and Martinović, 1993]. The finite element method is usually used for structure modelling but some authors applied it for fluid modelling [Donea et al., 1982] and[Hughes et al., 1981]. The equations, lead to solve a non-linear problem including the computation of residuals by means of a Newton algorithm. Therefore a global fluid-structure matrix has to be inverted. Although the interface conditions are implicitly achieved, the matrix inversion is highly consuming time as the matrix is large and the computation/inversion of the Jacobian is not straightforward.

The monolithic approach is the most robust and stable method as shown in the figure 2.2 adapted from [Razzaq, 2011]. It can achieve better accuracy and make reference for some problems. In [Heil et al., 2008], using a benchmark which can be more or less strongly coupled the authors show that the monolithic can be more robust than other approaches. In the literature several works can also be found where the monolithic approach depicts good agreement: [Michler et al., 2004], [Hubner et al., 2004], [Ryzhakov et al., 2010] and [Greenshields and Weller, 2005].

Unless these advantages, the development of the code handles high developments knowledges. The code updates are not easily achieved. Furthermore all the resolution is written in only one code, this leads to get a non flexible code. Finally, the fluid time step is much smaller than the solid one to handle accurately some physical phenomenon like turbulence or vortex shedding. The computation time is then long because the monolithic approach does not allow to use two different time steps.

In order to counterbalance some of the previously cited drawbacks another method can be used to solve fluid-structure interactions problems called, the partitioned method (see Figures 2.3 and 2.2).

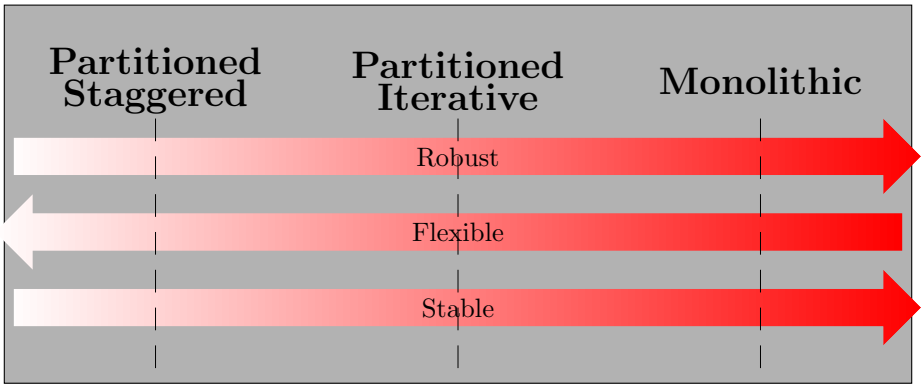

Figure 2.2: Performances of fluid-structure interactions coupling approaches

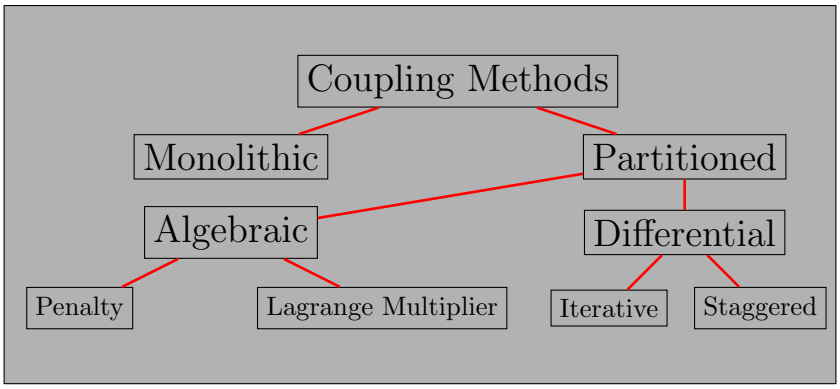

Figure 2.3: Fluid-structure interactions coupling approach classification

2.4.2 Partitioned

Unlike the above monolithic approach, the partitioned approach splits the fluid-structure interactions problem in two sub-problems. Nowadays, numerous efficient numerical techniques have been developed for the modelling of the fluids and the structures. The basic idea of the partitioned methods is to take advantages of all these developments, and used already developed and well-established computational codes as black boxes. The fluid and the structure are solved separately with their respective mesh discretizations and numerical algorithms and are coupled together in space and in time. An general overview of the main parts of the partitioned coupling scheme is given.

Computational fluid dynamics The computational fluid solves the partial differential equations to move during time the fluid and writes the pressures encountered on the wet boundary.

Computational structural dynamics The computational structural code reads the pressure produced by the fluid on the wet boundary then solves the partial equations to move during time the structure and writes the displacement or the velocity of the structure.

Spatial coupling interface The spatial coupling interface assures the transfer of the fluid's pressure to the solid and the solid's displacements to the fluid mesh. It plays a key issue mainly if the discretizations of the fluid and solid are different. It has to be independent of the fluid and solid computational code and of the time coupling. Once the solid motion is transferred

to the fluid mesh on the wet-boundary, the spatial coupling is in charge of the fluid mesh update.

Time coupling interface The time coupling interface insures the information exchange in time between the two solvers. The accuracy, the stability and efficiency of the coupling is very dependent on the time coupling. In addition, the time coupling has to be well established regarding whether the physical phenomenon is weak or strong.

The resolution of a fluid-structure problem using a partitioned method is usually referred as a three fields problem, the fluid computation, the solid computation and the mesh motion. In fact, when a liquid flows around a structure, the pressure applied on the structure causes its deformation. On the same time, the deformation of the structure induces a deformation of the flow geometry. Numerically, the fluid computational move the fluid assuming a wet boundary position. The pressure enforced by the fluid on the structure through the wet boundary are read and turn into forces. The forces are used as constant loads applied to the structural computation which updates the structure and thus the wet-boundary. But the fluid mesh has to fit the structure mesh. The displacements of the structure are therefore read and used to update the fluid mesh to accommodate it to the new wet boundary position. The mesh update is completed by the third procedure, the mesh motion.
Thus, the best combination of numerical techniques can be used for each specific investigation. Moreover, no constraints remains on the time steps, so that, the fluid time step can be smaller than the structure time step. The challenge is therefore to transfer the informations between fluid and structure codes and to keep a stable, accurate and efficient modelling (see Figure 2.2). The coupling methods in space and in time available nowadays in the literature are detailed in the next sections.

2.5 Spatial coupling

As previously pointed-out using the partitioned coupling method, the fluid-structure interaction problems are treated as two separated sub-domains of a close system (see Figure 2.1). Each of the sub-domain is computed by different algorithms and interacts through boundary conditions exchange. At any time the global close system has to be equilibrated regarding the

energy balance, thus the information transfer has to fulfill several criteria: the global energy conservation, the global loads conservation, the accuracy, the efficiency [De Boer et al., 2007]. The first challenge of the partitioned method is the spatial information transfer.
A fluid-structure interaction problem requires the transfer of the dynamical coupling condition equation 2.12, i.e. the pressure, from the fluid to the solid and the transfer of the kinematic couplig condition eq 2.13, i.e. the structural motion to the fluid mesh. Depending to the solid and fluid discretizations two situations can be distinguished, the Boundary Fitted methods and the Non-Boundary Fitted methods. In this section the different two spacial discretizations are presented.

2.5.1 Boundaries fitting method

The spatial discretizations

When the two media are split in two separated meshed sub-domains following their natural decomposition, the situation is called Boundary Fitted method. Dealing with partitioned coupling scheme, the boundary fitting method is very attractive as the wet-boundary is clearly observed and easily identified by the algorithms. Despite this easiness, various situation can occur according to the spatial discretization type and discretization size.
The discretization size is always a discussed issue because it could lead to errors if it is not well adapted to the situation. The discretization of the wet-boundary can be conforming or non-conforming. If the fluid and solid meshes have the same node positions along the interface, the meshes are then conforming (see Figure 2.4a). Nevertheless, the conforming meshes can be very constrained mainly in most real applications where the two sub-domains do not need the same discretization, e.g. the boundary layer of a fluid need to be very fine if the turbulences are modelled or because the two sub-domains are not created by the same analyst. If the two meshes do not match, they are non-conforming (see Figure 2.4b). Such meshes lead to additional drawbacks as the creation of gaps and overlaps which require further efforts toward the information exchange. This work adopts the general fluid-structure interaction resolution point of view found in the literature. The fluid mesh is always finer that the solid mesh and the meshes are thus non-conforming.

In this work, the fluid is discretized by the finite-volume (FV) method while the solid discretization is based on the finite-element (FE). This restrictions are done because the finite-volume

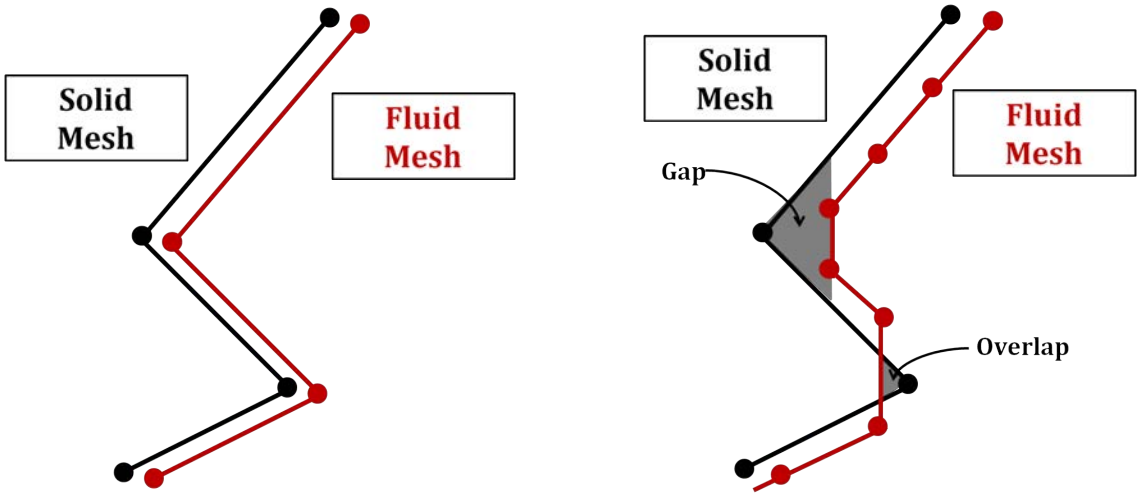

(a) Conform mesh (b) Non conform mesh

Figure 2.4: Discretization size

for the fluid and the finite-element for the solid have proven their respective efficiency. Accordingly, nowadays most of commercial, academic and open source codes are based on the above discretizations. For the finite-elements, the displacements and velocity are expressed on the nodes whereas the stress is expressed based on the Gauss quadrature points. The finite-volume is here co-localized, i.e. the displacements and velocities of the mesh are expressed on the grid nodes while the pressure of the flow are assumed constant over the cell and expressed on the cell centers. However, the cell center values can be readily interpolated on the cell's face centers.

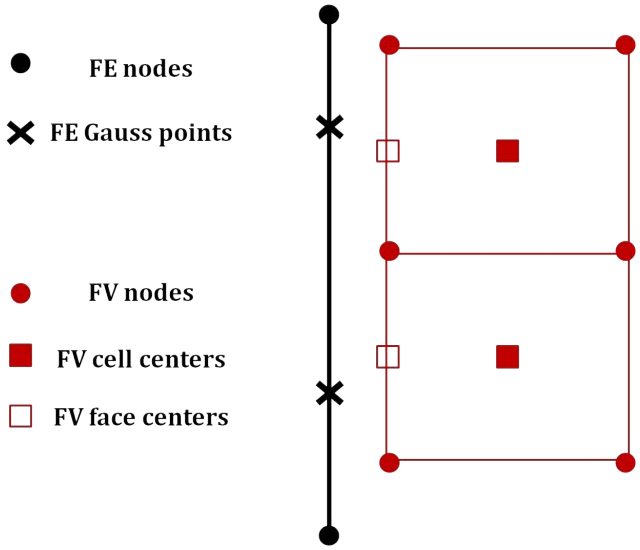

Figure 2.5: Discretization types: FE and co-localized FV

Spatial coupling methods

The information transfer is readily completed when the meshes are conformed. In fact, the *Nearest point* [De Boer et al., 2007] method is used whether the meshes are conformed or nearly conformed. In order to transfer informations from fluid to solid, the algorithm takes a fluid node and seeks for the nearest solid node. Once the two nodes are pairing, all the data of the fluid is transferred to the solid node. The conversely way, i.e. from solid to fluid is carried-out on the same manner.

Nevertheless, the non-conforming meshes require more efforts to perform an accurate transfer and is therefore the topic of the next section.

Transfer of the solid motion to the fluid mesh The methods aim to transfer the structural node displacements or velocities to the fluid grids. The first method belongs to the "point-to-element" methods commonly used because of its simplicity [Farhat et al., 1998]. It consists in creating a point(different from a node) which is the orthogonal projection of the fluid nodes on the solid elements. Subsequently, the motion of the point is assessed by shape functions of the structural elements. According to the figure 2.6 based on [Casadei and Potapov, 2004] the velocity V_{s*} (or displacement) of the point can be expressed by equation 2.23.

$$V_{s*} = \sum_{i=1}^{n} N_{S_i}(S^*) \cdot V_{s_i} \tag{2.21}$$

where n is the number of nodes of the structural element. $N_{S_i}(S^*)$ is the shape function of

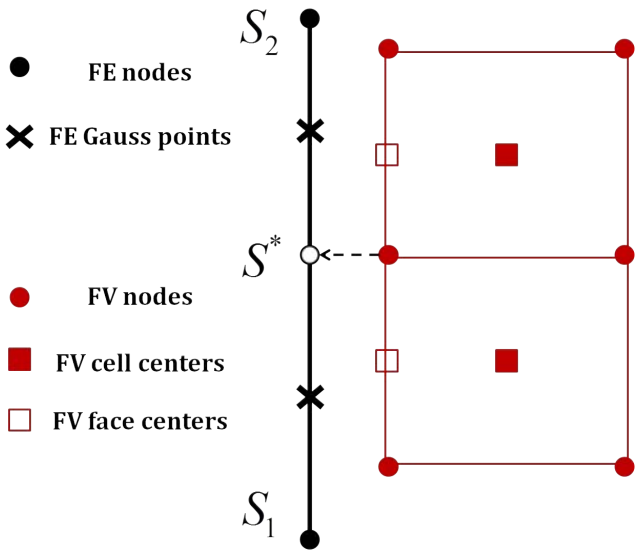

Figure 2.6: Transfer of solid motion to fluid mesh: Point-to-element method

the structural element evaluated at the point S^*.

The second method belongs to the *point-to-point* methods also known as Radial Basis Function (RBF) method, which known a growing importance with meshless methods. The data transfer is directly carried-out from a node to an other by create an approximation function f defined on the already known n values of f_c evaluated at the control points x_{c_i}. Based on the works [Lombardi et al., 2013] the value of a function f assessed at a approximated point x using the radial basis function is expressed as 2.22.

$$f(x) = \sum_{i=0}^{n} \gamma_i \phi \left(|x - x_{c_i}| \right) + q\left(x\right) \tag{2.22}$$

where γ_i is the weight coefficient, q a polynomial and $\phi\left(|x - x_{c_i}|\right)$ a given radial basis function based on the distance between the interpolated point x and the control points x_{c_i}. The most used radial basis functions are the one including compact support [Beckert and Wendland, 2001] or the Multi-quadratic biharmonic splines and the thin-plate splines used by [Smith et al., 2000]. In order to transfer the solid motion to the fluid mesh, the control points are the structural nodes whereas the interpolated points are the fluid grids nodes.

Transfer of the fluid load to the solid mesh The methods aim to transfer the pressure induced by the fluid into forces on the solid mesh. The first method called "consistent interpolation method" presented in [Farhat et al., 1998]. The structural finite-element method computes the stress on the Gauss points. The principle of the method is thus to pair each Gauss point of a solid element to a fluid cell (see Figure 2.7). The value of the pressure of the fluid can be computed by any interpolation methods. Despite the method is attractive by its simplicity, it is shown that it is not ever conservative of the energy because the final load is computed based on the interpolations related upon both discretizations, the fluid and the solid.

In order to improve the energy balance of the first method, [Farhat et al., 1998] proposed and used a second method already investigated in the paragraph 2.5.1 as the "point-to-element" method. In this way, as pointed-out in the figure 2.8 the fluid nodes are projected to the structural elements, then based on the shape function of the finite element, the value of the forces

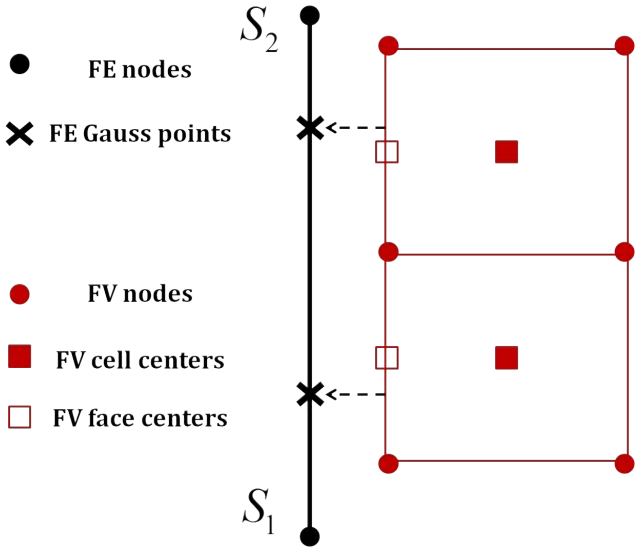

Figure 2.7: Transfer of fluid load to solid mesh: Gauss point and fluid cell pairing

on the structural node can be estimated by:

$$f_{s_i} = \sum_{j=1}^{n} N_{S_i}\left(S^*j\right) \cdot \Phi_{S_j^*} \tag{2.23}$$

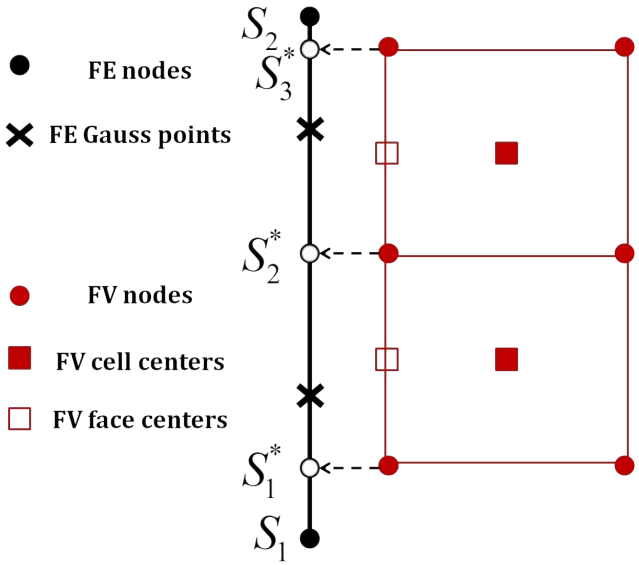

Figure 2.8: Transfer of fluid load to solid mesh: Point-to-element method

where n is the number of node on the fluid element. $N_{S_i}\left(S^*j\right)$ is the shape function of the structural element evaluated at the point S^*j. $\Phi_{S_j^*}$ is the numerical pressure estimated at the point S^*j.

Finally, the RBF presented in the paragraph 2.5.1 allows to transfer the fluid load to the solid

mesh. In this way the interpolated points are the structural nodes and the control points are the fluid face centers.

2.5.2 Mesh update procedure

Once the structural motion is transferred to the wet-boundary of the fluid mesh, the deformation located on the wet-boundary has to be spread on the whole fluid mesh to avoid that the deformations may localize on the first fluid cell's range. Generally, the grid near the wet-boundary behaves like a Lagrangian grid whereas the mesh far from the wet-boundary could stay fixed like an Eulerian mesh and between a transition zone has to be managed by the mesh update procedure. Because the mesh update procedure is often very time consuming, it is essential to choose the best suitable strategy. Several mesh update methods are therefore presented in the next paragraph.This procedure claims to impose at each grid nodes for each time step a displacement or a velocity.

Such methods aim to avoid the elements distortion, overlap or warped and are known as the *mesh regularisation* methods. The displacement of the wet-boundary is prescribed on the fluid mesh, the remaining nodes are moved by a smoothing procedure to smooth the whole mesh. The smoothing allows overcoming the concentration of the deformations around the first cells' range around the wet-boundary. All the smoothing procedures can be used to update the ALE grid. However, some of them are often found in the literature like the interpolation method used in [Suliman et al., 2015], [Song et al., 2013] where the displacements or velocities inside the mesh could be simply found by means of interpolations. Other mesh regularisation method are based on the Poisson equation resolution upon the coordinates or velocities initially proposed by[Winslow, 1963]. This method moves the node to fit the iso-values, of velocity. Several authors used this simple method, like [Zeng and Scovazzi, 2016] who recently used it for impact applications. Another popular method used in the fluid-structure for instance, [Zeng and Scovazzi, 2016] is called 'pseudo linear elastic" method. In this method the grid is regarded as a Lagrangian part enhanced by a material law wherein the displacement of a part of the grid is prescribed. The mesh update procedure is often time consumming, to improve its efficienty [Wood et al., 2010] purposed to use the method of the Delauney triangulation whereas [Hussain et al., 2011] proposed the sharing memory system using OpenMP system. When the domain sustained very large deformations, the grid is distorted leading to an increase of the computational cost and a decrease of the accuracy. In such a case a remesh involving a

topology evolution is advocated or unavoidable. This procedure is highly time consuming and shows the major boundary-fitting method limitations.

Although boundary-fitted method has been widely used in many fluid-structure problems [Matthies et al., 2006], [Farhat et al., 2006], [Matthies and Steindorf, 2002], the method has two main drawbacks, an expensive remesh procedure has to be undertaken when large deformations are enforced and the creation of the fluid mesh which must faithfully represent the structure geometry that can has very complex shape. It is the main reason that had prompted for the used of methods dealing with non-boundary fitting methods involving fixed fluid grids. Some authors tried to achieve non-boundary fitting method based on ALE. For instance, [Wick, 2013] developed a method based on the ALE called "Fluid structure interface tracking / interface capturing" allowing to deal with fully Eulerian and then fix fluid grid. This method is applied to a biomechanical valve [Wick, 2014]. [Codina et al., 2009] used also the ALE method but keeps the fluid mesh fix and turn the parameter's values on the fixed fluid grid. The principle to use the ALE description as a tool is used by [Troshin et al., 2015] to enhance the "Proper Orthogonal Decomposition" which initially depicts interesting results but only for fixed meshes.
The growing interest for the non-boundary fitting methods prompts to the development of special methods devoted for the fluid computation involving solid as in the figure 2.9. An overview of this methods is presented in the next section.

2.5.3 Non boundary fitting methods

In the previous section, it was pointed-out that the boundary-fitting methods were limited when dealing with the large deformations. In order to overcome this drawback, the non-boundary fitting methods were created (see Figure 2.9). Contrary to the boundary-fitting methods, the non-boundary fitting methods are composed of a fixed Cartesian fluid mesh which does not take into account the structure and overlaps it. The fluid problem may be treated in an ALE or an Eulerian framework whereas the structure is always treated in a Lagrangian description [Aquelet et al., 2006]. The fluid mesh does not required to fit the structure's boundaries, it could be therefore restricted to simple primitive shapes like square or cube. This advantage is worthwhile when industrial applications are carried-out because they engage often complex geometries.

Because there is no clear interface as the previous wet-boundary, the key challenge of such methods is to be able to define special conditions upon the fluid mesh to enable the fluid to "see" the structure and its evolution during the simulation. In order to achieve such a challenge, both method's families have been achieved, the *Continuous* forcing methods and the *Discrete* forcing methods.

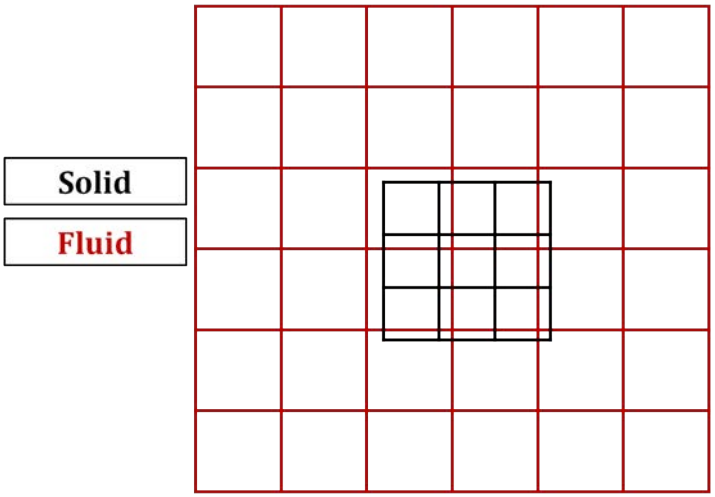

Figure 2.9: Non boundary fitting

Continuous forcing methods

The continuous forcing methods adds a source term called forcing term, in the right hand side of the Navier-Stockes equation to handle the effects of the structure. The modified Navier-Stockes equation is then dicretizied in the whole fluid domain by any numerical scheme. Some continuous forcing methods are described in the next paragraphs

Immersed Boundary Method The Immersed Boundary Method (IBM) was developed by Peskin in 1972 [Peskin, 1972] to simulate cardiac valves mechanism and the blood flow associated. The blood was considered like a Newtonian incompressible and viscous fluid. The structure immersed is represented by a collection of massless point belonging to a fibre and evolving in a Lagrangian framework. In order to take into account the structure, a source term f_b is added in the right hand side of the equation 2.11 which become:

$$\rho_s \frac{d\overrightarrow{U_f}}{dt} + \overrightarrow{grad}\,(p_f) - \nu_f \overrightarrow{\Delta}\overrightarrow{V_f} - \frac{1}{3}\nu \overrightarrow{grad}\left(div\left(\overrightarrow{V_f}\right)\right) - \rho_f \overrightarrow{f} = \overrightarrow{f_b} \text{ in } \Omega_f \tag{2.24}$$

The basis of the method is to move the structure's points at the same velocity than the fluid. The position of the K^{th} point denotes X_k is governed by the following equation:

$$\frac{\partial X_k}{\partial t} = v\left(X_k, t\right) \tag{2.25}$$

The relative point displacements lead to the computation of the structure deformation. Subsequently, using the Hook's law the stresses could be assessed also. The presence of a solid is then treated by the solid stresses.

Nevertheless, there is no assumption about the conforming between the fluid ans solid spatial discretization. In other words: there is not a priori a corresponding fluid node for each solid node. A distribution of the solid stresses has to be calculated on several fluid nodes around the solid node. This distribution is broadly set-up by a Dirac distribution.

$$f(x,t) = \sum_k F_k\left(t\right) \delta\left(\mid x - X_k \mid\right) \tag{2.26}$$

where δ is the Dirac function, F_k is the stress of the K^{th} solid node. In the equation 2.26 the term f is integrated in the Navier-Stockes equation 2.24 as a source term.

Because the fluid and the solid meshes are not conform, the solid node velocities theoretically expressed by the equation 2.25, are assessed on each node by the same approach.

$$\frac{\partial X_k}{\partial t} = \sum_k v\left(x,t\right) \delta\left(\mid x - X_k \mid\right) \tag{2.27}$$

Although the Dirac function solves the problem of the non-conforming meshes, its discretization poses a delicate issue. The Dirac function is a highly irregular function and needs to be approximated by a smoother function to be discretized. Thus, several approximations of the Dirac function are available in the literature as it is represented in the graph 2.10. Despite its relative easiness, the IBM suffers from some drawbacks. Leakage problems near the boundaries have been shown. Due to the leakages, it is possible for some fluid particles to move inside the solid domain. Some authors have proposed some improvements to fix this problem [Xu and Wang, 2006], [Peskin and Printz, 1993]. In addition to that, the IBM provides available results if the assumption of regular flow is respected however near the interfaces, the flow is quickly irregular and the IBM creates an artificial thick boundary layer, some improvements have been proposed, [Leveque and Li, 1994], [LeVeque and Li, 1997], [Li and Lai, 2001].

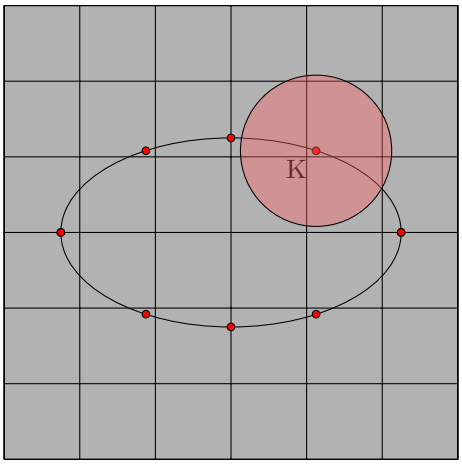

Figure 2.10: Distribution de Dirac

Euler-Lagrange penalty method Several kinds of fluid-structure coupling using penalty were developed, as for instance the method of penalisation by a porous media of Brinkkman [Angot et al., 1999]. However, the most useful is the Euler-Lagrange method.

The Euler-Lagrange method was developed notably to solve hydrodynamics problems. The basis of this method is to couple a slave real solid node with a master fictitious fluid node by a spring of stiffness k. The springs impose opposite forces F_f and F_s respectively on the fluid and on the solid nodes. The force penalises then the relative displacements.

Let V_s et V_f are the velocities of the solid and the fluid respectively and d_n the relative displacement, during a time step, the relative displacement is incremented by:

$$d^{n+1} = d^n + \Delta t \left(v_f^{n+\frac{1}{2}} - v_s^{n+\frac{1}{2}} \right) \tag{2.28}$$

If the relative displacement is known, the forces are expressed by:

$$F_s = -F_f = kd^n \tag{2.29}$$

In order to avoid vacuum creation, the forces are applied only if they compress the fluid. The choice of the spring stiffness is a challenge of this method. In fact, if the spring is too soft, the fluid can penetrate the solid. Conversely, if the stiffness is too high, the time step will be very small if a explicit temporal discretization is under consideration and if an implicit time discretization is used, the number of time step will increase dramatically to reach an equilibrium.

In [Aquelet et al., 2006] a spring damper system is proposed to reduce the non-physical

oscillations. Nevertheless, the value of the damper has to be characterized otherwise some physical phenomena could be over diffused.

Lagrange multiplier Contrary to the IBM, the fluid Fictitious Domain is discritized by finite element. Formerly using only for rigid body [Glowinski et al., 2141] [Glowinski et al., 1999] two evolutions [Baaijens, 2001] and [Yu, 2005] were proposed to treat the slender elastic and furthermore the non-slender elastic structures.
The Lagrange multipliers could be seen as pseudo forces and are involved across the solid body to include the coupling conditions. The main advantage of this method regarding the IBM method is to involve the solid effect into the variational formulation. Thus there is no need to approximate the Dirac function by a smoother function. Nevertheless, it can be time consuming because all the Lagrange multipliers have to be computed at every time-step.

The previously presented coupling methods need to asses a source term in the whole fluid domain to take into account the presence of the structure. Such methods showed an interesting efficiency if the flows involves a small or moderate Reynold's number. Nevertheless, if the Reynold's number becomes high, the turbulence phenomenon appear and the boundary layer effect cannot be neglected. The boundary layer is a local phenomenon located around the solid's interfaces. The previous methods introduce important diffusion effects and tunr to be enable to predict accurately the crucial boundary layers effects. Due to this limitation, some other methods called discrete methods are investigated with the objective to be more accurate locally.

Discrete forces methods

The discrete methods discretize the Navier-Stockes equation through the whole Cartesian fluid domain without regards on the structure. In a second step the position of the structure is detected. Subsequently, the computational strategy is modified around the structure in order to take it into account with sufficient accuracy. A description based on the works [Mittal and Iaccarino, 2005] and [Hovnanian, 2012] is undertaken in this section.

Ghost-Cell method The Ghost-Cell method is based upon the works of [Fadlun et al., 2000] and [Tseng and Ferziger, 2003]. The method adds forcing terms in the Navier-Stockes equation

of the *ghost cells* to impose implicitly the boundary condition on the interface. A ghost cell is then defined as a cell in the solid which has at least one neighbouring in the fluid as the cell "G" in the figure 2.11. For the problem dealing with fluid-structure interaction, a velocity is often prescribed on the fluid to get the correct velocity on the fluid-structure interface. Nonetheless, any value Φ can be enforced to be used in this method.

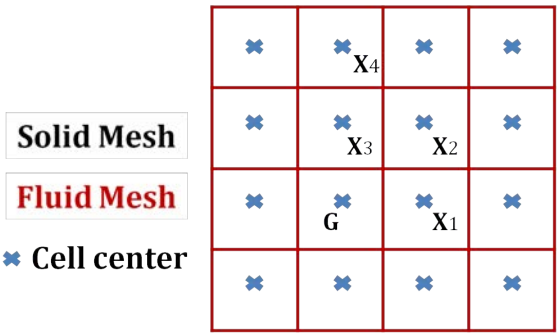

Figure 2.11: Ghost cell [Mittal and Iaccarino, 2005]

Tseng [Tseng and Ferziger, 2003] proposed a general procedure of the ghost-cell method:

- Identification of the interface and the ghost-cell. A level set method can be used.
- Extrapolation to find the correct values of the ghost cells.
- Solving the Navier-Stockes equation.

Once all the ghost-cells are depicted, the challenge is to find the value which has to be enforced on the ghost-cell to get the desired value on the interface. In the most general case, i.e. non-conforming meshes, for each ghost-cell an extrapolation is used to find the value which is prescribed. A number of options are available for constructing the extrapolation. For a general variable ϕ, the extrapolation can be:

- bilinear as reported by [Durbin et al., 2001].

$$\phi = C_1 x_1 x_2 + C_2 x_1 + C_3 x_2 + C_4 \tag{2.30}$$

- quadratic in the normal direction and linear in the tangential direction [Durbin et al., 2001]:

$$\phi = C_1 n^2 + C_2 nt + C_3 n + C_4 t + C_5 \tag{2.31}$$

- readily linear [Durbin et al., 2001] and [Tseng and Ferziger, 2003]:

$$\phi = C_1 x_1 + C_2 x_2 + C_3 \tag{2.32}$$

In order to identify the constant of the extrapolation a collection of point's grid belonging to fluid media where the value is known can be taken.
The method is globaly conservative, but the conservation laws are not satisfied on the ghost-cells because of the interpolations. The Cut-cell method purposes to satisfy the conservation in both global and local.

Cut-Cell method The Cut-cell finite volume approach is based on a finite volume discretization to satisfy both, local and global conservation laws. It can be applied to inviscid and viscous flows [Seo and Mittal, 2011] [Udaykumar et al., 2001] or [Ye et al., 1999].
In order to treat the Cut-Cell method, co-localized grid, where all the variables are defined on the cell's center, definition is employed [Udaykumar et al., 2001] [**?**].
Firstly, according to [Mittal and Iaccarino, 2005], the cells are cut by the Immersed boundaries' structure are identified. Then, the cells whose the centres are in the fluid domain are reshaped by discarding the portion of these cells which are linked in the solid. Pieces of cut cells which lie in the solid are absorbed by the neighbouring cells. The common control shapes which are used such as squares or rectangles are turned into trapezes. The issue of the method is to asses the value of the flux (diffusion, convection, pressure gradient,...)on the cell-faces using the cell-centre values. As noticed, the boundary layer is a crucial part of the flow especially when the fluid is viscous, the approximations from the trapezoidal cells has to be of a sufficient order. The basic idea is to evaluate the flux through the trapeze's face using polynomial interpolation function. The unknowns of the interpolation function are expressed in terms of the values at the stencil points as shown in figure 2.12.

2.6 Time coupling

The previous section tackled the spatial discretization of both domains, fluid and solid. In order to complete the modelling of the fluid-structure interaction problems, the coupling conditions 2.13 and 2.12 have to be coupled in time.
According to the physical phenomenon the fluid-structure interactions could be classified from

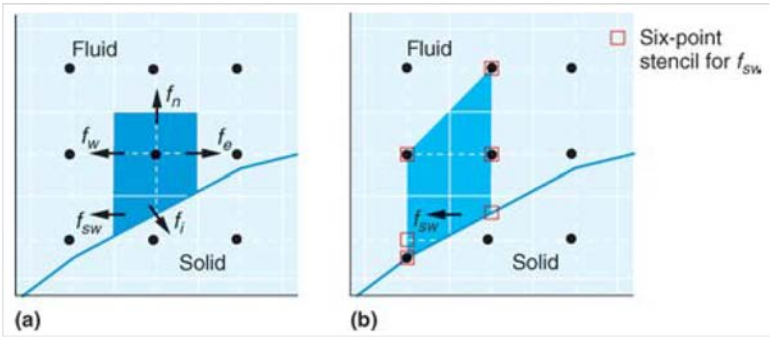

Figure 2.12: Stencil point for Cut-Cell method [Mittal and Iaccarino, 2005]

weak to strong regarding the degree of interaction. The partitioned strategies range therefore from weak to strong coupling. For a weak coupling, also known as explicit or staggered algorithms the coupling conditions are not necessarily fully satisfied, whereas the strong coupling aims to faithfully satisfy them. In order to converge to an accurate solution the strong couplings have to be iterative and are often called implicit.

2.6.1 The time coupling strategies

Among all the possibilities to treated the FSI problematics, the staggered is probably the most natural and appealing. It try to give accurate results by solving the coupling problem using only one iteration per coupling step. However several staggered algorithms can be found in the literature, some of them are presented in the next paragraphs.

Conventional Serial Staggered algorithm The Conventional Serial Staggered (CSS) algorithm [Farhat and Lesoinne, 2000] is the most simple algorithm and seems to be yet one of the most popular. The CSS algorithm solve simultaneously the fluid, the solid and the dynamic mesh following the next procedure:

- Transfer the solid wet boundary motion to the fluid mesh
- Update the fluid with regard to the solid motion
- Compute the fluid flow and read the pressures on the wet interface
- Turn the pressures to solid load cases, compute the solid and read the solid's motion

The previous procedure is sum-up in the figure 2.13.

Although the classical CSS algorithm is very appealing by is simplicity, some authors [Matthies et al., 2006] or situations show some disadvantages. In many situations the fluid

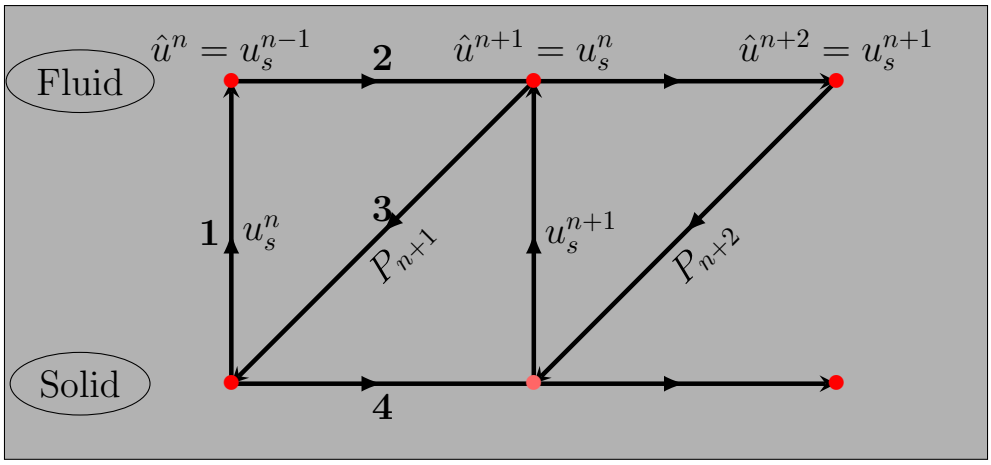

Figure 2.13: CSS algorithm

time step must be indeed smaller than the structural time step. But using the CSS algorithm, the two time steps have to be equal. This leads to an useless increasing of the computation time. Firstly because the structural simulation does not need so many computational steps, secondly a communication between the sub-domains is required and thirdly a mesh update is performed . In order to avoid this wasting time, the fluid modelling can be sub-cycling during one structural time step. This minor modification is depicted on the figure 2.14.

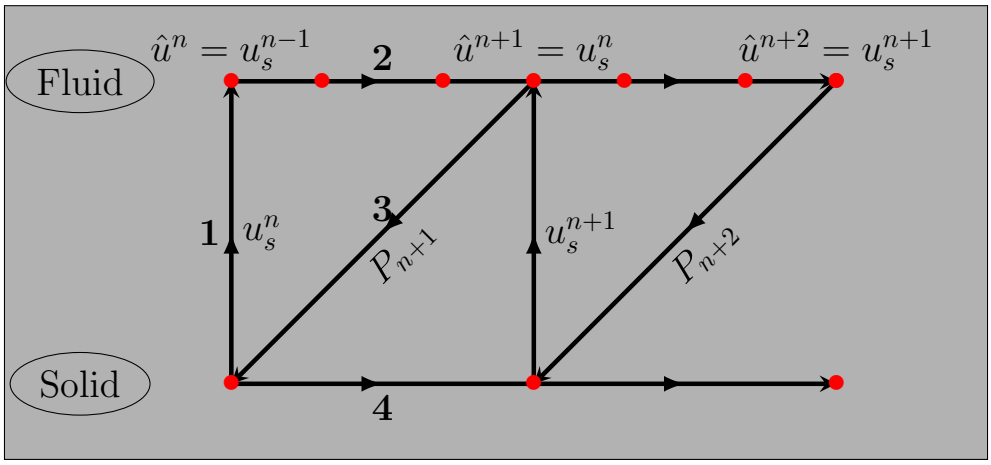

Figure 2.14: CSS with fluid sub-cycling algorithm

Geometric Conservative Law Before to proposed an improved coupling scheme it is important to point-out some difficulties which arise when an unsteady flow deals with a moving boundary and does not respecte the *Geometrical Conservative Law* (GCL). This observation is firstly done by [Thomas and Lombard, 1979] then a couple of papers have covered this question [Lesoinne and Farhat, 1996], [Farhat et al., 2001] [Farhat and Lesoinne, 2000] or [Donea et al., 2004].

The GCL imposed that the motion of the moving boundary has no effect on the flow computation. A simple test is to move the boundary during the computation of a constant flow, the results has to remain unchanged. The GCL can be elaborated from the mass conservation equation wrote in ALE configuration 2.19 which is integrated over a moving volume occupied by fluid and bounded by the surface S through a time step from t^n to t^n to obtaine the discrete GCL as it is explained in [Donea et al., 2004].

$$\Omega_e^{n+1} - \Omega_e^{n+1} = \int_{t^n}^{t^{n+1}} \left(\int_S V_m \cdot n dS \right) dt \tag{2.33}$$

Where Ω_e is the volume of the element e. The discrete GCL impose that the change in volume of the moving grid must be equal to the volume swept by the element boundary during the time step. Accordingly to [Koobus and Farhat, 1999] and [Lesoinne and Farhat, 1996], in boundary fitting method the flow solver and the mesh update procedure respect the GCL if the mesh velocity is computed by 2.34

$$V_m = \frac{U_m^{n+1} - U_m^n}{\Delta t} \tag{2.34}$$

Where V_m is the mesh velocity and U_m^n is the mesh displacement at time n.
It was shown that the FSI modelling which do not respect the GCL condition are inaccurate [Ma et al., 2015], [Lesoinne and Farhat, 1996]. The question is why error arise when the GCL is not respected? The reason is well explain in [Farhat and Lesoinne, 2000], indeed the structural prediction broadly used a second order accurate prediction as mid point or trapezoidal rules, the mesh velocity is therefore not an average of the nodes displacement, in other word $V_s \neq \frac{U_s^{n+1} - U_s^x}{\Delta t}$.
In boundary-fitting method, the interface position is used to being enforced on the same position than the structure $U_m = U_s$ in addition if the GCL 2.34 is respected, the problem is highlighted by the the equations 2.35.

$$V_m = \frac{U_m^{n+1} - U_m^n}{\Delta t} = \frac{U_s^{n+1} - U_s^x}{\Delta t} \neq V_s \tag{2.35}$$

Under such a condition, the exchange of kinematic energy is not equilibrated between the subdomains and instabilities could appear. Despite it is not a method adopted by all the authors, a part of the instabilities could be counterbalance by using a small time step.

Improved Serial Staggered The Improved Serial Staggered algorithm is developed by [Farhat and Lesoinne, 2000] to respect accurately the energy exchange on the interface and allowing an efficient staggered coupling on the same time. The ISS algorithm has to respect the GCL previously presented as well as the continuity equations. An illustration of this algorithms is shown on figure 2.15.

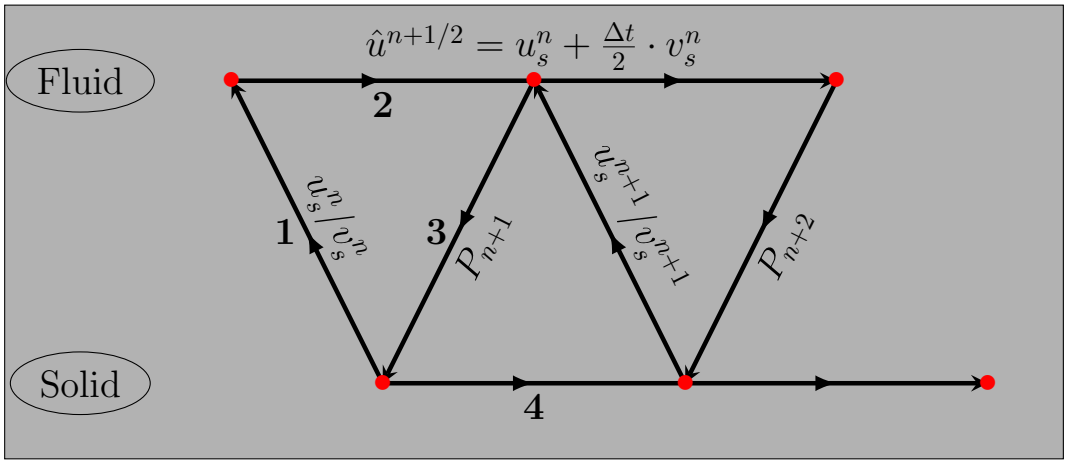

Figure 2.15: Improved Serial Staggered algorithm

The ISS algorithm depict higher perfomance than the CSS [Farhat and Lesoinne, 2000]. But if the solved problem require more accuracy or faster computation the ISS can be sub-cycling as well.

2.6.2 Added Mass effect

In the previous paragraph some staggered schemes were presented. Although the staggered algorithms are quit relevant, they are often subjected to instabilities mainly when an incompressible flow involving light structure is under consideration. It is demonstrated that the instabilities could come from the added mass effect. Before to tackle the numerical instability it is important to understand what is the added mass. This current section is then split in two parts, the first deals with the physical descrisption of the added mass while the second investigate the numerical instabilities roots.

Physical point of view When a fluid and a structure are in contact and one of them moves at velocity U some forces appear and a kinetic energy T is related (see Eq 2.36.

$$T = \frac{\rho}{2} \int_V u_i u_i dV \tag{2.36}$$

where $i = 1, 2, 3$ and u_i are the fluid velocity components.

The nature of forces could be classified according to the situations as described in [Fackrell, 2011].

First, if the body and the fluid have no motion then the only applying force is the static pressure.

Second, if the body depicts a rectilinear translation motion at velocity U and the fluid remains stable or conversely if the fluid depicts a steady state flow with at velocity U while the body remains immobile, a constant kinetic energy T is implied and no forces act on the body (see eq. 2.37). It is the d'Alembert's paradox.

$$T = \frac{\rho}{2} U^2 \int_V \frac{u_i}{U} \frac{u_i}{U} dV \tag{2.37}$$

where $\int_V \frac{u_i}{U} \frac{u_i}{U} dV$ is the fluid inertia denoted I. Such a case could be observed for potential flows.

Finally, if the flow or the body motion is unsteady, the kinetic energy evolves following its velocity U. As explain in [Brennen, 1982] if the body velocity increases, the fluid kinetic increase. An additional work must then be done by the solid on the fluid to increase this energy. Inertia forces F are therefore introduced.

DuBuat in 1786 [Du Buat, 1786] carried out experiences which illustrates the physical phenomenon. He shows that if a sphere is accelerated in water or air the original second law of Newton 2.38 could not predict the results, something else happen.

$$F = M.a \tag{2.38}$$

Thus he found that the inertial forces are not proportional to the acceleration and that a mass M_{add} has to be added to the structure mass M to account for the force.

$$F = (M + M_{add}) .a \tag{2.39}$$

It is relevant to quantify this inertia force. In [Brennen, 1982], it is shows that the inertia force is proportional to the rate of change of the kinetic energy.

$$-FU = \frac{\partial T}{\partial t} \tag{2.40}$$

if the fluid inertia I remains constant, the added force is

$$F = \rho I \frac{dU}{dt} \tag{2.41}$$

A short discussion can be done on the added mass effect as it is well carried out in [La Mantia, 2012]. The force expressed by equation 2.41 follow the same direction that the body acceleration. The term ρI could therefore be see as a mass of fluid which is accelerated by the body and is commonly named "added mass". The added mass is proportion to the fluid density as well as to the body shape. The added mass effect is therefore not a mass but a force which is proportional to the body acceleration and which is required to accelerate the fluid around the structure. Lot of application like aeroelastic could solve the problem without taking into account for the added mass. On the contrary, the added mass effect become important when the fluid density is close or higher that the solid one. This kind of situation is for instance a light solid moving in a water flow. The previous method could be extend to a more general case involving an arbitrary body motion and geometry. The force is then not confined in one direction but rather in all the six degrees of freedom. The general expression of the forces due to the inertial forces is [Brennen, 1982]

$$F_i = M_{ij} A_j \tag{2.42}$$

The added mass matrix M_{ij} has in the most general situation thirty-six parameters. Of course depicted some special situation like one dimensional flow velocity or body geometry symmetries, a couple of matrix terms could be fixed to zero. Nevertheless, the computation of added mass matrix could need special method as presented in [Fackrell, 2011] or in [La Mantia, 2012].
At this point the physical observations and understanding of the added mass effect is completed. The numerical treatment of such additional forces is presented in the next paragraph.

Numerical point of view It is observed that instabilities of staggered schemes occurred in the following situation [Förster et al., 2006]

- Instabilities occurs earlier when the coupling time step decrease.
- The bigger the ratio between the fluid and the structure densities is, the most unstable the coupling is.

- High fluid viscosity increases instability. Contrary to the viscosity, the structure stiffness intends the scheme to be more stable.
- The combination of the fluid and structure time discretization could lead to instabilities.

This paragraph claims therefore to explain the numerical instabilities induced by the added mass effect.

The source of instability is the addition of a mass term in the characteristic equation. To complete this objective it is convenient to take a mono-dimensional case as in [Söding, 2001] and following [Yvin, 2014]. The present case is characterized by the equation

$$m\ddot{y}^{i+1} = f^i = \bar{f}^i - m_a\ddot{y}^i \tag{2.43}$$

where i are the iteration of the implicit resolution, y is the position, f the total efforts, m_a is the coefficient of added mass to retrieve the forces coming from the added mass from the others and finally $\bar{f}^i$ is the other forces apart from the added mass forces. Following the resolution of the Ordinary Differential Equation (ODE in short), this equation is stable if the equation 2.44 is respected.

$$m_a < m \tag{2.44}$$

One of the most common stabilization method to solve the equation 2.43 is to add an artificial added mass on the both hand sides of the equation 2.43 [Song et al., 2013]. Commonly, the artificial added mass is firstly without dimension using the coefficient of added mass $\bar{C_a} = \frac{m_a}{m}$ and it is then used in a relaxation coefficient $\alpha = \frac{1}{1+\bar{C_a}}$. Finally following the development of [Yvin, 2014], the equation 2.43 is equivalent to solve the equation 2.45 using the fluid effort relaxation coefficient.

$$m\ddot{y}^{i+1} = \alpha f^i + (1-\alpha)\, f^{i-1} \tag{2.45}$$

As it was shown in [Söding, 2001] the relaxation coefficient has to be small when the added mass is high to counterbalanced their effects.

However, the instability does not occured immediatly, thus some authors worked on the developement of a limit's assesment to depict the instability onset. A depth study of the stability for staggered coupling scheme is proposed in [Förster et al., 2007] and [Förster et al., 2006]. It is

shown that an instability limit could be expressed function of the volumic mass ratio between fluid and structure. Following [Förster et al., 2007] if the equation 2.46 is respected then the scheme could be stable.

$$\frac{m^F}{m^S} max_i \mu_i < C \tag{2.46}$$

where μ is the eigenvalue of the added mass matrix, m^F and m^S are respectively the mass on fluid and solid and C is a coefficient which depend of the structural predictor and the fluid time discretization. [Song et al., 2013],[Mok and Wall, 2001] and [Wall et al., 1999] explain as well that the staggered coupling schemes are inherently unstable. The observations are enhanced by mathematical background proposed by [Causin et al., 2005].

[Förster et al., 2007] explains as well that the structure stiffness act on the coupling as a stabilising features whereas the fluid viscosity increased the instability. That explain why the stiffness and viscosity are an important parameter. In addition to that, the small time steps tend to reduce the stiffness influence regarding the fluid viscosity. The small time steps lead then to an instability. A lower time step is thus imposed moreover an upper bound is commonly imposed by the Courant–Friedrichs–Lewy (CFL) condition. In a fluid-structure interaction numerical problem the time step is thus bounded by an upper and a lower limit, the limit could be very tight or reduced to zero, the coupling scheme is in this case, unconditionally unstable.

Based on this considerations, several authors deal with the added mass effect to predict accurately the behaviour. In [Song et al., 2013] a simple piston case is developed to depict the instability onset and propose an iterative coupling scheme enhanced by a relaxation term to be able to solve the fluid-structure interaction problem for any density ratio. Furthermore, they give a method to asses added mass tensor by computed the modal participation factors of the pressure force vector.

[Jaiman et al., 2016] develops an iterative coupling scheme enable to deal with strong added mass effect. In order to be able to predict such coupling situation, the authors use a relaxation technique close to [Song et al., 2013], they show the superiority of this algorithm so-called NIFC scheme regarding to a classical fixed point method when high density ratio is studied. The iterative couping seems to be enable to deliver accurate result but they pay a hight computational cost to conterbalance this problem. Some authors like [Liu et al., 2014] developes a second order explicit algorithm named CFEI. Its stability is proofed by an

mathematical background based on energy evaluation. Subsequently numerical applications confirm the accuracy and stability as well as for high density ratio. [Banks et al., 2014] and [Banks et al., 2014] propose an explicit method calls added mass partitioned (AMP) method. The interface conditions are not expressed by the Dirichlet-Neumann but rather by the Robin condition.

Although, various methods are developed to evaluate numericaly the added mass, experimental devices are set-up as well. In [De La Torre et al., 2013] investigations in a hydrodynamic channel lead to develop a method based on the measure of natural frequency of the fluid-structure system to calculate the added mass coefficient. In addition to that the authors depict a relation between the added mass and the cavitation phenomenon [Brennen, 2013].

The fact is that the stability is harder to satisfied when the accuracy of the fluid time discretization scheme is high, i.e. get accuracy as well as stability cannot be achieved. The combination of temporal discretization has to be carefully studied to avoid instabilities onset.

2.6.3 The Iterative coupling

It is shown that the main advantages of the staggered coupling is the implementation simplicity and its low computational cost. It is the raison why the major parts of aero-elastic problems treating compressible inviscid flow use this kind of algorithm. Unfortunately, non respect of the coupling conditions can leads to a misprediction.

In order to solve this problem a readily method consists in impose several iterations of the GSS explicit algorithm. The aim of this iterative algorithm, referred as the Block-Gauus-Siedel method, is to impose as much as possible the respect of the coupling condition at the interface. Thus the energy balance is more equilibrated and the added mass effect is avoided on the same time. At each iteration, a residual is computed to judge if the equilibrium is reached or not, the equation respect is validated under a tolerance chosen by the user. Various residuals can be used, but it is used to defined it as the difference of the fluid and solid interface velocity:

$$r_n = u_s^n - u_f^n \tag{2.47}$$

Although, the iterative algorithm is more stable than an explicit one, several authors have shown that it can still diverge unless the two sub-domain modelling are stable and can suffer

from added mass effect as well. In addition to that, the iterations can lead to a very expensive computational time. Indeed, the global computation is longer that the sum of each fluid and solid modelling because at each iteration the time of information exchange can not be neglected. A way to improve the stability and the convergence speed is to used relaxation method. The relaxation method consists in enhance the residual by a relaxation parameter between 0 and 1 so that the interface displacement is reduced. The numerical value of the relaxation parameter has to be calibrated because higher the parameter is, faster the algorithm converge is but higher the instability occurred. The simplest way to specified a parameter value is to imposed a constant value all over the simulation. However other method have been developed to optimized the balance between convergence rate and stability. As well known relaxation method in FSI problem is the Aitken method [Jaiman et al., 2016], this method offers a dynamical evaluation of the relaxation parameter without needed any modification of the solvers as the the parameter is expressed as a function of the previous and current residual. Other acceleration technique is developed like the Newton at the Steepest descent technique.

2.7 Applications of the fluid-structure interactions

2.7.1 History of the modelling of the fluid structure interactions

The modelling of the fluid-structure interactions seems to show a growing interest since the eighty's. In order to confirm this tendency, a simple experience can be well known. The evolution of the number of publications per year could be drawn on the now broadly used publisher "Elsevier". On the wedsite, the request which is done is the research of the word's group "Fluid structure interaction" in the titles or in the keywords. Figure 2.16 provides a sum-up of the results. The conclusion is clear: the interest of the fluid structure interactions on the scientific field is growing.

Nevertheless, an overall study of the papers shows that a large part of the studies deal with only numerical modelling. A review of the benchmarks is performed in the following section.

Until 1980, only few authors investigated on the fluid structure interactions however the developed computed codes treat the coupling as a single problem and implement dedicated codes. Professor Hughes in 1980 speaks about the fluid-structure modelling as a new field which can be enhanced by the ALE method [Hughes, 1980], [Hughes et al., 1981]. As Hughes, other well know authors see the fluid-structure modelling as a important field to be investigated

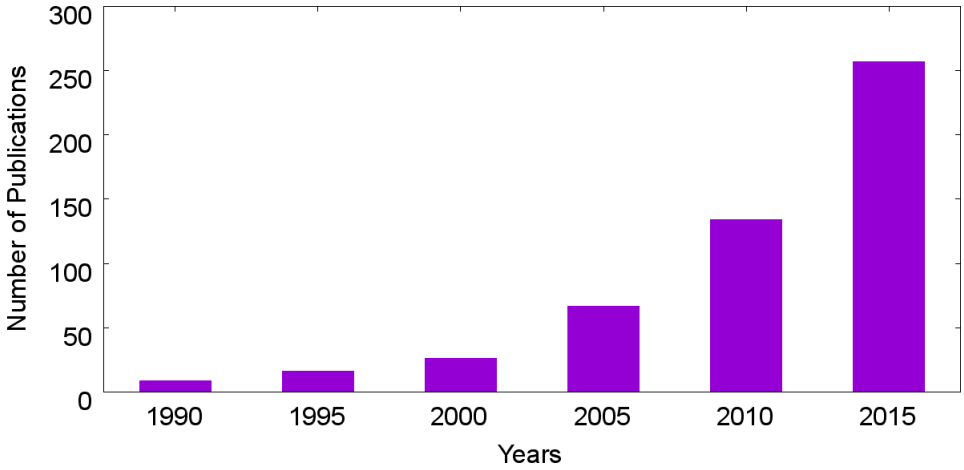

Figure 2.16: Hystory of the Publications dealing with FSI

as Professor Belytschko in 1980 [Belytschko, 1980], which purposes a survey of the modelling techniques and concludes that computations of the fluid and solid would be undertaken by different time integration and mesh descriptions, such conclusions will lead to the separation in a three fields problem coupling together: one is the solid resolution, the second the fluid computation and the third the mesh up-date. As it was already said Professor Peskin in 1972 developed the well known immersed boundary methods unfortunately this method had not met an great interest immediately. Regarding the application fields before 1980 the investigated applications are mainly the Nuclear problems [Belytschko and Schumann, 1980] [Babu and Reddy, 1980].

From 1980 to 1990, the dedicated monolithic solver represents always the major part of computational methods. Nevertheless, the partitioned methods arise with for instance the fluid structure code ADINA founded by M Bath [Zilliacus, 2014]. The first problem of the partitioned scheme are studied like the stability [Neishlos et al., 1981] as well as the problem of the balance between the time step limitations and the computational time. The partitioned methods need to treat the mesh as a dynamic mesh, various techniques are then proposed and the Arbitrary Lagrangienne Eulerienne configuration found more and more interest mainly after the paper of Professor Hudges published in 1981 [Hughes et al., 1981]. Although the nuclear applications has not disappeared, they are less often found and are replaced by hydrocode applied in marine' applications [Samuelides and Frieze, 1989], sloshing and tank begin to be investigated [Debongnie, 1986].

From 1990 to 2000, the increasing of computational capabilities in terms of CPU efficientcy and particularly in terms of modelling accuracy in both solid and fluid leads to a broadly implementation of the partitioned schemes [Farhat and Lesoinne, 2000] to joint the advantage of the already developed fluid and solid solvers. The new partitioned schemes are used mainly in aeroelastic application to depict the onset of flutter of wings or air-plane [Iii et al., 1999]. The study of the flutters leads the authors to depth studies of the code's stability based on the energy conservation. A major part of the aeroelastic problem treat air as the fluid, the euler equations are then used and the added mass effect are not the main problem[Piperno et al., 1995].

From 2000 until present days, the most used method is still the partitioned schemes as they are the less expensive coupling algorithm, and required the fewer implementation efforts [Li et al., 2016]. The main evolution of such methods are the good correlation of the couplings involving incompressible and viscous fluids and added mass effect. In addition, several authors work on the code's performances using the parallelism between several computers. Now a day, some middle ware are developed for industrial application, the fluid-structure interaction managed to turn and used this middle ware to pair-up a solid and a fluid solver. The middle-wares offer lot of possibilities to enhance the coupling by addition of electromagnetic or thermic solvers. In the C++ language, a library is devoted to the creation of middle-wares, the CLT library. Dspite the interest for partitioned schemes, one of the main investigated method for 5 years is the used of non-boundary fitting method based on the earlier proposed method of the Professor Peskin with Immersed Boundary Method [Pasquariello et al., 2016] [Schwarz et al., 2016]. The applications are more and more versatile, the behaviour of composite structures is studying, lot of biomechanicals subject are treated [Aletti et al., 2016] [Huihao et al., 2014] as well as optimisation [Aghajari and Schäfer, 2015].

2.7.2 The benchmarks

The previous fluid-structure time line history leads to conclude that several numerical developments were carried-out and the major part of the numerical developments are validated based on benchmarks. The next paragraph presents the most frequently adopted in the literature to validate the coupling algorithms.

Among all the fluid-structure applications which could be used for validation, four of them are broadly used.

The first one often called "lid-cavity" depicts a very simple geometry. It is commonly used for the validation of Computational fluid dynamic code [Ghia et al., 1982], [Bruneau and Saad, 2006] or [Marchi et al., 2009] but some authors have modified it to involved a fluid-structure interaction [Wall, 1999], [Küttler and Wall, 2008]. The lid-cavity without fluid-structure interaction is shown in figure figure 2.17a. The cavity is full of fluid and a horizontal velocity is imposed to the top of the fluid, a principal vortex is created and a couple of smaller vortexs appear near the bottom corners. A fluid-structure interaction test have been developed based on the lid-cavity. The configuration is nearly similar but the bottom surface is flexible as shown in the figure 2.17b. Thus, because of the created vortex, a depression is imposed on the flexible structure. The structure bending could be used as parameters for the validation according to the input velocity.

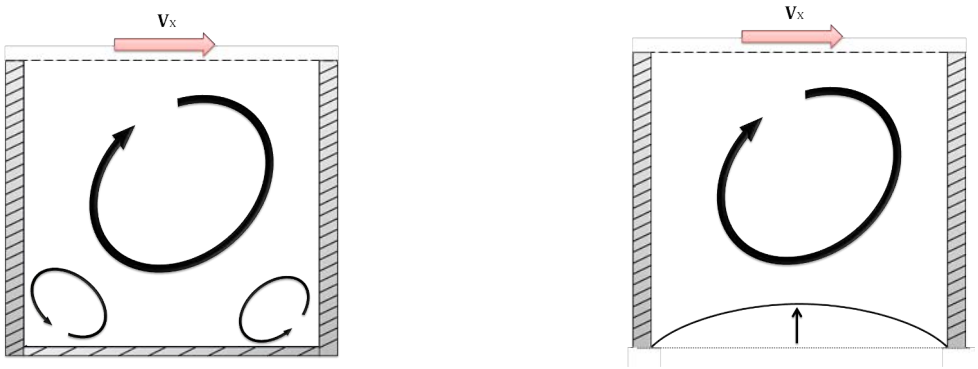

(a) Without fluid-structure interactions

(b) With fluid-structure interactions

Figure 2.17: Lid cavity test

The second test is very often used as it implies oscillation induced by vortex, thus complex fluid-structure interaction could be studied with large deformations. The test is presented in figure 2.18. The flow starts at the inlet of the obstacle and impacts it. According to the fluid velocity, vortexes could appear and trigged a asymmetric pressure repartition leading to the tail deformation. The most efficient situation to reach the flutter of the tail is the von Karman streets.

The study of the aeroelastic problem involving compressible inviscid fluid are often validated on wing profile. The aim is the detection of instabilities to avoid the onset on flutters. Several wing geometries could be used however only couple of them are involved in a number

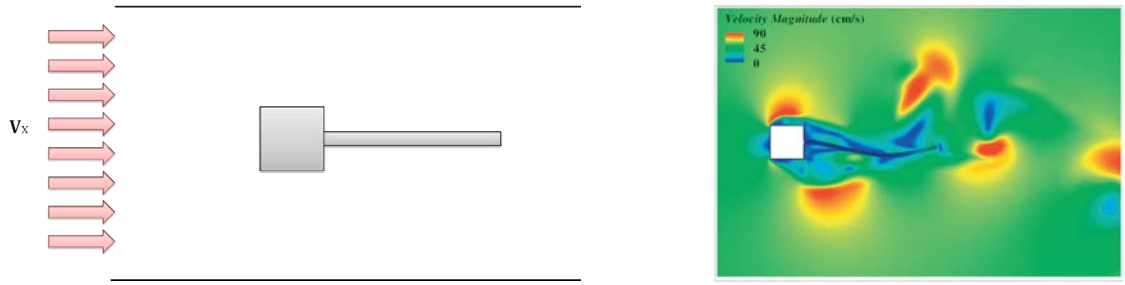

(a) Geometry (b) Typical results [Bazilevs et al., 2013]

Figure 2.18: Flexible structure behind rigid square

of published works.

The third largely used test deals with a very simple geometry as shown in figure 2.19 The flow impacts the plate which is clamped on basis. Under the pressure effects, the structure bends. According to the fluid velocity, the bending of the plate could be used as validation parameter. This test is very attractive because of, the easiness of the geometry, the straightforward structure measurements and the easy understandable fluid phenomenon involved.

It is observed that the fluid structure interactions are broadly investigated based on numer-

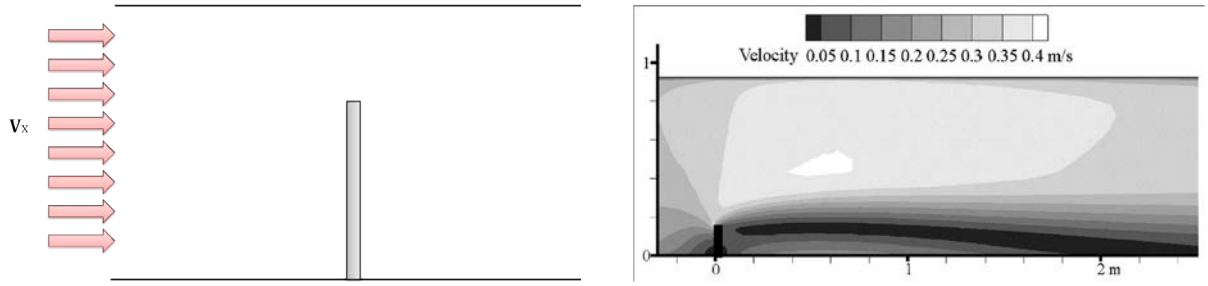

(a) Geometry (b) Typical results [Wu and Lin, 2015]

Figure 2.19: Flexible thin plate

ical study and the developed algorithms are often validated on typical benchmarks. But the question of the physical meaning of the results provided by the algorithms could be used when no experimental results are used for the validation.

The next paragraph will point-out the experiences found in the literature involving fluid structure interactions.

2.7.3 Experiences

It is important to mention that despite they may be classified in the fluid structure interactions all the applications such as blast and explosion are not take into account, because they are out

of the scope of the present thesis.

The hydroelastic and aeroelastic researches are still studying the experimental analysis. [Iafrati et al., 2015] investigated the aircraft ditching to understand the physical phenomenon and to support the validations of a developed code. This study is considered at a realistic high speed and used a real part of an aircraft, the SMAES-FP7. The pressure and the strain of the structure were measured and then interpreted. Nevertheless, authors [Sterenborg et al., 2014] reported the lack of experimental data. To overcome the problem, they propose to carried-out experiences to be compared to numerical results. Thus, [Gomes, 2011] proposed in his PhD thesis a great study. A flutter case as represented in figure 2.18a is placed in a wind tunnel full of water and able to provide a laminar as well a turbulent regime. They control and measure the flow velocity by means of a P.I.V. devise, and the position of the structure was tracked by an non-contacting magnetic angular position sensor. The structure was assumed to be rigid and is then subjected to only rigid body motions. Other aeroelastic experiences were presented, like the work of [Sterenborg et al., 2014], which set-up an experience composed of a wing subjected to an air flow, the wing was rigid and its motion was constrained to only vertical rigid body translation and rotation around the axis normal to the flow, a spring suspend the wing. The study computes the frequency of the structure and of the flow by means of a P.I.V.. They conclude that the accuracy of the measurements is not enough to be used for validation but the measures confirm the similarities of the aeroelastic problems with the viscous damped mass-damper-spring system. Despite the aeroelastic applications are still under interest, more and more industrial cases were investigated by experimental set-up. [Shangguan and Lu, 2004] investigated the behaviour of a hydrolic engine. The interaction are located between water and a soft rubber membrane used as spring. The fluid pressure and temperature are followed, subsequently a finite element model was developed to study the rubber behaviour. Other problems dealing with the behaviour of mechanical structure under water like [Huang et al., 2013] who investigates the behaviour of a trash-rack for an hydropower plants. Of course the trash-rack can collapse under an important impact, but the rupture often suffers from fatigue problems. The authors measured then the natural frequencies of the structure and compared it to the frequencies of the vortex shedding so as to avoid any coincidence between the frequencies. The frequency response of the tarsh-rack was measured under water using submergible accelerometers. The results were compared to numerical models and leading to the validation of the numerical model. The impact underwater was studied as well by [Huang et al., 2016] where an

aluminium alloy plate was subjected to an impulsive load. The plate behaviour was tracked by means of a digital camera and imagery correlation were subsequently used to discus on the occurring physical phenomenon. They affirmed to be able to asses the plate bending reduction at 53% regarding the same impact in air.

To conclude, the experiences conducted in the fluid-structure interactions filds are often applied to special issues and are therefore not relevant to be used as validation test. In order to validate the previously presented typical fluid structure benchmarks some experimental studies are completed however they dealled with only rigid and fixed structure. [Rajaratnam and Nwachukwu, 1983] proposed the experimental study a plate close to the figure 2.19a under turbulent flow or with two succesiv plates [Demartini et al., 2004]. [Ramm et al., 1998] provided a flutter benchmark with square obstacle 2.18a often taking as reference, although they did not come from experiences.

2.8 Conclusion

In order to improve the biofidelity of human body models the fluid-structure interactions have to be taken into account. This chapter aimed to have an accurate and deep overview of the fluid-structure interaction modelling methods.

The chapter have demonstrated that the partitioned method is the most attractive. The partitioned scheme carries-out the interactions by the data transfer between a fluid and a solid computational codes used as black-box. The fluid computations are often performed in an Eulerian or ALE framework and used a finite-volume discretization whereas the solid computational described the continuum in the Lagrangian framework and used a finite-elements discretization. The global fluid-structure system has to insure a constant energy. In order to have a constant energy, the data exchanges have to be equilibrated as well. Thus a set of coupling conditions insure the exchanges between the fluid and the structure. The information transfer is carried-out by the spatial coupling. Regarding the fluid and solid meshes, the spatial couplings could deal with boundary fitting method or non-boundary fitting method. The boundary fitting method is often referred as a three fields method as it involves a fluid and a solid computations as well as a mesh updating procedure.

Once the data are well transferred the frequency and sequence of exchange are managed by the temporal coupling scheme which could be explicit or implicit according the level of accuracy

wished.

A growing interest about the fluid-structure interaction modellings have been pointed-out. Nonetheless, many developed computation codes have been validated against only numerical benchmarks. Add to this, a lack of experimental tests especially made towards the computational codes validation have be highlighted in this work.

The next chapter investigates the fluid-structure interactions modelling in a bio-mechanical situation of the brain injury assessment.

3 A fluid-structure benchmark in dynamics: Experimental and numerical investigations

Contents

3.1 Introduction

As pointed-out in the previous chapter, the laboratory aims to contribute to the development of a biofidel human body model. In order to complete such an ambitious project, numerical models have to take into account influences of the fluid on the living parts behaviours. Unfortunately, two major issues arise, the living tissues and the fluid-structure interactions modelling. The living tissues or organs are very soft material which depict often high nonlinearities and viscosity. They are often non-homogeneous and non-isotropic as well. The characterization of such materials becomes therefore not trivial. In addition important variations of behaviour are observed between the living and post-mortem materials. Accordingly, the characterization, modelling and use of living materials still remain of scientific challenge. The difficulties arising from the fluid-structure interactions modelling have been demonstrated in the previous chapter as a key challenge regarding the stability, accuracy and efficiency issues of the coupling of two distinct and widely different domains.

A particular interest of the human head modelling is undertaken in this work. In fact, nowadays, the traumatic brain injuries (TBI) is still being a major issue in our populations as for instance more than 50.000 people pass way each year in the United States [Thomas et al., 2015]. Owing to this reason, researchers from various fields prompt to enhance the TBI mechanisms understanding in an attempt to reduced this significant societal burden. The laboratory has a strong expertise on the human head modelling and has already completed a couple of PhD works on the subject [Delille, 2002], [Rungen, 2004], [Delille, 2007], [Hault-Dubrulle, 2007], [Auperrin, 2009]. In order to have a better understanding of the TBI, the human head modelling and the related issues, a brief description of the human head anatomy is undertaken hereafter.

Human head anatomy

The human head is a very complex structure involving several parts such as bones, skin, muscles, vessels, nerves, etc. Regarding the objective of this study only the skull, the meninges and the encephalon are investigated.

The Skull The skull is composed of the neurocranium and the viscerocranium. The viscerocranium are the bones of the face and are not investigated in our study. The neurocranium is a structure of eight bones (see Figure 3.1a)which protect the brain. The skull bones are flat

with a sandwich structure composed of a spongy bone enclosed between two trabeculaes layers (see Figure 3.1b). The outer part of the cranium is smooth whereas the inner one is rough because of the presence of the vessel, nerves. Bone marrow filling-up the spongy bone trabeculaes while blood flows inside the compact bone by means of the Haversian and Volkmann's canals (see Figure 3.1c).

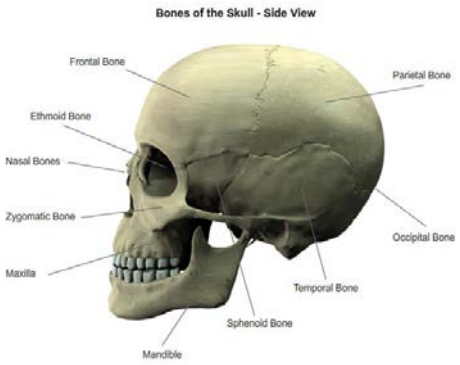

(a) Skull Neurocranium

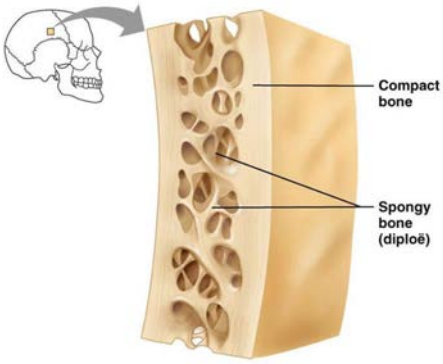

(b) Flat skull bone

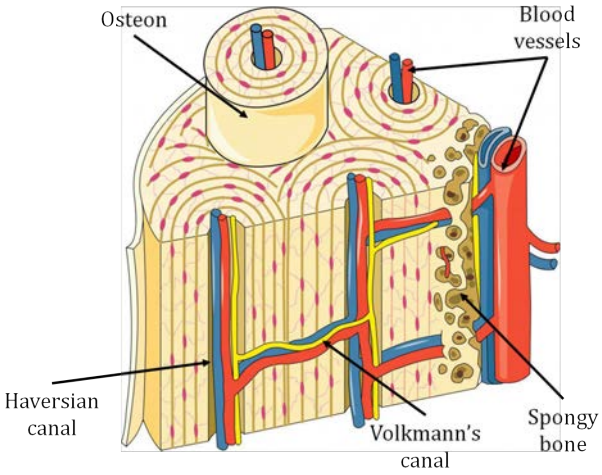

(c) Haversian system of compact bones

Figure 3.1: Human skull

The Encephalon The spinal cord and the encephalon are the central nervous system. The encephalon is composed of the brain, the cerebellum and the brain stem (see Figure 3.2a). The brain is the largest part of the encephalon and is split in two hemisphere the right and the left. In the cerebrum, the gray and white matters can be observed (see Figure 3.2b). The gray matter is mainly composed on nerve cells and the white matter releases the connection between the the periphery and the center of the brain by means of fibres called axons.

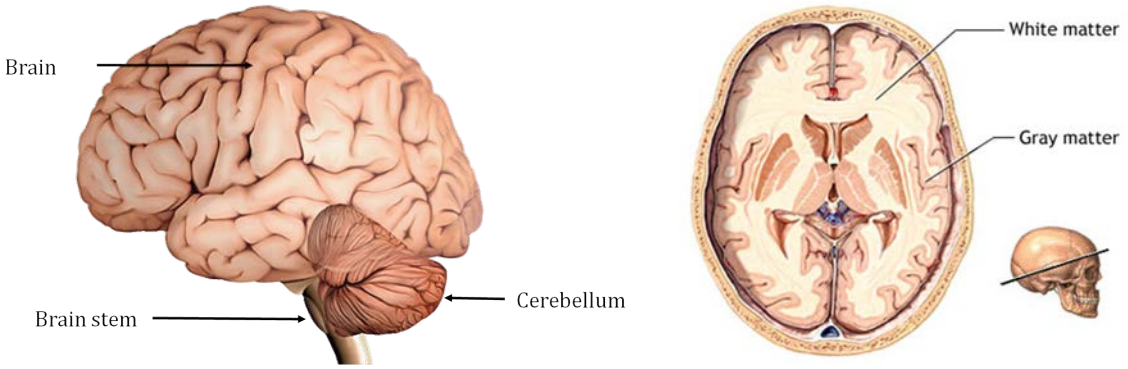

(a) Encephalon anatomy (b) Section cut of the brain

Figure 3.2: Human Encephalon

The Ventricular system The ventricular system is composed of four cavities full of cerebrospinal fluid (CSF) (see Figure 3.3). The four ventricles are composed of two lateral ventricles, the third and the fourth ventricles. All the ventricles are connected together to allow the CSF to flow. The CSF is produced by the Choroid plexus once the ventricles are full, it flows inside the subarachnoid space through the fourth ventricle. In the subarachoid space the CSF is reabsorbed by the arachnoid granulations.

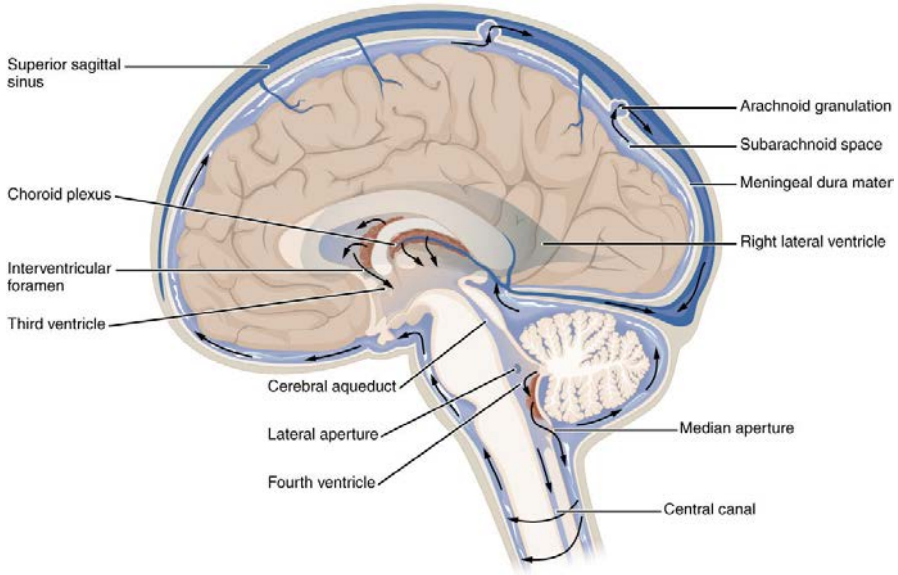

Figure 3.3: CSF circulation

The Meninges The meninges are a collection of three membranes located between the skull and the central nervous system and aim mainly to protect the encephalon against mechanical damage and contribute to its venous vasculature. From the outermost of the head to the innermost the three layers are the dura-matter, the arachnoid mater and the pia-mater (see

Figure 3.4a).

The *Dura-mater*, is a fibrous thick and through layer which is vascularized by the meningeal artery and has nerves. Actually, the dura-matter is split in two layers, the outer layer (Endosteal) stacks the skull and the inner layer (meningeal). Between the two dura-mater sheets there is the dural sinuses which collect the blood. The meningeal can be somewhere separated to carry-out the falx cerebri, and the tentorium cerebelli (see Figure 3.4b). The falx cerebri split the brain in the right and left part while the tentorium cerebelli separates the cerebellum and the brain.

The *Arachnoid mater*, is the middle element of the meninges. The upper face of the arachnoid is in contact with the dura-mater. Under the arachnoid there is a space of about 3mm, known as sub-arachnoid space it is full of cerebrospinal fluid from the arachnoid a large number of collagen trabeculaes rely the pia-mater. The arachnoid is therefore the barrier between the blood flow of the dura-mater and the cerebrospinal fluid of the sub-arachnoid space.

The *Pia-mater* is a very thin membrane which adheres perfectly to the encephalon following the gyri and sulci. Although, the pia-mater is vascularised and lets the vessels go to the brain, it is impermeable to the cerebrospinal fluid. Between the meningeal sheets some spaces are bounded: the epidural space between the skull and the dura-matter, the subdural space between the dura-mater and the arachnoid, subarachnoid space between the arachnoid and the pia-mater.

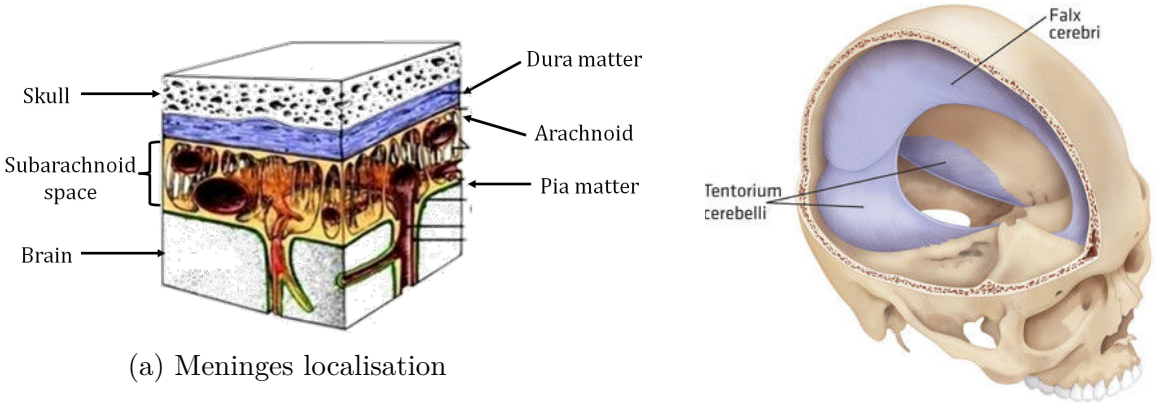

(a) Meninges localisation

(b) Falx and tentorium

Figure 3.4: Meninges

Brain injury Three different head injury types occur: the brain injury, the scalp wounds and the skull fracture. Only the brain injuries are ivestigated in this work. The brain injuries

can be sort in two familly, the focal and the diffuse injuries.
The focal injuries are commonly caused by a direct impact on the head, it follows a localized superficial injury which can be observed to the naked eyes. The focal injuries involved:

- The cerebral contusion and laceration resulting from the impact of the brain on the inner face of the skull, the coup-contercoup injury is a focal injury.
- All the hemorrhages which are a bleeding in the space of the meninges or in the cerebral matter lead to high pressure on thus matter damages.

Contrary to the focal injuries, the diffuse injuries are located on a widespread area and are thus called multifocal injuries. Such injuries arise from acceleration/deceleration and are microscopic and therefore not easy to be detected. It is observed that the rotational accelerations are very dangerous and lead often to diffuse injuries like concussion or diffuse axonal injury (DAI). The DAI is the most often observed diffuse injury. It is a collapse of the white matter due to high shear strain.

This previous anatomy study lead to several conclusions. The head is a very complex structure involving several interactions wherein the fluid plays a key role through various scales from the smaller, the havers canal in the skull bones to the larger, ventricles full of CSF. The brain is loosely coupled to the skull and can thus move inside the skull, this relative motion between the brain and the skull is a major cause of brain traumas. It has been shown that the CSF in the subarachnoid space covers and cushions the brain against the impacts resulting from this relative motion possibility.
In order to have a better understanding of the brain relative motion a common strategy is to build numerical models. The models aim to simplify the physics and to isolate the highlighting physical phenomenon. Three kinds of models could be actually used, the physical with real biologic matter or with biomaterial and the numerical models.
The *physical models with real biologic material* seems to be most efficient method because it involves real situations. Unfortunately, numerous complications arise as the ethical and hygiene issues as well as the great evolution between in-live and post-mortem tissue behaviours. One solution to overcome this problem is to perform measurements, like accelerations, on the head of living people and to compare them with the brain injury criteria. [Mihalik et al., 2012] and [Cobb et al., 2013] carried-out the instrumentation of helmets of football and Hockey players and compared the received impacts to the brian traumatic criteria. A other solution is

to perform the study of living anaesthetized animal often rats or mousse [Ucar et al., 2006], [Cernak, 2005].

The *physical models with biomaterial* use materials which have been engineered to mimic the physical behaviour. A major part of the real biologic materials problems can then overcame. Several physical models dealing with the brain injury using biomaterials can be found in the literature [Bradshaw et al., 2001], [Ivarsson et al., 2000]. Some other reproduce the head structure to asses the subarachnoid space effect [Klug et al., 2013].

Finally, the *numerical models* are more and more used because they do not require any physical material and allow to carried-out an important number of situations, load cases and materials. Nevertheless, deep studies are required so that the numerical prediction will become as fair as possible. Many authors investigated the biofidel representation of this relative motion and all conclude that the space between brain and skull has to be accurately modelled [El Baroudi et al., 2012] [Ji et al., 2014]. Actual finite-element (FE) representations of head do not represent the subarachnoid space [Asgharpour et al., 2014] or represent it using membranes modelling the meninges coupled with contact algorithms ranged from no-slip to slip conditions with variable friction coefficient [Roberts et al., 2012]. They introduced a layer of fluid usually represented with low shear solid elements between the brain and the skull to model the CSF [Yan and Pangestu, 2011] [Iwamoto et al., 2007].

All conclusions drawn from these works converge towards the need to account for a more realistic representation of the subarachnoid space. Thus several research investigation were devoted to the study of the subarachnoid space and the role of the cerabrospinal fluid. [Jin et al., 2011] used bovine subarachnoid to carried-out an experimental charaterization. Nevertheless, the major part of the studies treats the problem only with numerical models. [Saboori and Sadegh, 2011] discussed on the better subarachnoid space material modelling using either fluid or linear elastic or porous models. [Gu et al., 2012] studied the influence of each of the meninge part and [Zoghi-Moghadam and Sadegh, 2010] proposed an equivalent model to take into account the trabelulaes and the cerebrospinale fluid.

All proposed FE models have to be validated thoroughly against experimental data. Because of the major drawbacks of the physical models with real biologic material, a physical model with biomaterial is proposed in this work. The aim of the benchmark is to demonstrate that a water layer affects the displacement patterns of a biomaterial as the CSF strongly influences the brain motion. It should be noticed that this benchmark is developed for the head and

accidentology but can also be extended to other fields of application (pregnant woman, breast implant and all engineering applications that put forward soft materials surrounding by fluid). In our work the benchmark is used at two stages: firstly, without including fluid to validate the material model of the biomaterial. Secondly, with including fluid to test and improve the fluid-structure numerical methods. The experimental test is presented and the results are given. Subsequently the numerical modelling of the experiemental test are investigated on one hand without fluid and then with fluid.

3.2 Experimental dynamical fluid-structure benchmark

3.2.1 Experimental set-up

The experimental device was developed in the PhD [Hault-Dubrulle, 2007] to investigate the behaviour of a soft material in rotational transient loadings under high strain-rate of deformation in two configurations. One configuration did not involve any fluid, the second involved a water layer around the soft material. The version without water allowed to depict the only soft material behaviour whereas the version with water led to conclude on the fluid-structure interactions influence. The two experiments were subsequently used to validate and improve the numerical models.

Regarding the translation, the rotational accelerations impose the highest relative displacements between the brain and the skull and lead indeed to important injuries. Therefore a rotational acceleration was subscribed to the physical model.

The experimental set-up (see figure 3.5) was composed of a physical model held tight by an arm free of rotation and accelerated by means of a torsional spring device and followed by a highly accurate measurements apparatus.

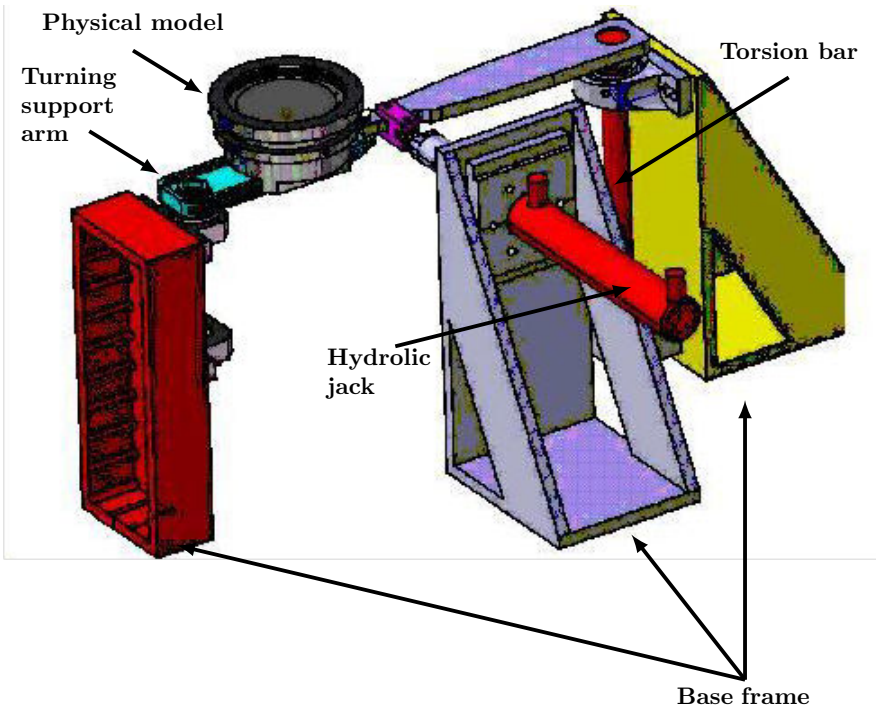

Figure 3.5: Dynamical test

The physical model

The physical model consisted of a rigid aluminium cylindrical vessel of 75 mm height and 180 mm inner diameter. On the vessel four markers called vessel markers were placed such as an orthogonal reference system could be draw (see Figure 3.6), they allowed to trigger the vessel kinematics.

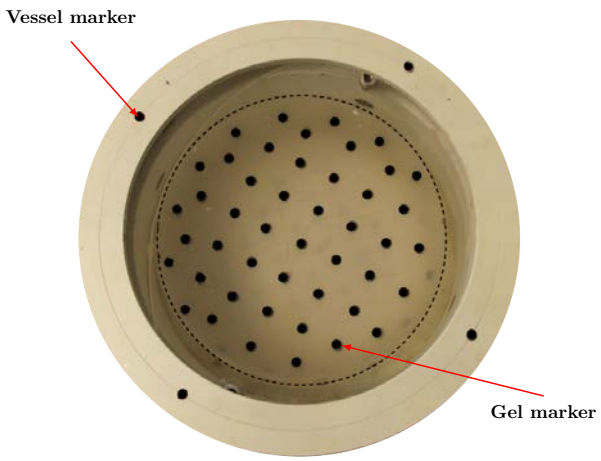

Figure 3.6: Physical model: Markers positions

A gel cylinder of 75mm height and 150mm of diameter was made of Sylgard 527 A&B

silicone gel. The two components were mixed in a one-to-one mass ratio then it was covered and left at the room temperature to complete the polymerization for 48 hours. Small paper markers (4-mm diameter) were placed in the middle horizontal plane of the gel (named gel markers) to capture the deformations (see figure 3.6). It could be assumed that the markers have no significant influence on the gel behaviour. The markers were placed on the gel following a grid pattern, which had to be fine enough to capture the deformations accurately; however a minimum gap had to be respected to enable the tracking motion device to distinguish two neighbors' markers. The spaces between the middles of the markers were approximately 10 mm. The gel casting was done in two steps: the first step was done until the middle of the cylinder, then the markers were placed and 48hours were left to ensure a full polymerization. In a second cast, the cylinder was filled. Regarding the gel texture, the gel behavior was not affected by the number of cast and behaved as one part. This conclusion was already drawn in [Ivarsson et al., 2000]. Thus the cylinder could be considered being a unique part and not two staggered components.

The gel cylinder was placed on the middle of the aluminium vessel which was closed by a transparent Plexiglas cover. The gel is gluey and then considered as stuck to the vessel bottom and the Plexiglas cover, hence no relative motion could occur between the gel and the rest of the apparatus.

Between the gel and the inner surface of the aluminium vessel, there was a gap of 15mm. Two configurations were then possible. The first possibility achieved the experimental set-up without water(see Figure 3.7a). In order to hold the gel cylinder, another aluminium cylinder was fixed into the biggest. The inner diameter as well as the height of the inner aluminium cylinder is exactly the same than the gel cylinder, i.e. 75mm and 150mm respectively for the height and the diameter. They second configuration achieved the experimental set-up with water(see Figure 3.7b). In this configuration the gap between the gel cylinder and the external aluminium cylinder was filled-up with water. A stopcock and a bleeding system wherein the gap was filled of water without any air bubble were added.

(a) Without water (b) With water

Figure 3.7: Cylindrical experiment

The loading device

An experimental device, able to generate high rotational acceleration magnitude in the experimental model was developed. The load was applied without impact to avoid to excite all the frequencies which may lead to add noise in the measurements. It was therefore based on energy exchange between potential energy stored in a torsion spring and kinematical energy transmitted to the model. The torsion spring was made of a steel bar (35NCD16) embedded at one end and tied to a rigid arm at the other end. This rigid arm was related to a hydraulic jack via a FGL250 cast iron specimen and was used to put in torsion the steel bar. The specimen was loaded in tension and was dimensioned to break down when sufficient potential energy was stored in the steel bar. When the tensile specimen broke, the torsion bar returned immediately to its equilibrium position and pushed promptly the model. A hinged link was made to ensured the free rotation of the model.

Experimental mesurements

The behaviour of the structure was tracked by a couple of measurements devices. Firstly, for the two configurations: without and with water, the gel displacements had been measured by means of a tracking of both, the gel markers and the vessel markers. Secondly, for the configuration with water the pressure had been tracked through the motion by sensors. Some of the characteristics of the motion tracking and pressure sensors are subsequently given.

Markers's tracking During the experiment, all markers positions were recorded at 1000 frames per second by a high-speed video camera (Kodak Ektrapro ES Motion Analyser) at a resolution of 512x384 pixels. The marker images thus obtained were post-processed with tracking software (Track Eye Motion Analysis).

Pressure sensors The history of the pressure inside the fluid layer had been obtained by means of four sensors screwed on the mid plane of the vessel and located at each pole: north, south, east and west. The piezoelectric sensors (type 403A5 from Kistler) were screwed until the inner face of the vessel to avoid all flow perturbations.

3.2.2 Experimental results

General results

The cup rotation was conducted in a horizontal plane in the counter clockwise (see figure 3.8). The distance between the center of rotation and the center of the vessel was arbitrary fixed to 165 mm. The experiences were repeated several time using the two configurations over different acceleration levels. The configuration without water was fulfilled five times while the second configuration with water was fulfilled eight times.

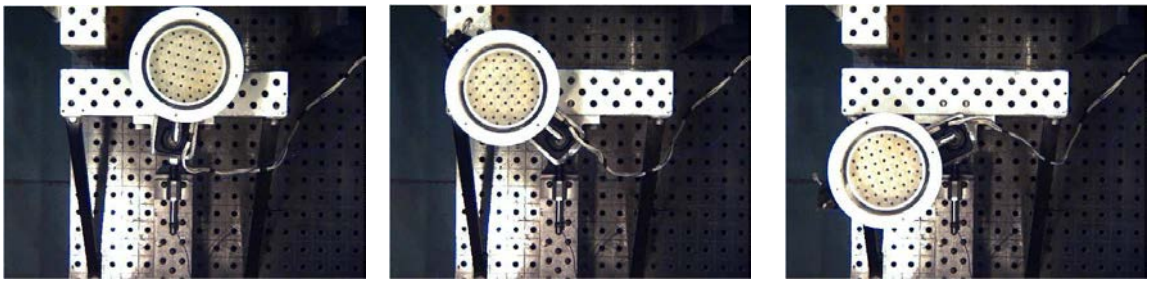

(a) t=0 ms (b) t=30 ms (c) t=130 ms

Figure 3.8: Dynamics rotational experience

A good repeatability was observed over the tests with and without fluid and over the different acceleration levels. Furthermore, fluid strongly influenced gel responses whereas the angular acceleration only induced a change in displacement and strain amplitude. With reference to these conclusions, a loading case was chosen for numerical investigations and is presented here. The motion of the vessel was presented on the set of curves 3.9. The angular velocity of the vessel increased during the first 132 ms until approximately 15.8 rad/s was reached. Afterwards, the vessel was slowed down and stopped at its end of motion range i.e. 350°. Associated peak angular accelerations were approximately 1600 rad/s^2. The displacement inside the gel was studied only for the acceleration.

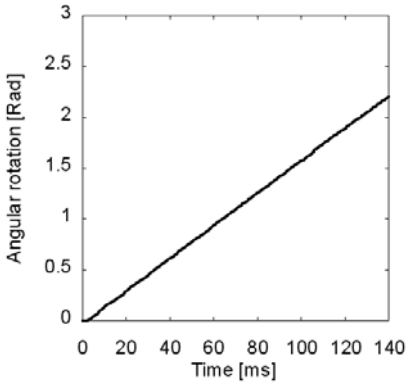

(a) Angular rotation

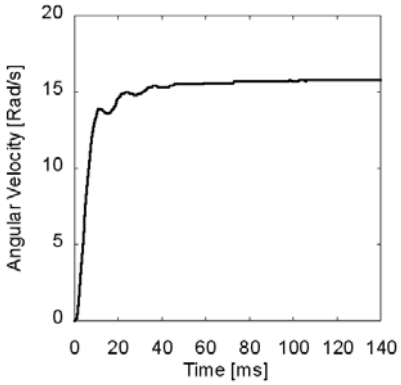

(b) Angular velocity

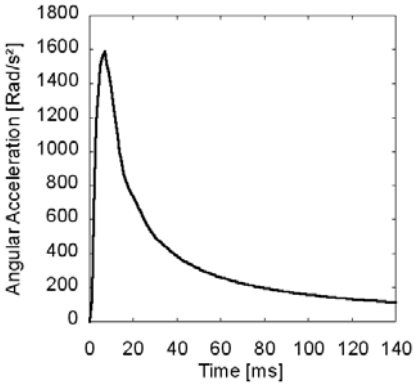

(c) Angular acceleration

Figure 3.9: Kinematics

Gel's kinematic

A total of 52 gel markers were tracked. In order to compare accurately the displacement inside the gel block, the gel marker displacements were not more observed by the fixed coordinate system relied to the camera but rather by a local coordinate system named vessel coordinate system (see figure 3.10). The new local vessel coordinate system was fixed to the vessel and was based on the vessel markers. The vessel was assumed to be perfectly rigid. Thus the coordinate of each gel markers as well as its displacements were expressed in the vessel coordinate system. Each gel markers had then one displacement component on the X_{vessel} axis and a second on the Y_{vessel} axis. It was more relevant to combine the two components by expressed the gel marker displacements by a single value: the norm of the displacement

$$Dispalcement = \sqrt{X_i^2 + Y_i^2} \tag{3.1}$$

Where X_i and Y_i were respectively the X and Y coordinates in the Vessel system for the i^{th} gel marker. The representation of the displacements was more convenient in the vessel system

as they correspond to the relative displacement regarding the vessel.

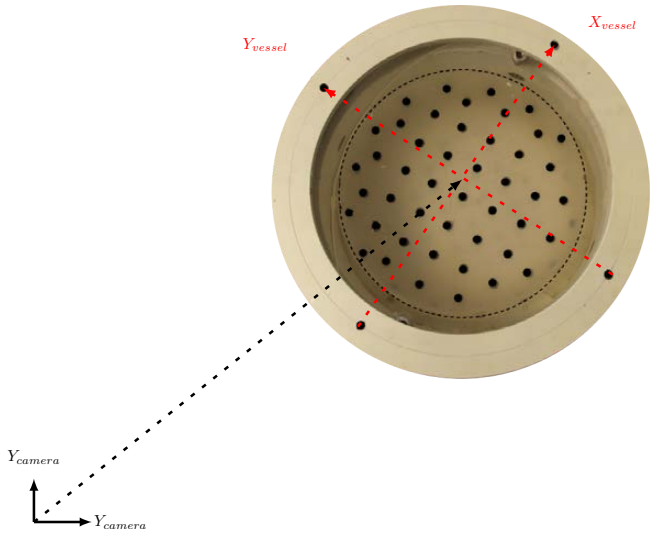

Figure 3.10: Vessel coordinates system

The presentation of all the 52 marker displacements for the two configurations, without and with water is useless and not suitable in this work. Accordingly, only the results for the gel markers located in the diameter, i.e. near a straight-line expressed in the vessel coordinate system by $Y_{vessel} = 0$, are given since they are representative of the whole behaviour of the gel. The numbers of the studying markers are given in the figure 3.11.

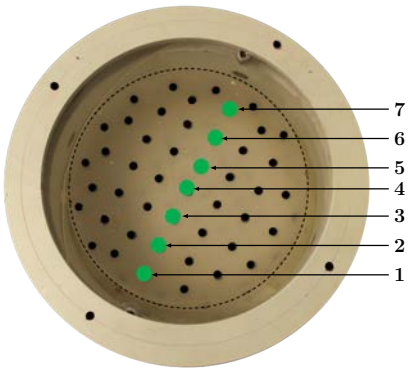

Figure 3.11: Localisation of specific markers of interest

The displacements of the gel markers are shown in figure 3.11 for the two configurations are shown in figure 3.12.

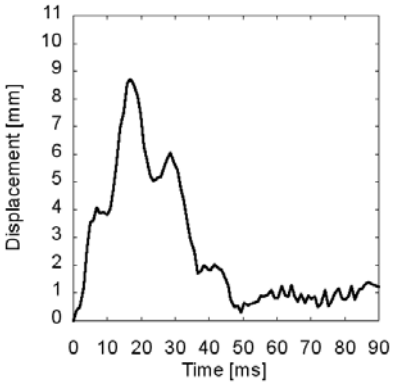

(a) Without water marker 1

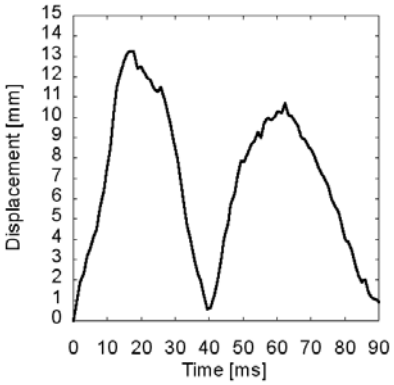

(b) With water marker 1

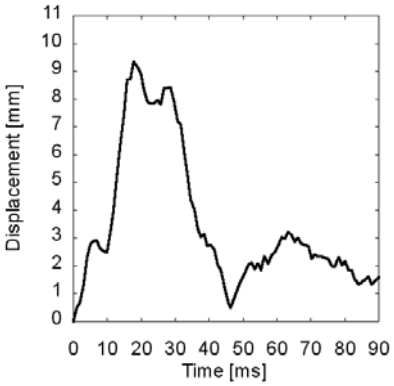

(c) Without water marker 2

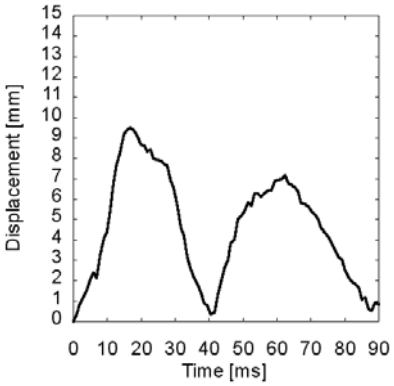

(d) With water marker 2

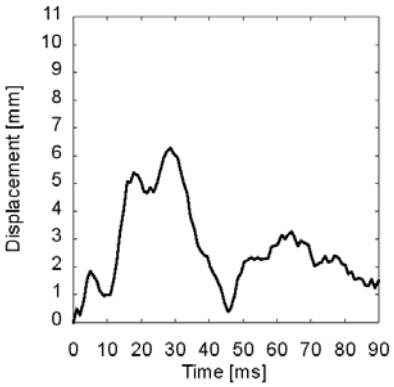

(e) Without water marker 3

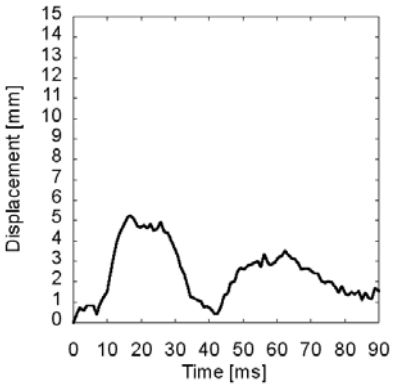

(f) With water marker 3

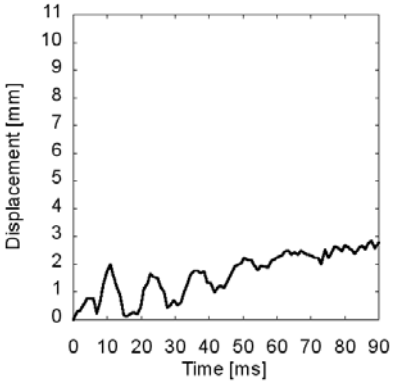

(g) Without water marker 4

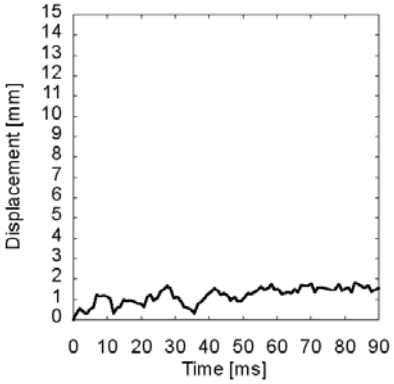

(h) With water marker 4

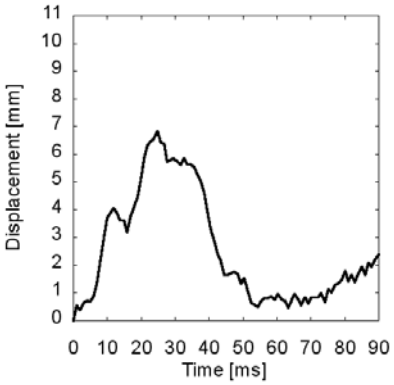

(i) Without water marker 5

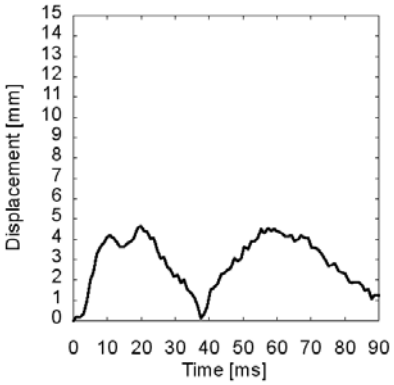

(j) With water marker 5

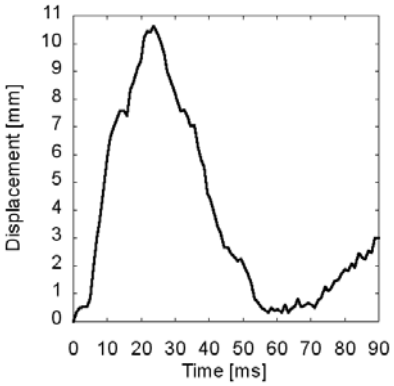

(k) Without water marker 6

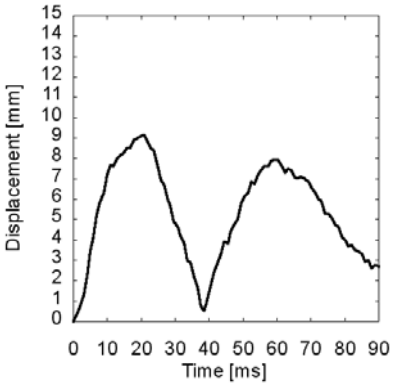

(l) With water marker 6

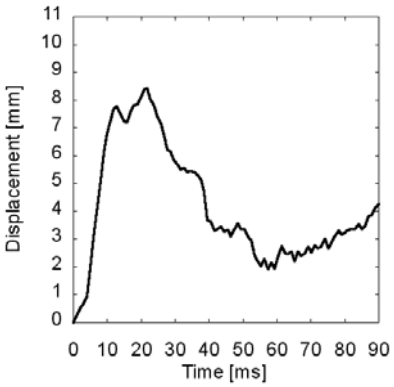

(m) Without water marker 7

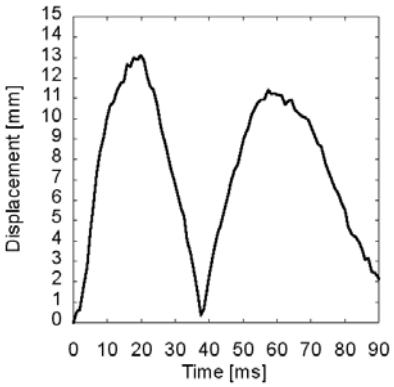

(n) With water marker 7

Figure 3.12: Dynamics rotational experience results

From a general point of view, two parts could be distinguished. A first peak was clearly observed, subsequently a second part which was either a smaller peak or a more constant phase. The first peak corresponds to the initial acceleration. When the model was rapidly accelerated forward, the gel lagged behind the vessel. The gel slided backward until it can go no further. This retarded behaviour explained the first peak displacement. After the first part the elastic come-back of the material enforced the gel to reverses its motion and travels forward. Despite the overall behaviour looked similarly a couple of differences could be

depicted.

The behaviours of the configuration without water are depicted on the left column of the figure 3.12. The first peak was clearly higher than the second part. After the first peak, it could be observed than the gel move backward immediately to its initial position either with a small rebound or without any rebound. No rebound were observed on the periphery (see figures 3.12a, 3.12i, 3.12k, 3.12m). This phenomenon was explained by the gluey characteristics of the gel which stacked on the vessel face. The periphery's displacements of the gel was therefore monitoring by the vessel kinematic. Contrary to the periphery, the inner displacements were not immediately related to the vessel kinematic, a rebound was then observed for the most inner markers corresponding to a forward motion of the gel because of the elastic come-back as well as the inertial forces (see figures 3.12e, 3.12c).

The behaviours of the configuration with water are depicted on the right column of the figure 3.12. Firstly, it could be observed than the first peak is always following by a second one corresponding to a rebound for the markers in periphery as well as in the center. Contrary to the first configuration, the rebound always occurred even for the periphery's markers because of the water layer which separate the gel from the vessel. In addition regarding the configuration without water, it could be observed than the first peak displacement is higher for the markers in periphery (see figures 3.12b, 3.12d, 3.12n) whereas it is lower for the inner markers (see figures 3.12f, 3.12j, 3.12l).

The previous observations allowed to conclude that the gel sustained more deformations when it was stuck to the vessel (configuration without fluid) whereas it depicted almost a rigid-body motion when a fluid layer dissociate the vessel and the gel (configuration with fluid). This final remark was explained by the fact that the rotational motion was not directly transmitted to the gel.

Due to the lack of time, the authors did not investigate deeply the modelling of the benchmark and failed to understand accurately why it wwas not able to model the interactions between gel and water. So in this PhD, I am interesting to the modelling of the fluid-structure interactions.

The dynamical benchmark will be used at two stages:

- The model without fluid to validate the material model and material parameters of the gel.

- The model with fluid to test and improve the fluid-structure interactions numerical methods.

3.3 Numerical modelling of the experiments

3.3.1 Model without water

The Sylgard 527 gel as well as other very soft materials depicts an elastic modulus in the range of some kPa. Its characterization is therefore still a challenge for conventional mechanical tests. In order to characterize this material, compression tests have been performed [Miller, 2005], [Morriss et al., 2008] but during the compression test barrel effect was inevitable. Several authors preferred to use indentation testing [Duan et al., 2012], [Liu et al., 2009], [Ma et al., 2010] which has proved to be an easy and powerful tool whereby numerical models could be calibrated. In order to characterize the mathematical models (hyperelastic, viscoelastic...), generally a force-displacement curve obtained experimentally is fit to find the best material parameters. Although such material models may be obtained readily and straightforward, they generally lack of robustness due to their sensitivity regarding the highly nonlinear behavior of the material and consequently the final mechanical response of a system which uses such gels still being limited [Ma et al., 2010] . Generally to overcome this problem, authors used calibration on the whole mechanical system and not for the sole material. Unfortunately in this case, any modification on the boundary conditions or the initial conditions of the mechanical device will lead to nonphysical results and requires a new material calibration.

This investigation aims to propose a specific methodology for the characterization and the modelling of Sylgard 527 gel under dynamic rotational loading. The proposed methodology is able to analyze accurately very soft materials in the case of transient analysis. In section 2, a detailed description of the Sylgard 527 gel material used in the present investigation and the adopted mixing procedure according to the Dow Corning recommendations. Section 3, is dedicated to the specific experimental setup used for the identification of material parameters in quasi-static under very large strains and a wide range of strain rates. In this section, several hyperelastic models have been identified efficiently based on a two-stage numerical procedure to reproduce the Sylgard 527 behaviour. At first, the material parameters were identified using a specific inverse method exploiting the indentation experiment. Secondly the validation of the obtained parameters was carried out using the dynamical experiment previously presented.

Following the quality of obtained results, it has been shown through the present investigation, that the proposed procedure presents good performances in terms of modelling and characterization of very soft materials.

A part of the results of this section have been published in [Fontenier et al., 2016].

Material

The brain matter was substituted by a bi-components Dow Corning Sylgard 527 A&B silicone gel. It is a two-component, room temperature and heat curing gel that is generally used for coating, encapsulating, potting, and sealing electronic devices. It provides flexibility, good flow, and low viscosity. Typical physical properties of Sylgard 527 gel are summarized in table 3.1. Depending on the ratio of mixture between the base and catalyst, the final Sylgard 527 gel can result in an extremely soft or firm part material, therefore it can be used for thermal/mechanical shock and vibration damping.

Properties	Values	Units
Viscosity (Part A or Base)	470	mPa.s
Viscosity (Part B or Catalyst)	454	mPa.s
Viscosity (Mixed)	465	mPa.s
Gel Time at $25°C$	7.8	mn
Working Time at $25°C$	120	mn
Head Cure Time at $100°C$	210	mn
Gel Hardness	113	grams
Penetration	45	1/10 mm
Volumic mass	970	Kg/m^3

Table 3.1: Sylgard 527 properties

The Sylgard 527 gel is based on polydimethylsiloxane (PDMS) formulations which are relevant to the study of cell behaviour to variable substrate mechanics and have the benefit of being easy to produce from commercially available PDMS while covering a wide range of appropriate physiologically elastic modulus.

[Azar et al., 2000] studied the Sylgard Dielectric Gel 527 and adopted the Mooney-Rivlin model which has been fit to the experimental data. The average parameter values reported were C_{10} = 3.74 kPa, C_{01} = 1.97 kPa for the silicone gel. [Brands et al., 2002] studied the non-linear behaviour of the Sylgard gel 527 A&B using a visco-hyperelastic model based on a 4^{th} order Mooney-Rivlin strain energy density for the detection of shock impact, up to 8 s-1 using a rotational apparatus. They obtained low values of Mooney-Rivlin parameters with maximal

range of the 4th order series as C_{10}=C_{01}=6.87 kPa. [Misra et al., 2007] used a hyperelastic material model identified using a sheer testing device, the Mooney-Rivlin obtained parameters correspond to C_1=-C_2=48.5 MPa, values which seem high compared to the literature. [Morriss et al., 2008] employed a Neo-Hookean material model identified using semi-confined compression experiments by means of fitting a solution of the finite element model of the experimental setup. They found a shear modulus of 1.5 kPa. [Ma et al., 2010] used the hyperelastic Ogden model and determined the couple of μ=2.44 Pa and α=4.46. [Palchesko et al., 2012] studied the polydimethylsiloxane formulation based on the blending of commercially available Sylgard 527; they showed its ability to create biomaterials with tunable elastic modulus over a wide range of magnitude. Under the assumption of linear elasticity, the authors found an elastic modulus of the Sylgard 527 gel of $5.05^{+}_{-}0.37$ kPa. [Appleby-Thomas et al., 2014] studied the high strain-rate response of Sylgard 527 gel using plate-impact experiments. Compared to other soft materials, the authors concluded about the necessity to use the Hugoniot equation-of-state model with a quadratic shock velocity to be valid for ballistic problems.

As it can be seen above, the mechanical characteristics of the Sylgard gel 527 are versatile and may vary enormously through the literature depending on the type of mathematical model and the linearized assumption made by authors for describing its behavior. In point of fact, the sensitivity of the Sylgard gel 527 material parameters is caused by the very low values of its mechanical properties which make them very difficult to be measured using classical devices and the second main reason is due to the nonlinear behavior of the silicone gel under very small loads.

According to the Dow Corning recommendations, the Sylgard 527 silicone gel has been obtained by mixing the base with the catalyst in a one-to-one mass ratio. Then it was poured in a cylindrical cup made of steel of 80 mm height and 150 mm of diameter. The large ratio between the indenter and the specimen ensured the semi-infinite assumption. Immediately after curing, the silicone gel was shaken to evacuate the air bubbles which may have been created during the mixing process. The cylindrical cup filled out with gel was then covered and rested at the room temperature to finalize the polymerization which requires 48 hours. Due to the gluey nature of the gel surface, it is assumed that the gel is glued to the lateral cylindrical walls and to the bottom basis of the cup.

Methods

Quasi-static indentation of the Sylgard 527 gel A quasi-static indentation apparatus for the identification of the local behavior of Dow Corning Sylgard 527 silicone gel was set-up using an Instron E3000 mechanical testing machine. The machine was equipped with a 1kN load cell and the stroke of the indenter was recorded following Instron recommendations. All the data were sampled at a rate of 10 samples per second. The indenter was a cylinder with a semi spherical head of 30mm diameter (see figure 3.13). The indented part gel was a steel cylinder of 80mm height and 150mm of diameter. A large ratio between the indenter and the specimen has been chosen on purpose in order to ensure the theoretical assumption of semi-infinite plan condition. Just few minutes after polymerization was complete, the cylindrical gel part was put centered right under the indenter. A linear stroke has been imposed to the indenter during the indentation experiment. The reaction force was recorder by the Instron E3000 mechanical testing machine. The indentation experiment has been conducted several times using different velocities in a range between 1 mm/min and 1000 mm/min, in order to represent the strain rate effects effect of the gel.

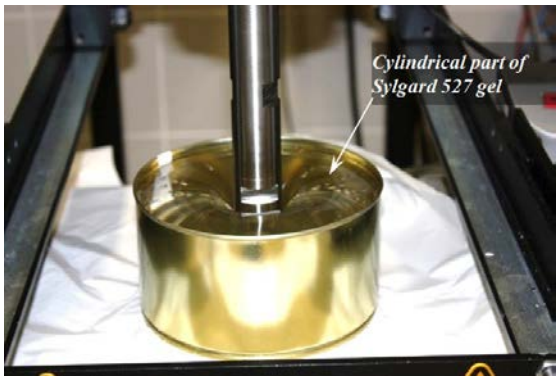

Figure 3.13: Quasi-static indentation of a Sylgard 527 bloc using hemispherical indenter

Figure 3.14 shows the evolution of the reaction force to the indenter vs. its stroke for three different loading velocities namely 1 mm/min, 100 mm/min and 1000 mm/min. First it has to be noticed that all three tests were carried out using the same specimen of gel. After each loading test, it has been observed that the final relaxed geometry of the gel part returned each time to its flat initial shape, therefore it allowed to conclude that no residual deformation or damage was introduced during loading experiment. Moreover, the deformed top surface of the gel cylindrical part (which receives the indenter) deformed only in the vicinity of the indenter and did not expend to reach the boundary walls of the cylinder (see figure 3.13). The assump-

tion of the semi-infinite media was then validated. Thus, the gel's characterization could be conducted accurately as no boundary effect could introduce undesirable structural effect.
During the indentation loading phase, it has been observed that large deformation of the gel occurs while a very small maximal reaction force can be triggered, around 6.5 N for a total indenter stroke of 30mm. It can be concluded at this stage of investigation that the indentation loading induced at least geometrical nonlinearities and most likely material nonlinearities. Therefore the classical linear elastic assumption sometimes encountered in the literature, cannot be taken to describe the physical behavior of gel since the loading path of Figure 2 shows clearly the nonlinear behavior of the Sylgard 527 gel. In the following, a first attempt will be the use of hyperelastic material models to describe the physical behavior of the Sylgard 527 gel.

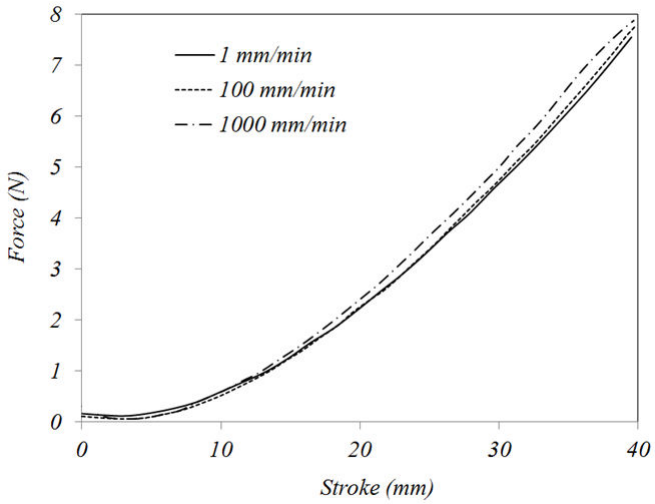

Figure 3.14: Indentation experimental results, indenter force vs. displacement

Relaxation test One can notice also from Figure 3.14 the fact that all three velocities did not lead to a significant change in the gel behavior. For the imposed kinematics of deformation, the Sylgard 527 gel seems not exhibiting any significant strain-rate dependency. Consequently it has been assumed that the viscosity could be negligible in the range of the used strain-rate. In order to confirm the assumption of the absence of viscosity effects and also pure elastic nonlinear behavior, a relaxation testing was performed. Creep and relaxation tests were two major experiences which led to study the evolution of creep and relaxation modulus respectively. For the creep experience a constant stress was imposed and the strain was triggered, whereas for the relaxation test, a constant strain was imposed and the stress was triggered.
In the present investigation, a relaxation experiment was performed by means of the same in-

dentation apparatus which has been shown above. The relaxation test was carried out instead of creep because the indenter stroke was readily controlled and it was easier to repeat the experiment for various loading velocities. During the indentation, a fixed stroke was imposed and the reaction force was monitored. Numerous authors showed that analytical treatments allowed to compute the elastic relaxation modulus based on the force-displacement, see for instance [Qiang et al., 2011] and [Toohey et al., 2016]. Moreover, for indentation test the relaxation of the forces due to the viscosity was qualitatively the same that the relaxation of the stress in the classical relaxation tests.

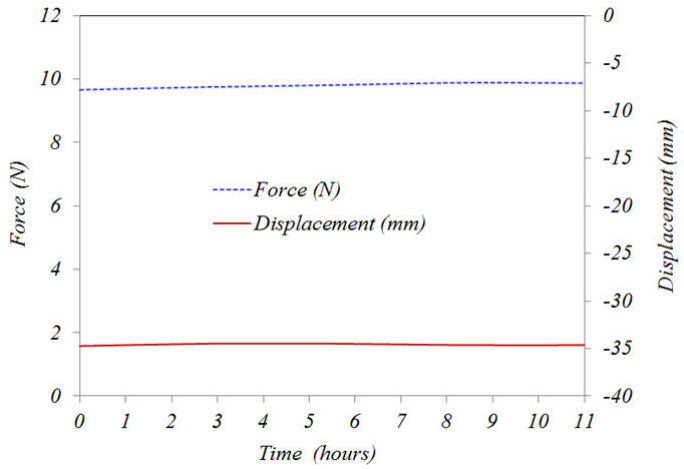

Figure 3.15: Relaxation Force/Displacement control

The relaxation test was performed on a gel Sylagrd 527 in a one-to-one mass ratio as well. The stroke of 35 mm was imposed at a constant speed of 100 mm/min. Subsequently the indenter was held in position and the reaction force was following at a sample rate of 1 sample per second. Imposed a constant stroke, the force was constant as well taking into account the measurement's approximation and the filter of the curves. The viscous effect could be neglected and the introduction of viscosity in the numerical model was therefore not useful in these ranges of strain and strain-rate (see Figure 3.15).

Non-linear constitutive relations Contrary to the elastic behavior, the hyperelastic laws arise from the Clausius-Duhen inequality [Charmetant, 2011] and are therefore based on thermodynamical formulations. The inequality of Clausius-Duhem drove the energy dissipation per unit of volume on the initial and final state of deformation. By definition, a hyperelastic material is then a material which does not dissipate energy. In addition, the strain energy (W) of the current state does depend on the history of the material. This leads to a major

property in the hyperelastic law: The energy cannot not be null if the material is not loaded or if it is subjected to a rigid body motion. In order to simplify the hyperelastic laws to only isotropic materials, the strain energy must be a function of the three invariants. It is common to use the invariants of the left or right Cauchy-Green tensor $W(I_1, I_2, I_3)$ or the principal stretches $W(\lambda_1, \lambda_2, \lambda_3)$. Which represent the coefficients of characteristic polynomial Cauchy-Green tensor or the eigenvalues of the deformation gradient tensor. The constitutive laws are subsequently derived from the strain energy density. Accordingly the Cauchy stress, σ as well as the second Piola-Kirchoff stress S, can be expressed as:

$$\sigma_i = \frac{\lambda_i}{J} \cdot \frac{\partial W}{\partial \lambda_i} \tag{3.2}$$

$$S_i = \frac{\partial W}{\partial \lambda_i} \tag{3.3}$$

where J is the determinant of the deformation gradient tensor, it is equal to 1 for the incompressible materials.

Several material models describing the strain energy density formulation have been proposed in the literature. The most popular are the Mooney Rivlin, the Ogden and the Neo-Hookean models. They are generally used to model rubber like materials or biomaterials submitted to very large strains.

Based on the literature, hyperelastic models are generally the most used mathematical models to mimic the physical response of Sylgard 527. Obviously, the simplest model is the Neo-Hookean [Moerman et al., 2009] [Morriss et al., 2008] as only one material parameter is required. The most used mathematical model is the Mooney-Rivlin [Azar et al., 2000] [Brands et al., 2002] [Misra et al., 2007], mainly because of its simplicity and relatively good accuracy for moderate strains (100%). Finally the Ogden model [Ma et al., 2010] which is a very efficient model because its versatility and accuracy, since it is able to handle very large strains (until 800%) was found in the literature as well.

As a first attempt in this investigation, the very simple and easy to use Neo-Hookean model [Ogden, 1972] was used. Indeed this basic material model which is available in LS-Dyna software, depends on only one material parameter, and the strain energy of a hyperelastic media

is expressed as,

$$W\left(\lambda_1, \lambda_2, \lambda_3\right) = \frac{\mu}{2}\left(\lambda_1^2 + \lambda_2^2 + \lambda_3^2\right) \tag{3.4}$$

with $C_1 = \frac{\mu}{2}$ is the unique material parameter to be determined.

The second hyperelastic model used in this investigation is the Mooney Rivlin model [Rivlin, 1948] which is also available in Ls-dyna commercial software. This model depends on two material parameters; it is widely used in several engineering fields as it constitutes a simple and a practical mathematical model. It is based on a linear combination of the two first invariants I_1 and I_2, and the strain energy can be expressed in this case as,

$$W\left(I_1, I_2\right) = C_{10}\left(I_1 - 3\right) + C_{01}\left(I_2 - 3\right) \tag{3.5}$$

The parameters C_{10} and C_{01} are the material parameters which have to be identified for each material in order to mimic the physical response.

Finally the general Ogden model [Ogden, 1972] which is more versatile and can handle very large strain has been used for the modeling of the Sylgard 527. This model is also available in Ls-dyna software. Contrary to the Mooney Rivlin model, it is based on the series summation of principal stretches.

$$W\left(\lambda_1, \lambda_2, \lambda_3\right) = \sum_{k=0}^{n} \frac{\mu_k}{\alpha_k}\left(\lambda_1^{\alpha_k} + \lambda_2^{\alpha_k} + \lambda_3^{\alpha_k}\right) \tag{3.6}$$

with N a parameter which represents the number of series chosen by the user. Naturally, the more N is high, better the quality of results is, but also difficult is the determination of material parameters μ_k and α_k are.

Numerical method for material identification The numerical model was performed using the commercial software LS-Dyna®. As shown in figure 3.16, the gel was modelled using 15975 constant stress hexahedral elements. A preliminary study of mesh convergence was carried out, and has shown that this discretization was fine enough to reproduce the solution with sufficiently accurate result in a reasonable CPU computing time. The indenter was modeled as rigid body and the contact between the indenter and the gel part was a penalty based formulation. It was assumed that once contact was established, the gel was stack to the indenter, and hence a big value of friction coefficient was employed. The Indenter was loaded using a ramp of stroke

in order to reproduce the same conditions to the experience, i.e. a velocity of 1 mm/min. A modified central difference scheme was used for time integration.

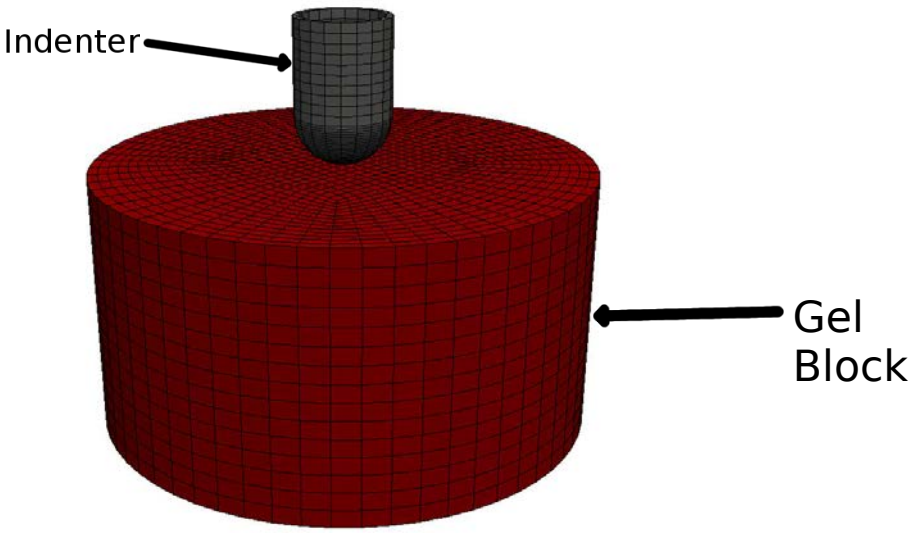

Figure 3.16: Finite elements model of the indentation test

An inverse iterative method was used to fit the hyperelastic mathematical model to the experimental curve. The optimization procedure performed by the LS-Opt® software, is based on the least square approximation method. The experimental and the numerical values of forces were evaluated at several sampling points. Then the errors were assessed and their squares were summed. Let's denote by X_{Exp} and X_{Num} the experimental and numerical force values respectively, the least square error was:

$$\epsilon = \sum_{k=1}^{N} \left(X_{Exp}^{k} - X_{Num}^{k} \right)^2 \tag{3.7}$$

The parameter X_{Num} was determined by minimizing ϵ.

Results and discussion

The determination of a material model which reproduces properly a polymer gel behaviour is crucial and depends mainly on the physical observation of the gel nature (linear elastic, non-linear hyperelastic, viscous, presenting some delayed permanent deformations ...). Once this crucial stage is done, the model parameters have to be determined as accurately as possible depending on the degree of softness of the polymer gel and on the stress precision needed. A current method widely used in the scientific community was to perform a Finite Element Model

(FEM) of an experience and by means of an inverse method, to calibrate the parameters from experimental responses.

This method was quit straightforward for conventional tests and material. But contrary to the conventional tests, the indentation of soft material led to non-uniform stress-strain field around the indenter. In addition to that, they often exhibited geometric and material non-linearities. Therefore, such materials were not driven only by a modulus but rather by a complex model involving a set of parameters.

In order to get accurate parameters, inverse method based upon experimental tests modelling by FEM seemed to be well adapted and frequently used over the last years [Czerner et al., 2015], [Liu et al., 2009] [Moerman et al., 2009]. Then a FEM of indentation test was carried out with a hyperelastic model for the gel and parameters were identified from experiences.

Several material models were used to simulate the gel behavior and for each model the best parameters were fitted. The Ogden model as well as the Monney-Rivlin models were already available in LS-Dyna whereas the Neo-Hookean model may derive from the Ogden reducing to only one couple of parameters and fixed $\alpha = 2$. Figure 6 shows the best results. The overall agreement was reasonable. The error was expressed as the ratio of difference between the areas of the experimental and the numerical curves regarding the area of the experimental curve. Thus the errors were around 1.5% for the three models. The models' parameters were summarized in the Table 3.2.

A comparison with the already proposed material parameters gave good insights. Only the Neo-Hookean could be compared. No available Mooney Rivlin model and no Ogden with six parameters were found by the authors. Nevertheless, the Neo Hookean parameters found in this study was agree with the works from [Moerman et al., 2009] [Morriss et al., 2008].

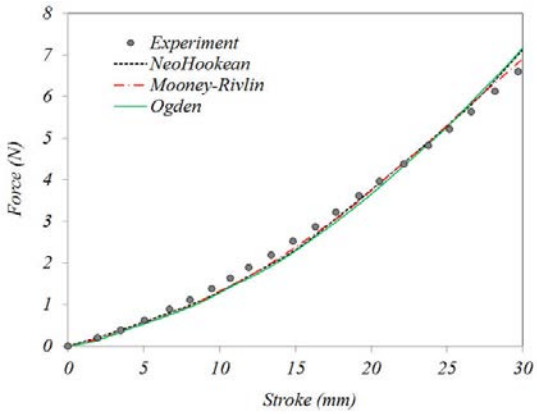

(a) Quantitative results

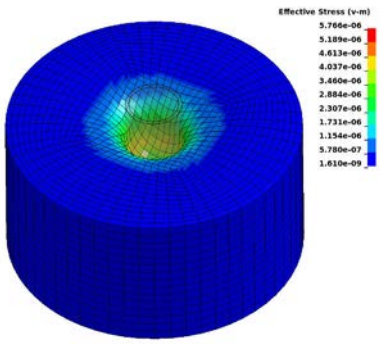

(b) Qualitative results with Neo-Hookean model

Figure 3.17: Charaterization of Sylgard 527

Models	Parameters					
Neo-Hookean	$C_1(MPa)$ $8.2020 \cdot 10^{-4}$					
Mooney-Rivlin	$C_{10}(MPa)$ $8.0018 \cdot 10^{-4}(MPa)$			$C_{01}(MPa)$ $1.39 \cdot 10^{-5}$		
Ogden	$\mu_1(MPa)$ $6.941 \cdot 10^{-6}$	$\alpha_1(-)$ 7.3825	$\mu_2(MPa)$ $1.143 \cdot 10^{-3}$	$\alpha_2(-)$ 2.33	$\mu_3(MPa)$ $9.0378 \cdot 10^{-5}$	$\alpha_3(-)$ 4.7443

Table 3.2: Hyperelastic parameters for Sylgard 527 gel models

Sensitivity study In such complex models of deep indentation needed hyperelastic laws involving one or more parameters provided a response. Unfortunately the relationship between the input parameter(s) and the output response was not clear and could be viewed as a black box. The sensitivity study was therefore a key point to guarantee the confidence in the modelling and its robustness. The sensitivity analysis led to point-out the most relevant and crucial parameters but showed if a parameter was useless as well. In this work a global sensitivity analysis method named One Factor at A Time method (OFAT) was used. This method consisted to change only one material parameter values around the optimal position from -10% to +10% and to observe how behaved the response. It could be concluded that the model was fair or not, was stable or not and if some parameters among the other were more sensitive. The response history could be plotted trough the input parameters. The evolutions were observed to be often linear, they were then approximated by a linear regression. The coefficients of the linear function were then taken as the sensitivity indices. The results of the sensitivity study was resumed in the table.

For the three models no parameter was very sensitive, the model could be judged unstable. The parameter C_{01} in the Mooney Rivlin model as well as the parameters α_1, μ_2 had very few influence. Therefore, spending too much time to find accurate values of these parameters was so useless.

In previous part, a hyperelastic model was calibrated upon indentation tests to represent the gel Sylgard 527 behavior. In order to ensure that the model was always eligible for higher velocities, an experience in dynamics was conducted. A FEM of the dynamics experience was then developed and the previous calibration gel model was used. The response between both the experiment and the numerical modelling were compared.

Experimental results validation The previous experiment was simulated on one hand to validate the modelling strategy and in other main to validate a Sylgard 527 material model.

Discretization The FEM (see Figure 3.18a) was composed of the gel cylinder, the vessel; four nodes representing the vessel markers and beams to connect the vessel marker to the vessel (see figure 3.18c). The vessel was discretized by 4572 3D Belytschko-Tsay shell elements. The cylinder of gel was discretized by 14512 constant stress solid elements and placed inside the internal vessel as show the figure 3.18b. In order to model the vessel marker, nodes located at the same position than in the experience were placed and connected to the inner vessel by rigid beams.

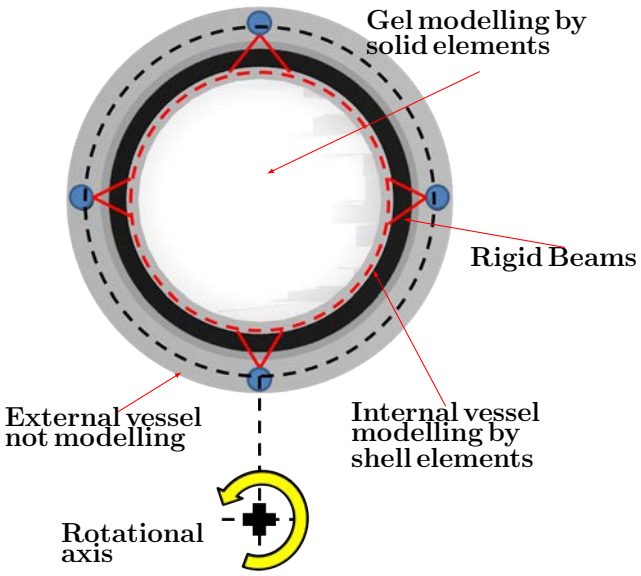

(a) Numerical modelling without water

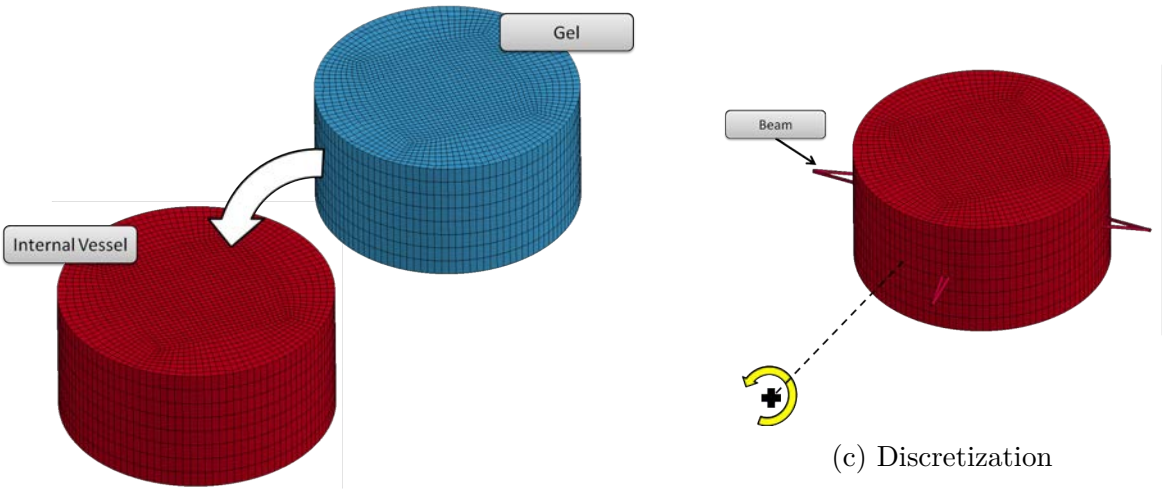

(b) Exploded view

(c) Discretization

Figure 3.18: Details of the numerical modelling without water

Material models The internal vessel was modelled using an elastic material model with a high young modulus to avoid all non-physical deformations. The beams were modelled using a rigid model as they did not influence the rest of the structure's behaviour. Contrary to the two previous one, the models which could be used to modelling the gel Sylgard 527 were highly discussed in the literature and led to a versatile range of model possibility.

Load cases and boundary conditions The angular displacement assessed in the experiment (see Figure 3.9a) was prescribed to the vessel by means of a LS-Dyna® option which allowed imposing nodes' rotation around an eccentric point. As in the experience, it was assumed that the gel was stacked to the vessel. Thus a contact based on penalty with a high friction coefficient was used.

The post processing consisted in tracking the history of the gel marker displacements and to comparing them with the measurements. In order to facilitate this post processing, each gel marker corresponded to one node in the FEM. As in the experience, the nodal displacement was not more observed by the fixed coordinate system but rather by a local coordinate system designed by the vessel markers.

Validation of the new material model In order to validate the material models, the three previously calibrated hyperelastic models were used in the cylindrical transient FE model. The responses were then compared to the experimental results. Among the 52 gel markers,

the comparison was completed on the same 6 gel markers as indicated in the previous section. Exactly like the previous section the curves were the history of displacements through the time. Two principal parts could be distinguished (see figure 3.19). The first peak, corresponded to the lag of the gel behind the vessel, it was very accurately fitted. The second part was either a second peak or a more constant phase corresponded to the elastic come-back of the gel. This second part depicted generally a good agreement.

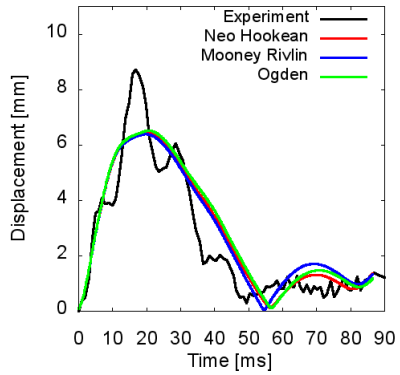

(a) Marker 1

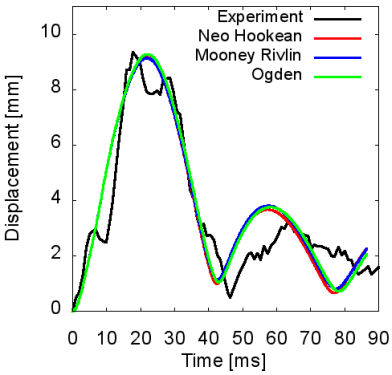

(b) Marker 2

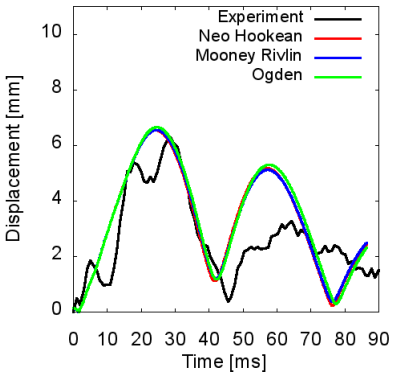

(c) Marker 3

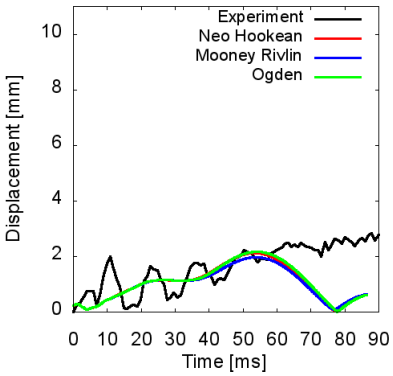

(d) Marker 4

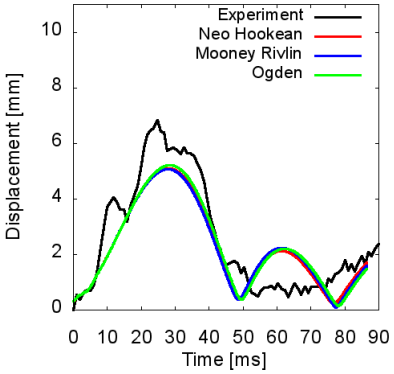

(e) Marker 5

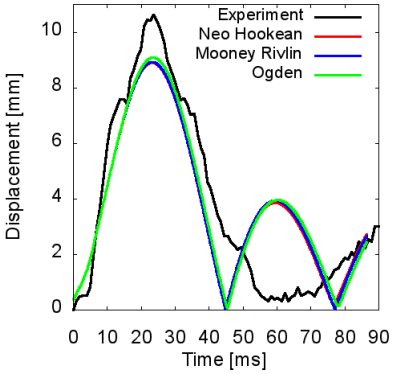

(f) Marker 6

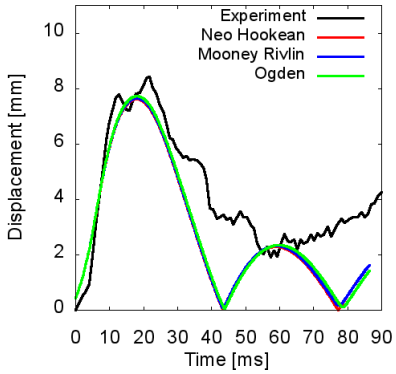

(g) Marker 7

Figure 3.19: Comparisons experiments vs simulation for models' validation

As 52 gel markers were studied, an objective criterion had to be found to assess the accuracy of the model prediction regarding the experimental results. The chosen criterion was based on the difference between the experimental and the numerical curves' areas (resp. A_{Exp} and A_{Num}) approximated by the trapezoidal rule. This error (ϵ) was expressed in percentage and was computed using the equation below.

$$\epsilon = \frac{A_{Exp} - A_{Num}}{A_{Exp}} 100 \tag{3.8}$$

For each gel marker an error was then evaluated. The interpolation between the gel markers errors led to a 3D surface. This surface represented the repartition of the error and allowed a global and better understanding of the structural response behavior; all three surfaces are shown in figure 3.20 as contour plots.

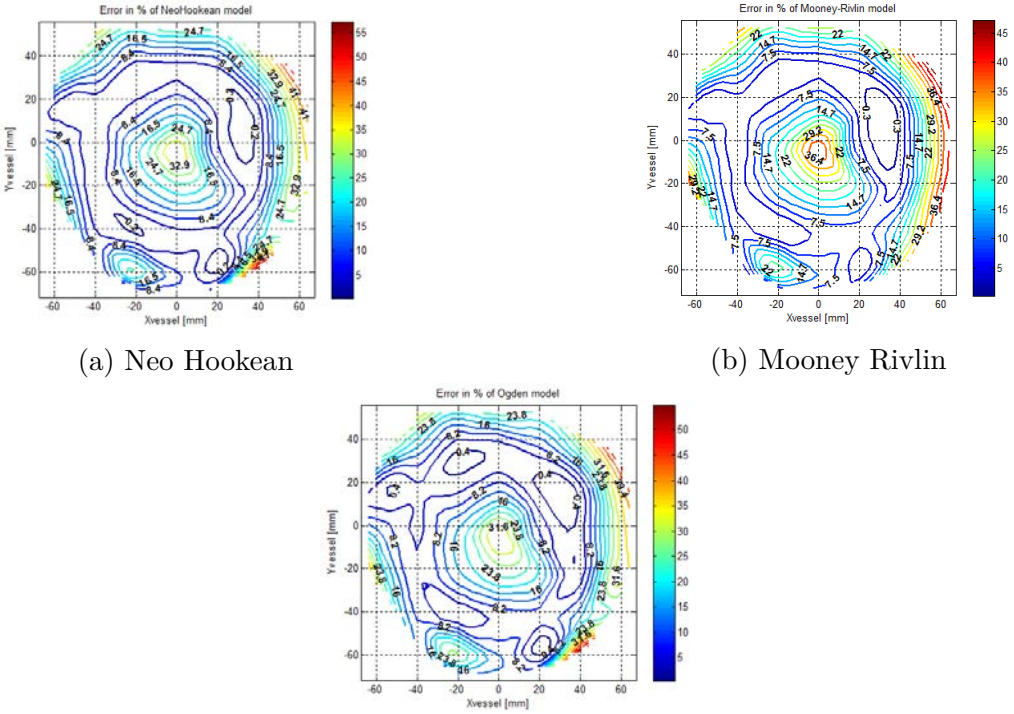

(a) Neo Hookean

(b) Mooney Rivlin

(c) Ogden

Figure 3.20: Error contour plots of different material models

The three contour plots errors were approximately similar. From the contour plots it could be observed that the main errors were located on the boundary and on the center. Firstly, on the corners the experimental curves of gel markers depicted singularities regarding the other curves. This phenomenon could be explained by the difficulties for the optical measurement

device to distinguish accurately the gel markers and the vessel boundary. Secondly, on the center of the gel cylinder the distortions were so high that the gap between two gel markers in a row became too small and the optical devices mixed the markers. The displacement's curves of gel makers around the center were therefore singular as well. In order to decide whether the errors were acceptable or not a statistical study was completed. Taking the 52 errors' values as sample, the first and third quartiles as well as the mean value are assessed and schematized on a box plot for the three hyperelastic models (see figure 3.21).

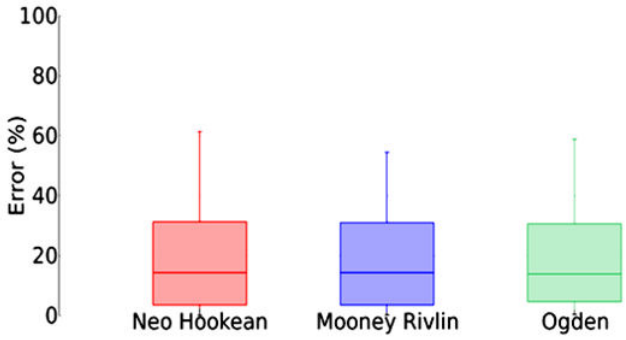

Figure 3.21: Error comparison between the three material models

3.3.2 Model with water

Subsequently to the modelling of the dynamical test without water, the configuration with water is investigated. The complexity of the situation is enhanced by addition of a fluid layer between the gel and the external vessel. Because the soft material model is now fair, the modelling of this configuration should assess the ability of prediction in case of a soft materials interacted with a fluid.

Firstly the coupling schemes proposed by LS-Dyna is presented. Then, the modelling of the cylindrical test with water is described and finally the results are discussed.

Fluid-structure interactions using LS-Dyna facilities

The FSI modelling was performed using ICFD solver of LS-Dyna. The ICFD module is available from the R7 version and is based on an implicit computational fluid software using the finite element discretization.

ICFD could be coupled with the classic solid module to undertake fluid-structure coupling problems. Two partitioned procedures are available either an explicit coupling (see figure 3.22a) when the problem is weak or an implicit coupling (see figure 3.22b) when the problem is

strong. A boundary-fitting method was used and the fluid mesh follows therefore the structure deformation by means of an ALE approach. As explained in the second chapter such method allows to represent accurately the boundary conditions through the fluid-structure interface. Nevertheless high fluid mesh distortion could result, an adaptively remeshing procedure was therefore achieved to overcame this issue. The coupling could be a one or a two way coupling. Regarding the explicit coupling scheme, no iteration were undertaken. The solid time integration is explicit while the fluid is implicit, the solid time step is then smaller than the fluid one and the fluid mesh is updated accordingly to the solids displacement only at each fluid time step.

The implicit coupling scheme offers an iterative procedure to increase the accuracy. The solid time integration is implicit and the fluid remains implicit. The coupling time step is the smaller between the solid and the fluid time steps. The convergence of the computation can be assessed by the solid internal energy evolution. Once the internal energy is constant, the convergence was reached and the next time step can be started.

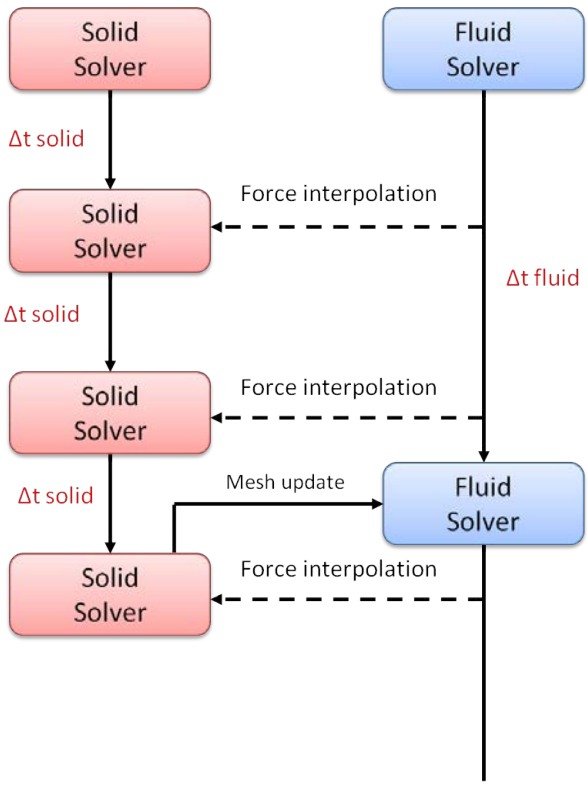

(a) Explicit

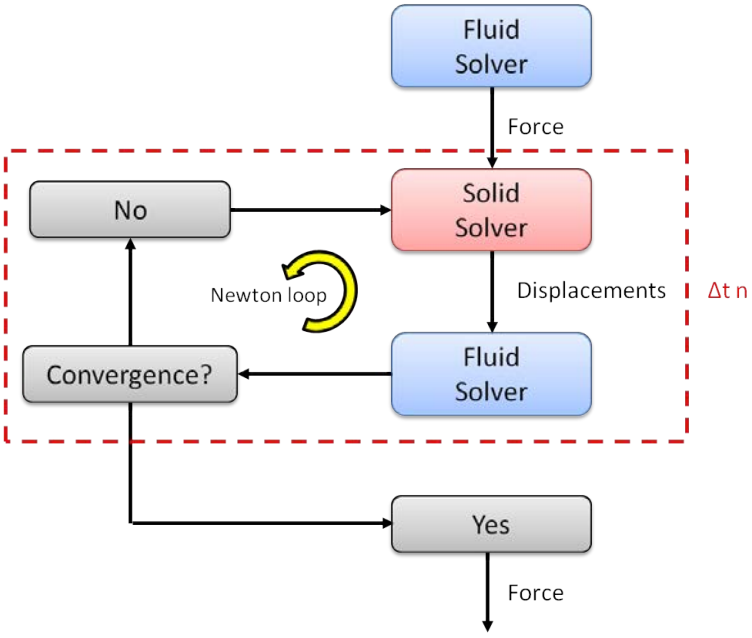

(b) Implicit

Figure 3.22: ICFD coupling schemes available in LS-Dyna 971 R7 and above

as ICFD deals with incompressible flow, the incompressibility assumption of the studying

situation has to be check. The compressible effects appear mainly in case of high fluid velocity and they correspond to a shock wave propagation. In order to evaluate whether the compressible effects have to be taken into account or not, the Mach number Ma was computed (see eq. 3.9) and must remains under 0.3 to validate the incompressibility assumption.

$$Ma = \frac{V}{a} \tag{3.9}$$

where V is the fluid velocity and a is the sound celerity in the media.

Methods

Discretization From the innermost to the outermost, the model was composed of the gel block, the water layer and the external vessel respectively (see Figure 3.23). The external vessel as well as the plexiglass cover were discretized as an unique part by 984 3D Belitchko-Tsay shells. The spatial discretization was achieved to ensure that nodes were located on the same position than the vessel markers in the experiments.
The fluid mesh was composed of an unstructured grid composed of 26854 tetrahedral elements.

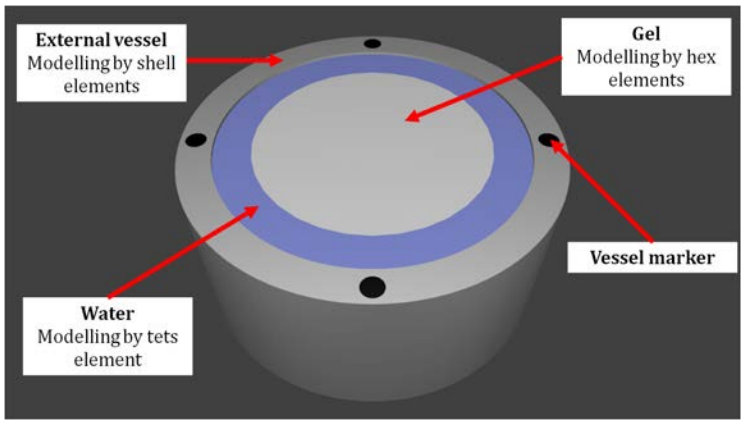

(a) Discretization

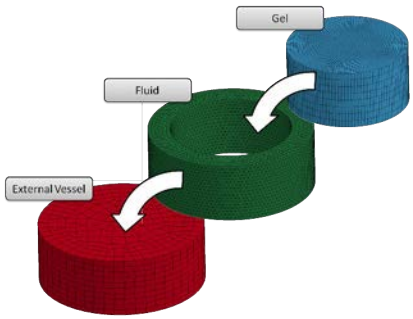

(b) Exploded view

Figure 3.23: Details of the numerical modelling including water

Material models The gel models which has been characterized and calibrated in the section 3.3.1 are used in this section (see Table 3.2). The vessel was modelled using an elastic model with high Young modulus. Because the flow remains incompressible, the fluid was modelled using a linear Stockes law where the dynamic viscosity $\mu = 1.002 * 10^{-3} Pa.s$ and the density $\rho = 998.2 Kg/m^3$ was taken at $20°C$

Load cases and interactions The rotational displacement recorded on the experiments (see figure 3.9a) was prescribed on the external vessel by means of the same method than the model without water. As in the experience and in the model without water, it is assumed that the gel is glued to the vessel. Thus a contact based on penalty with a high friction coefficient was used for the lower and upper faces.

The fluid interacts with the vessel and the gel. At the same time, the fluid structure interactions are achieved in the two ways, i.e. the fluid acts with a pressure on the solid and the solid acts with its motion on the fluid. The mesh motion was monitored by the resolution of a linear elastic problem where the stiffness were proportional to the element sizes.

Results and discussion

The gel displacements predicted by the numerical model were compared to the experimental results already outlined in the paragraph 3.2.2.

Unfortunately, whatever the hyperelastic gel models used among the previously calibrated models, the fluid-structure interaction simulations lead always to important instabilities and were not able to converge. The qualitative representations of the results just divergence are presented in figure 3.24 for the Ogden model which behaves similarly with the two other hyperelastic gel models. From figure 3.24 one can observe the gel and the external vessel are shown respectively in blue and red with transparency. In order to be able to see the gel deformation, the water is not represented. The figure 3.24 shows an important distortion of the gel mesh and probably hourglass effect which makes the numerical simulation diverging.

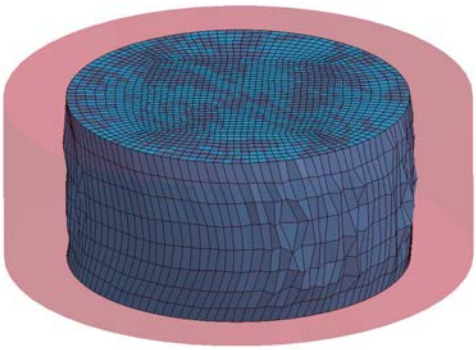

Figure 3.24: Numerical instability of fluid-structure interaction using Ogden material model for the gel

This issue led to some questions, Is the instability stems from the fluid-structure interaction

treatments? Is the instability are due to the mesh motion procedure? In order to understand the reason of this instability, a parametric sensitivity was achieved and presented by a set of histograms graphics. The total simulation time was fixed to $110ms$, the histograms summarize the achieved computation time before that the instability occurs. The first conclusion is the sensitivity of the simulation regarding all parameters and the second, is the effect of each parameter, e.g. if a parameter improves the stability, the instability occurs later and conversely. This parametric study was carried-out using the previously presented model with the gel calibrated model Ogden.

Fluid viscosity In the parametric study the fluid viscosity was varied from the water viscosity $0.001Pa.s$ to a very high value $100Pa.s$. The results are summarized in the figure 3.25.

One can notice, for all value of the viscosity, the stabilityseems to be not affected. The viscosity is therefore not a sensitive parameter.

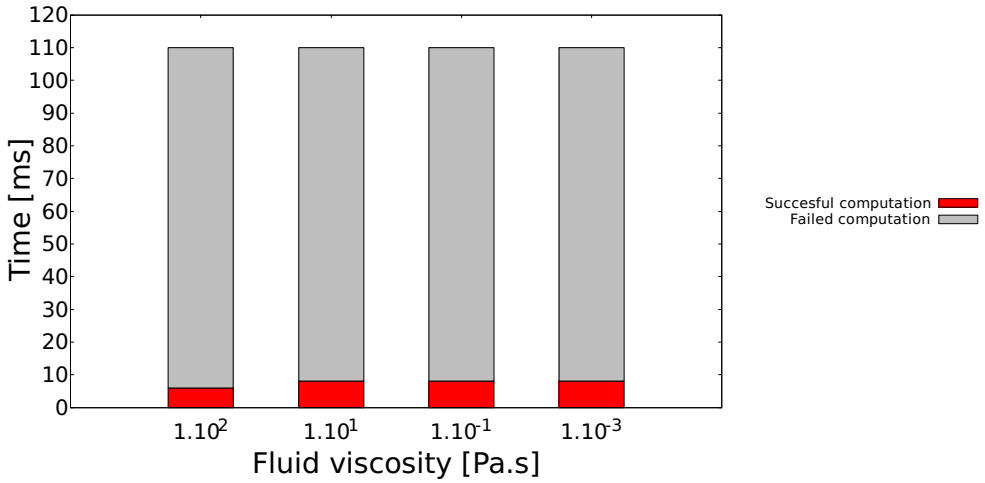

Figure 3.25: Fluid viscosity influence

Fluid and solid densities Based on the literature survey, the second chapter has shown that the added mass effects may lead to instabilities and are monitoring by the ratio between the fluid density ρ_f and the solid density ρ_s. The density ratios are crucial parameters regarding the stability of the partitioned coupling schemes and should be investigated.

A sensitivity study was carried-out to investigate the influence of both densities of the fluid and of the solid. A design of numerical experiments had been built and shown in table 3.3 it is divide in two parts firstly only the fluid density ρ_f is variable while ρ_s remains constant

then only the solid density evolved ρ_s is variable while ρ_f remains constant. It is important to remark that the same density ratios were used in the two parts of the design of experience.

Fluid density			
$\rho_s \ [Kg/m^3]$	970		
$\rho_f \ [Kg/m^3]$	10^4	10^3	10^2
$\frac{\rho_f}{\rho_s} \ [-]$	10.3	1.03	0.1

Solid density			
$\rho_f \ [Kg/m^3]$	10^3		
$\rho_s \ [Kg/m^3]$	97	970	9700
$\frac{\rho_f}{\rho_s} \ [-]$	10.3	1.03	0.1

Table 3.3: Design of experiment for density influence

The results are summarized in figure 3.26.

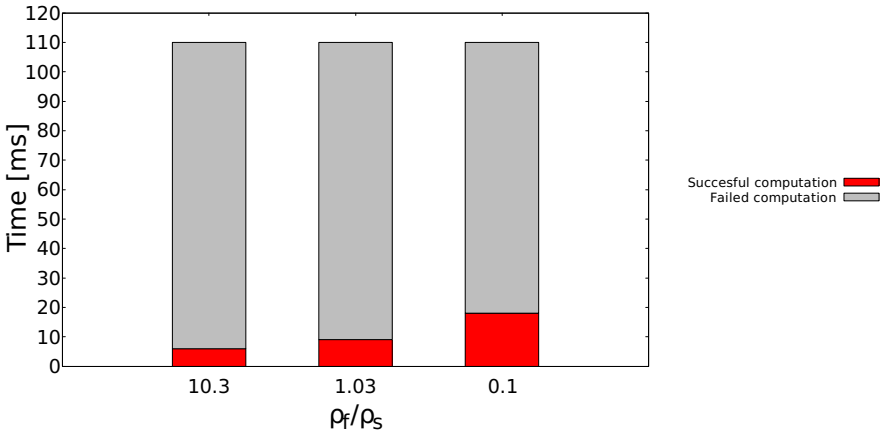

(a) Fluid density evolution

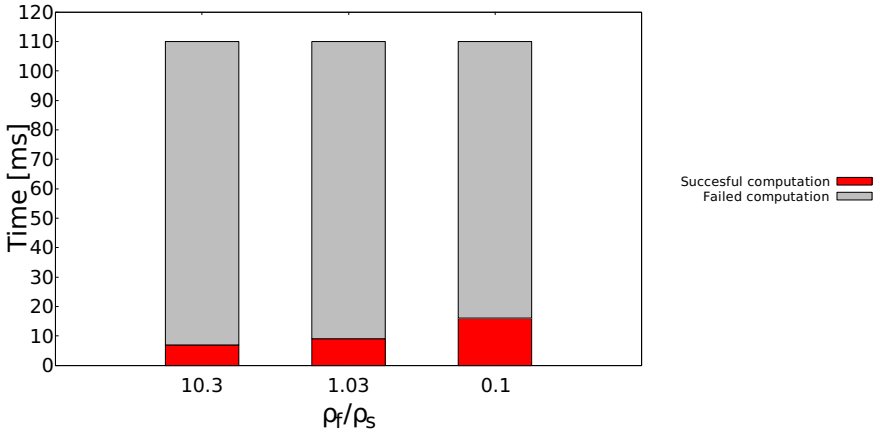

(b) Solid density evolution

Figure 3.26: Ratio's densities influence

Regarding the results a couple of interesting answers could be done. Firstly, whatever the fluid or the solid densities the really most important parameter is the density ratio. This conclusion is frequently underlined in the literature [Song et al., 2013] [Banks et al., 2014]. Nevertheless, several authors conclude that a threshold of density ratio could be found equal to 1. In the present case even for a ratio of 0.1 and smaller, the modelling crashes. A deeper study of the instability source has therefore to be investigated. As illustrated in figure 3.27, dealing with this density's ratios the reason of the crash is no more the mesh distortion but rather the impact of the gel against the external vessel leading to mesh distortion and contact problem as well. In addition in the experiments the external vessel is never impacted by the gel.

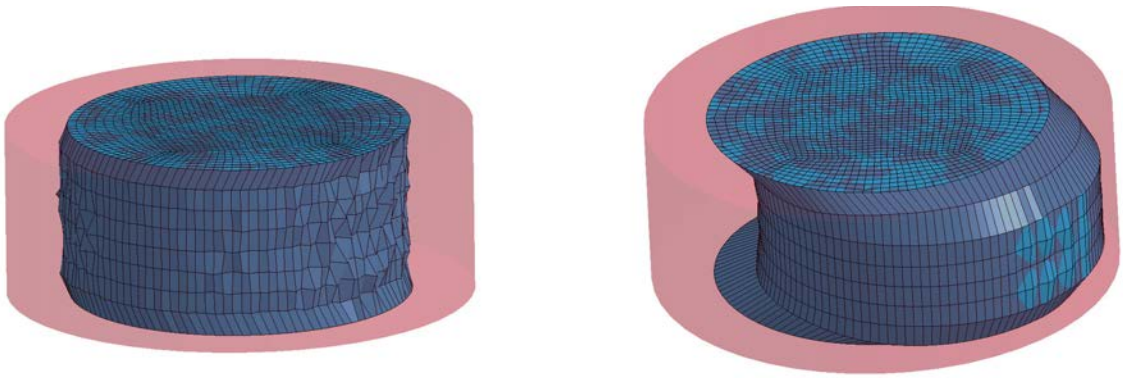

(a) High density ratio: Added mass and hourglass effects

(b) Small density ratios: Unexpected contact between vessel and gel

Figure 3.27: Numerical instability of fluid-structure computation

Solid stiffness The second chapter has indicated that the coupling stability could be difficult to reach if soft materials are involved. A parametric study has been carried-out. The solid Young's modulus is ranged from the Sylgard one, i.e. $2.5 \cdot 10^{-3} MPa$ to $2.5 MPa$. The results are represented in the graphic 3.28.

The results fit well with the expectations. The stiffer materials introduce less deformations and displacements and assure a better stability.

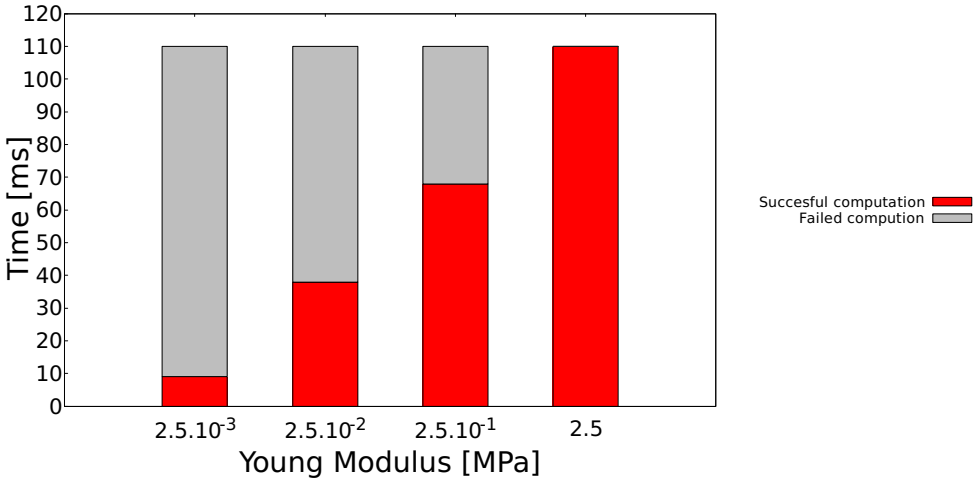

Figure 3.28: Influence of Young modulus on the numerical stability

3.4 Conclusion

Because the traumatic brain injury remains a real society burden, we have proposed to study the human head to improve the understanding of the brain injuries. A anatomic study has been performed and has shown that between the brain and the skull there is a gap of about 3 mm called the meninges which are essentially filled by cerebrospinal fluid. Due to this gap the brain is relatively free to move inside the skull. It has been shown that this relative motion contributes to improve the brain injury criteria. Therefore, a physical human head model has been developed by [Hault-Dubrulle, 2007] to demonstrate that the CSF strongly influences the brain motion for the case of a dynamical load.

In the physical model, a dynamical rotational load case has been prescribed to a brain material substitute commonly used in the literature, the silicon gel Sylgard 527. The benchmark is used at two stages: firstly, an initial version dealing only with gel, with the objective to validates the material modelling of the biomaterial. Secondly, an improved version including to improve the fluid-structure numerical methods. The investigation carried-out in this chapter have been split in two parts.

Firstly, based on a developed macro indentation experiment and on an inverse numerical characterization method, the Sylgard 527 gel has been characterized using hyperelastic material models. This proposed new gel models have been validated based on the dynamical experiment. Secondly, based on the same dynamical rotational experience a fluid layer has been added around the gel in order to mimic a more realistic head behaviour. This fluid layer modified

the boundary conditions and imposed a fluid-structure interaction situation. The previously characterized material has been used to model the Sylgard 527 gel and an implicit partitioned scheme has been used to model the fluid-structure interactions. It has been shown that the instabilities cannot be avoided. Firstly due to the fact that the fluid and solid density are closed, added mass effect can appear leading to instabilities. Secondly, the dynamical load case induces high impulses. The soft material which exhibit important displacements leading further more accelerations. Nevertheless, only implicit treatment of the fluid is available with ICFD in LS-Dyna, which is not recommended for high accelerations.

The next chapter will investigates the development of an in-house coupling code which is able to deal with fluid-structure interaction involving dynamical load cases and soft materials.

4 Implementation of a fluid-structure interactions computational code validated on experiments

Contents

4.1 Introduction

In order to emphasize the performance of the fluid-structure simulation techniques in dynamics involving soft materials for biomechanical applications, a dynamical experiment has been carried-out as shown in chapter 3. The experiment has been modelled by two LS-Dyna fluid-structure interaction methods. Unfortunately, none of them has managed to accomplish a correct modelling. Based on this results, it has been made the decision to create an in-house fluid-structure interaction solver to model this dynamical experiment. This code aims to be easily updated and improved. It has to be versatile to solve simulation problems in the laboratory either in biomechanics or in other fields.

The choice of the coupling strategy for the fluid-structure interaction solver is a crucial choice and has to be argued. The second chapter is the root of this argumentation. The biomehcanical applications require an accurate fluid prediction around the wet boundaries. In addition, the solver has to be easily updated. Based on the requirements and on the second chapter conclusions, a partitioned coupling scheme with boundary fitting method seems to be the most adequate and has been chosen in the present work. The partitioned coupling scheme needs two solvers, a fluid and a solid. The solid solver used is LS-Dyna as already used in the previous chapter. LS-Dyna is a good candidate because it is versatile and already well established in addition it offers the possibility to performed simulations by means of a set of keywords which could be written in any plain text editors, this possibility is very attractive to manage the data exchange completed by the coupling solver. The fluid code is the open source OpenFOAM. OpenFOAM has been chosen because it is free, open sources and it deals with numerous fluid and turbulence models as well. A stand-alone middleware between OpenFOAM 2.3 and LS-Dyna-R7 has been implemented in C++ to accomplish the coupling. The creation of such a C++ interface is very advantageous as they allowed to keep reusable fluid and structure computational codes which permits their independences moreover the two codes could always be updated as long as the input/output file's structures do not evolved.

Prior to model the dynamical experiment of the previous chapter, the developed coupled solver has to be created step by step. In order to accomplish a robust solver each step has to be validated. A specific experience is therefore proposed in this chapter to validate the fluid-structure interaction coupling code.

The first part of this chapter is devoted to the first developments of the coupling solver using

C++ programming language. In order to validate this first step, a very attractive fluid-structure experiment has been carried-out in a wind channel. The experience is presented in the second section of the present chapter. In the third section the implemented coupling solver is validated using the wind channel experiment. The results of this validation test lead to a couple of conclusions very useful for the improvement and the enhancement of the in-house coupling solver.

4.2 Baseline of a fluid-structure interaction solver

The baseline of the coupling solver deals with the finite-volume solver OpenFOAM 2.3 and finite-element solver LS-Dyna-R7 to compute respectively the fluid and the solid media. The solid is modelled from static to dynamic including geometrical and material non-linearities. The fluid is considered as incompressible turbulent and steady. In order to perform such fluid computation the solver simpleFOAM is used.

In this section, the numerical resolution of the solid and fluid problem is firstly presented. Subsequently, the choices of the temporal and spatial coupling as well as the mesh updating procedure are discussed. This section will end by presenting the C++ solver implementation facilities.

4.2.1 Numerical resolutions

Flow solver

The flow solver aims to compute the pressure and velocity field by the solving the continuity and momentum equations of the fluid (see eq. 2.6 and 2.7). Nevertheless, the resolution is not straightforward because the pressure is a source term in the momentum equation and is a-priori unknown. An additional pressure equation has to be used in order to calculate the pressure field. It is obtained by applying the divergence on the momentum equation and by introducing the result into the continuity equation, thus the two equations are coupled. Pressure equation from the work of [Ferziger and Peric, 2012], using the Einstein notation for simplicity, can be stated as:

$$\nabla^2 p = \rho \frac{\partial}{\partial} \left[\frac{\partial u_i u_j}{x_j} \right] \tag{4.1}$$

The SIMPLE (Semi Implicit Method for Pressure Linked Equations) algorithm is an iterative procedure developed by [Patankar and Spalding, 1972] based on the velocity and pressure correction [Mangani and Bianchini, 2007], its procedure reads as:

- Initialize the pressure field p_0
- Solve the momentum equation to compute an intermediate velocity field u_0
- Solve the pressure equation to obtain $p^{'}$
- Update the pressure and velocity fields: $p = p_0 + p^{'}$ and $\overrightarrow{u} = \overrightarrow{u_0} - \frac{\Delta t}{\rho} \overrightarrow{\nabla p^{'}}$
- Repeat the step 2, 3 and 4 until convergence

Solid solver

Based on the theoritical manual of LS-Dyna [Hallquist et al., 2006] a good overview of the explicit and implicit time integration schemes are done.
The objective is to solve the momentum equation 2.2. In order to solve the momentum equation 2.2 and assuming that the damping term can be neglected, the matrix form is used (see equation 4.2). It is a non-linear ordinary differential equation which can be solved only by numerical devices.

$$[M] \overrightarrow{\ddot{u}_s} = \overrightarrow{P} - \overrightarrow{F(u)} \tag{4.2}$$

where $\overrightarrow{u_s}$ is the solid displacement, F is commonly call the internal force and are a non-linear function of the displacement $[M]$ is the mass matrix. The basic problem is to determine the displacement u_{n+1} at time $t_{n+1} = t_n + \Delta t$. The explicit and implicit method used in LS-Dyna are presented subsequently.

Explicit An key assumption for the explicit scheme is that all the terms are known at time states n. LS-Dyna used the central difference time integration to move forward $t_{n+1}t$ the semi-discrete equation where the hourglass term is not taking into account:

$$[M]\,\overrightarrow{\ddot{u}_s^n} = \overrightarrow{P^n} - \overrightarrow{F^n} \tag{4.3}$$

where $[M]$ is the diagonal mass matrix, $\overrightarrow{P^n}$ account for the external and body forces load, F^n is the internal force vector.

The central difference scheme is then:

$$\overrightarrow{\ddot{u}_s^n} = [M]^{-1}\left(\overrightarrow{P^n} - \overrightarrow{F^n}\right) \tag{4.4}$$

$$\overrightarrow{\dot{u}_s}^{n+1/2} = \overrightarrow{\dot{u}_s}^{n-1/2} + \overrightarrow{\ddot{u}_s}^{n}\Delta t^n \tag{4.5}$$

$$\overrightarrow{u_s^{n+1}} = \overrightarrow{u_s}^n + \overrightarrow{\dot{u}_s}^{n+1/2}\Delta t^{n+1/2} \tag{4.6}$$

where

$$\Delta t^{n+1/2} = \frac{(\Delta t^n + \Delta t^{n+1})}{2} \tag{4.7}$$

The geometry is then updated with respect to the initial state

$$\overrightarrow{x^{n+1}} = \overrightarrow{x^0} + \overrightarrow{u^{n+1}} \tag{4.8}$$

where x is the nodal position.

Implicit The implicit integration time is an iterative scheme able to simulate the static, the quasi-static and the dynamics involving low frequency problems. In this work the implicit method is used to solve quasi-static or static problems where the inertial terms are neglected. Without the inertial terms the solved equation 4.3 becomes:

$$\overrightarrow{R}\,(u_s^n) = \overrightarrow{P^n} - \overrightarrow{F^n} = \overrightarrow{0} \tag{4.9}$$

where $\overrightarrow{R}$ is called the residual.

The term $\overrightarrow{u_s}^{n+1}$ is calculated to solve the equation $\overrightarrow{R}\,(u_s^{n+1}) = \overrightarrow{0}$.

Under linear assumption the term $\overrightarrow{R}\,(u_s^{n+1})$ could be approximated by the first order Taylor

developments.

$$\overrightarrow{R}\left(u_s^{n+1}\right) = \overrightarrow{R}\left(u_s^n\right) + \left[\frac{dR}{u_s^n}\right] \cdot \overrightarrow{du_s}^n = 0 \tag{4.10}$$

A linear equation system has to be solved.

$$[K_t] \cdot \overrightarrow{du_s}^n = -\overrightarrow{R}\left(u_s^n\right) \tag{4.11}$$

where $[K_t] = \left[\frac{dR}{u_s^n}\right]$ is the tangent matrix.
Eight quasi Newton methods and one Newton method are available in LS-Dyna to solve the linear system. The Newton methods are more robust while the quasi-Newton requires fewer iterations.

4.2.2 Coupling scheme

At this time, each of the domains can be solved by the equation of the section 4.2.1. Now, based on the chapter 2, the results of fluid and solid solvers have to be exchanged between the solvers in a partitioned coupling. The temporal and spatial coupling strategies as well as the mesh up-date procedure used in the implemented coupling code will be presented.

Temporal coupling

Implemented temporal coupling An iterative coupling scheme enhanced by a convergence criterion as already pointed-out in 2.6.3 is used. A fully coupling simulation is required to guaranty as much as possible the respect of the coupling conditions 2.12 and 2.13 and insure the energy conservation through the wet-boundary. In addition, the iterative scheme decreases the undesirable added-mass effects (see paragraph 2.6.2).
In order to carry out the non-linear iterative resolution several methods are usually found in the literature, the fixed-point method or the block-Newton method. Conversely to the block-Newton method, the fixed-point method is more relevant in this work as it is able to converge to stable solution without any intervention in the computational codes. The principal of black-boxes is therefore firmly maintained.
The strong coupling scheme used in the present work is illustrated in figure 4.1. Unless the fixed-point converges slowly, it is frequently used. In order to improve the convergence rate some methods can enhance the scheme such as the Aitken relaxation methods.

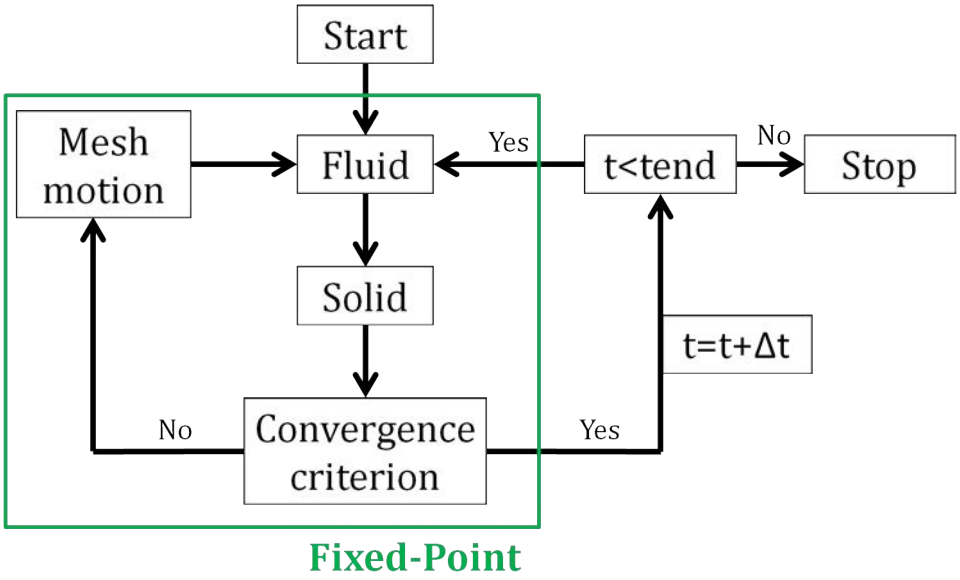

Figure 4.1: Strong coupling scheme

Convergence Criterion In the literature a wide choice of convergence criterion can be found. The internal energy variation of the structure is taken as convergence criterion (see equation 4.12). For all the sub-iterations inside the fixed-point block the variation of the current internal energy E_{int}^{i} regarding the internal energy of the previous sub-iteration E_{int}^{i-1} is assessed, if the variation is small enough (less than ϵ_{FSI}) the iterative procedure is considered as completed.

$$\frac{|E_{int}^{i} - E_{int}^{i-1}|}{E_{int}^{i}} < \epsilon_{FSI} \tag{4.12}$$

Spatial coupling and Mesh updating procedure

It is reminded that, when the fluid-structure interaction problems are treated by a partitioned scheme, the structure was deformed by the fluid pressures acting on the wet-boundary and once the structure is deformed the mesh motion solver has to accommodate the fluid mesh to fit the structure while a good fluid mesh quality is required.

The data are exchanged between the fluid and solid elements through the wet boundary by means of the spatial coupling. For the moment, the fluid and solid meshes are conformed (see Figure 2.4a). The data transfer are readily carried-out from nodes-to-nodes. This method is very basic but it is quickly limited as already mentioned in 2.5.1. The implementation of an additional module to deal with non-conforming meshes is planned but by lack of time is still

not implemented.

The accommodation of the fluid mesh to the structure one is implemented based on the RBF method presented in 2.5.1. This method, close to the meshless methods, spreads the nodal wet-boundary displacement on a wide part of the fluid mesh (see Figure 4.2). The interface displacement is prescribed on the fluid vertices regarding a non-uniform pattern monitoring by a weighting function. Indeed, for the vertices situated on the fluid-structure interface the weighting function is equal to the unity whereas a zero value is enforced for the vertices located further a specified radius. The evolution of the weighting function between the two ends has to be well investigated by the Users. For instance if the weighting function is linear, the only parameter which is required as input is the "spreading" parameter (see Figure 4.2d). Regarding the simulation, the spreading parameter is the radius of the circle in 2D, or of the sphere in 3D, where the mesh vertices are allowed to move.

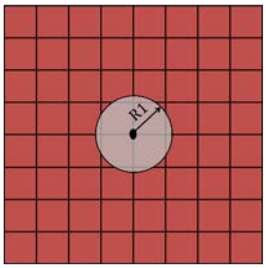

(a) Radius R1

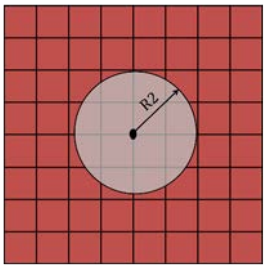

(b) Radius R2

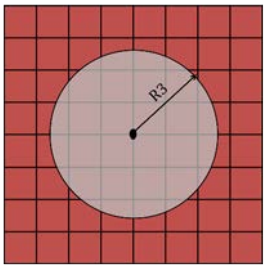

(c) Radius R3

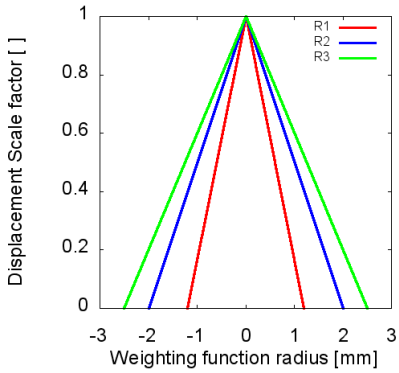

(d) Weighting functions

Figure 4.2: Mesh motion: linear weighting function

4.2.3 Implementation of the coupling scheme

The coupling strategy has been presented in the previous section, its numerical implementation is undertaken in this section. The coupling algorithm consists in a middleware composed of a main class called *FSI*, composed of header *FSI.h* and source file *FSI.cpp*. The FSI class is

composed of members and attributes but it has access to two other classes called *solid* and *fluid* (see figure 4.3). All the required data are brought by the Fluid and Solid objects respectively created by the classes *fluid* and *solid*. The next section details all key functions xhich are used by the *FSI*, *solid* and *fluid* classes.

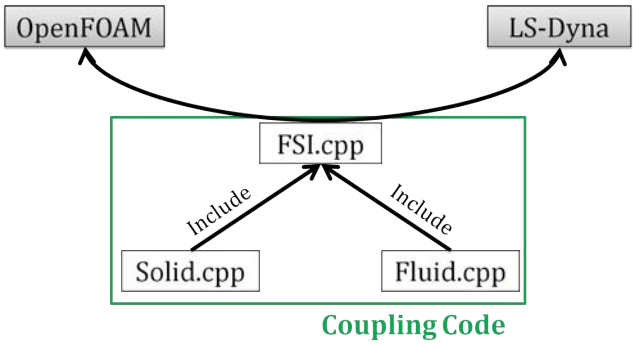

Figure 4.3: C++ coupling interface

Class members needed by solid solver

The solid class performs the operations which take place only in the structure computation, its members are listed below.

meshSave records in a table the initial nodes localizations as well as the grid. It searches the node belonging to the fluid-structure interface and saves them in an other table.

fluidStressToForce reads the fluid stresses and transforms pressure into force terms regarding the surface of the finite element faces.

readDisplacement reads the displacements of the fluid-structure interface nodes.

Class members needed by fluid solver

The fluid class performs the operations which are necessary only in the fluid computation, its members are listed below.

meshSave records in table the initial node fluid mesh position as well as the grid belonging to the fluid-structure interface and saves them in a other matrix.

boundaryNodes searches for the vertices located on the fluid domain boundaries which are not connected to the wet-boundary. In order to perform the mesh motion this fluid boundary vertices domain has to be specified and fixed.

meshUpDate reads the fluid-structure interface node displacements and prescribes the new positions of the fluid vertices concerned by the mesh updating procedure. It creates a file linked each fluid vertices to its displacement, this file can be read by the visualization application "Paraview" to check accurately the mesh updating effects.

Class member needed by the fluid-structure interactions

setUpFolder creates all the folders, fluid and solid, needed to record the coupling evolution during the time. These folders contain results like pressure or displacements. They are used to transfer the data through subsequent iterations and time steps.

transferMatrix reads the matrix fluid-structure interface of the fluid and the solid, then by identification carry-out a transformation matrix to enable data transfer from fluid to solid and conversely from the solid to the fluid.

simulationLauncher launches the openFOAM as well as the LS-Dyna simulations once the inputs data is done.

inputSetUp writes the fluid and solid input files. For the solid the loading conditions (forces) are written in a separated file (laodCase.k) as well as the updated mesh (mesh.k) and the previous displacement of the fluid-structure interface nodes (displacement.k).
Regarding the fluid input data, the vertices localization are rewritten as well as the previous velocity and pressure fields in the files boundary/polyForm/node, time/u and time/p respectively. Finally, the starting time and the simulation duration for the fluid computation have to be modified in the the file system/constant if several fluid-structure interactions are completed through the whole computational time.

convergenceThreshold computes the convergence criterion and assessed whether the criterion is satisfied or not.

4.3 Experimental benchmark for the validation of fluid-structure modelling

In order to perform a first validation of the previously implemented fluid-structure interaction computational code, an experimental test has been carried-out but this experiment is devoted to validate any fluid-structure interaction coupling code. It consists in a plate which is deformed by an air flow. Among all the experimental fluid-structure interaction situations which can be performed, this one is chosen because of two main reasons. Firstly, it was due to the lack in finding experimental fluid-structure results to be used for comparison and validation purpose. The author wishes therefore to provide useful results to validate the numerical predictions. Secondly, this experimental facilities lead to an easy and fairly modelling, without any doubt about some modelling parts like the boundary conditions prescription or the material models. In this section, the experimental set-up are presented as well as the measure facilities. Then, the procedure to create the structure is detailed and finally the results expressed in terms of fluid velocity field and structure bending are discussed.

4.3.1 Experimental set-up

Subsonic wind tunnel

The experiment was carried-out in a close subsonic wind tunnel (see figure 4.4). It depicts a square section of 5m*5m followed by the test section of 10 m long with a square section of 2m*2m. A fan of 4.8m diameter is powered by a 200 kW electric motor is enable to enforce an air velocity until 60 m/s out of the boundary layer with a flow rate of 240 m^3/s. In this work, the inlet velocity (U_0) is fixed to $5m/s$, nonetheless higher velocity is attempted to be investigated later. The turbulence intensity assessed by an empty test section was about 0.5%. The free stream turbulence is controlled by a honeycomb wall located some meters before the test section. The wind tunnel floor is made of wood leading to an easy fixation of the structure.

Figure 4.4: Subsonic wind channel

Structural support

The structural device support aims to maintain the basis of the structure (plate) on the floor and has to be able to use a range of plates with variable thickness. In the present effort the pate measure $1m/20cm/5cm$. The device was made to fix the plate is presented in the figure 4.5.

It is composed of two steel corners which are able to slide by means of three normal slide links. The corners are fixed to the slide links by means of bolt/washer systems. Through the vertical sides of the corners a couple of holes were drilled to allow screwing the basis of the plate on the corners. A thin aluminium plate bended on its two edges was added to close the front and the rear of the apparatus avoiding all turbulences under the testing plate.

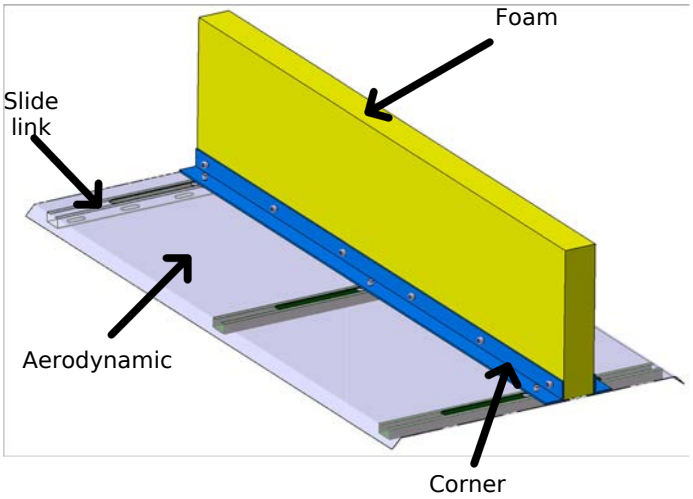

Figure 4.5: Structural devices

Measurement facilities

Two parameters were measured, related to the fluid namely the velocity field around the plate and related to the structural, namely the deflection of the plate.

In order to measure and observe the velocity field, the "Particle Image Velocimetry" method (PIV) has been used. The PIV chain of measure is essentially composed of a laser and a camera, its introduction into the wind channel is shown in figure 4.6. The flow chart of the PIV method is presented in figure 4.7. It consists in seeding the flow by tracer particles and to follow the particles to visualize the velocity field. The particles are about $2.510^{-6}m$ diameter. A synchronisation device trig simultaneously a laser pulse and the camera acquisition. The laser produces a short duration laser plan while the camera was recording. The synchronizer forces a group of two impulsions separated by a short time interval of Δt leading to two temporally closed images of the flow. The two images are compared and by means of cross-correlation method the displacement and then the velocity of the seeding particles are localized. The operation is repeated during all test duration to get the dynamical evolution of the velocity field.

The commercial package TSI® is used to perform the PIV measurements and the data treatments are carried-out by the software Insight®3G. In order to catch the two subsequent pictures the double laser pulse is produced by a ND-YAG with a wave length of 532 nm (green) and a frequency of 7.25Hk. The laser pulse produces an energy of 200mJ for 8ns.

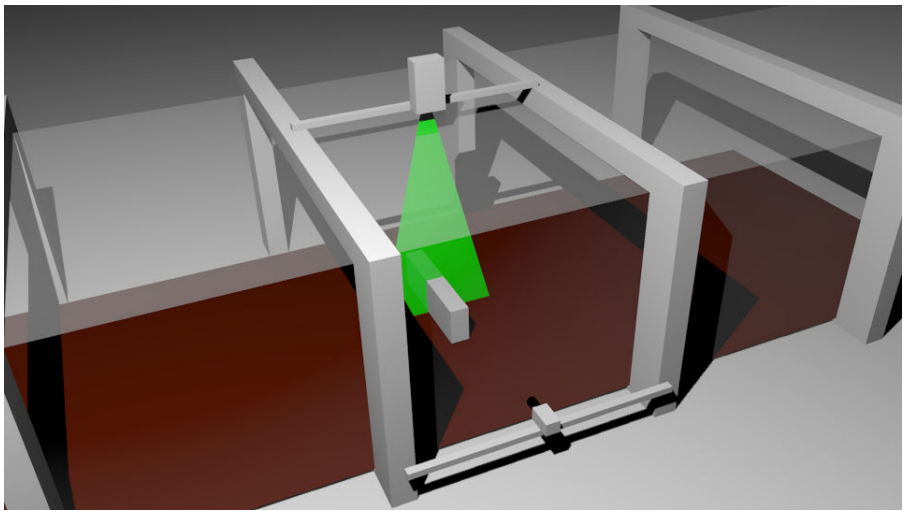

Figure 4.6: Wind tunnel test overview

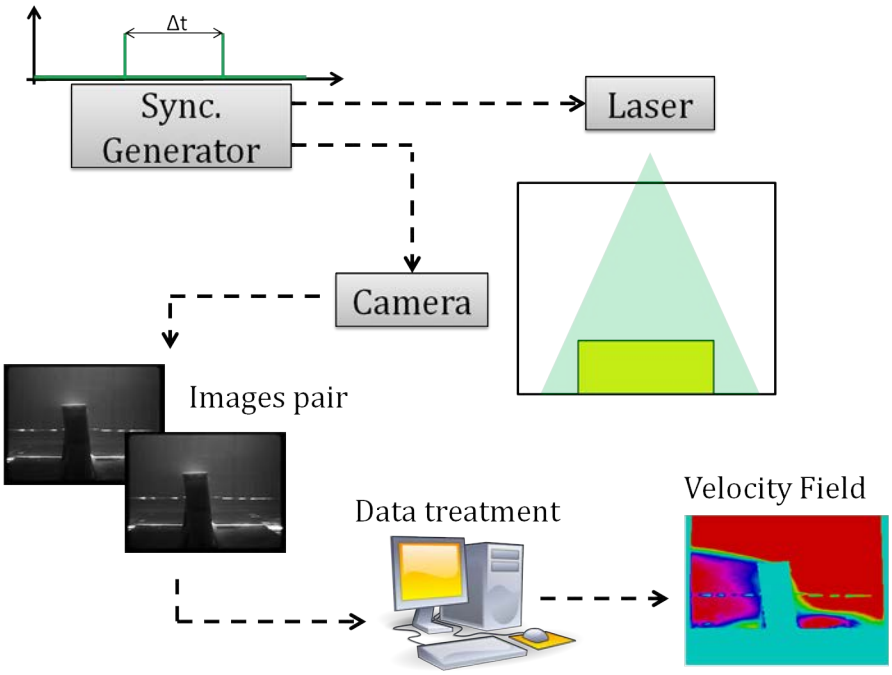

Figure 4.7: P.I.V scheme

The same picture from camera are used to follow the structural displacement. Three sights markers have been imposed on the side of the structure whereby the displacement has been measured. The pictures on the initial and final positions are superposed, thereafter by transparency of the top picture a quantitative and qualitative comparison can be done (see figure 4.8).

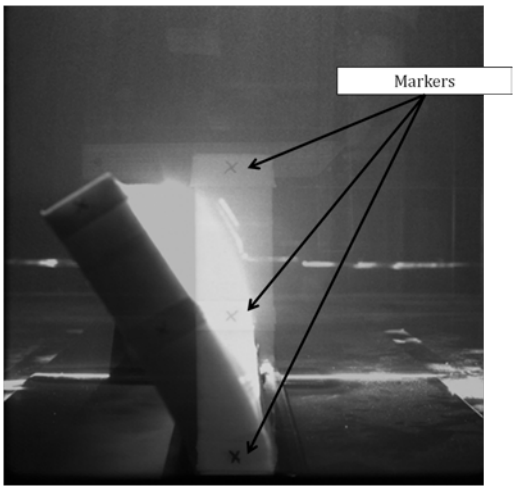

Figure 4.8: Structural displacement measurement

4.3.2 Plate fabrication

The choice of the plate's material is one of the key point, because the test has to deal with soft material in order to investigate significant displacements of a thick structure so as to be as close as possible of a situation which could be found in biomechanic.
In order to determine the optimal material regarding the structure thickness and compliance, a preliminary study has been undertaken using the analytical estimation of the drag forces F_d sustained by the plate.

$$F_d = \frac{1}{2}\rho C_d S U^2 \tag{4.13}$$

with C_d the drag coefficient, S the surface of the plate, U the prescribed velocity at infinity and ρ the fluid density.
The material which was suitable in our case is the poly soft Polyurethane foam 'HR7540'. This material is commonly used in furnitures, film productions, theatre props or automotive. It is composed of two parts a polyol and an isocyanate. Regarding the mixed quantity of each part the final foam can be ranged from high density and stiff to low density and soft material. The freedom and the easiness to change the foam stiffness is very useful in this work, accordingly, a couple of tests with different mixture ratio have been carried-out to reach the most optimal combination.

	Polyol	Isocyanate
Viscosity	750 mPa.s	375 mPa.s
Density	1200 g/l	1220 g/l
Color	Translucent	Amber

Table 4.1: Polyol and isocyanate characteristics

Because the primary product is two liquid, a special fabrication process has been developed to make the plate. The fabrication process is based on the method of moulding used to perform draped composite components. The figure 4.9 shown a detailed view of the process. Firstly a mould is made in wood where the inside dimensions correspond to the specimen dimension i.e. 1m length, 20cm heigh, 5cm thick (see figure 4.9a). Then a mixture of polyol and iscosyanate in a respectively 60%/40% in mass proportion is poured in the mould (see figure 4.9b). The mould is closed and the blend inflates until the mould is full (see figure 4.9c and 4.9d). The

ratio between the blend quantity and the mould volume influence the final structure as the mixing quantities, the total blend quantity is 1.2Kg.

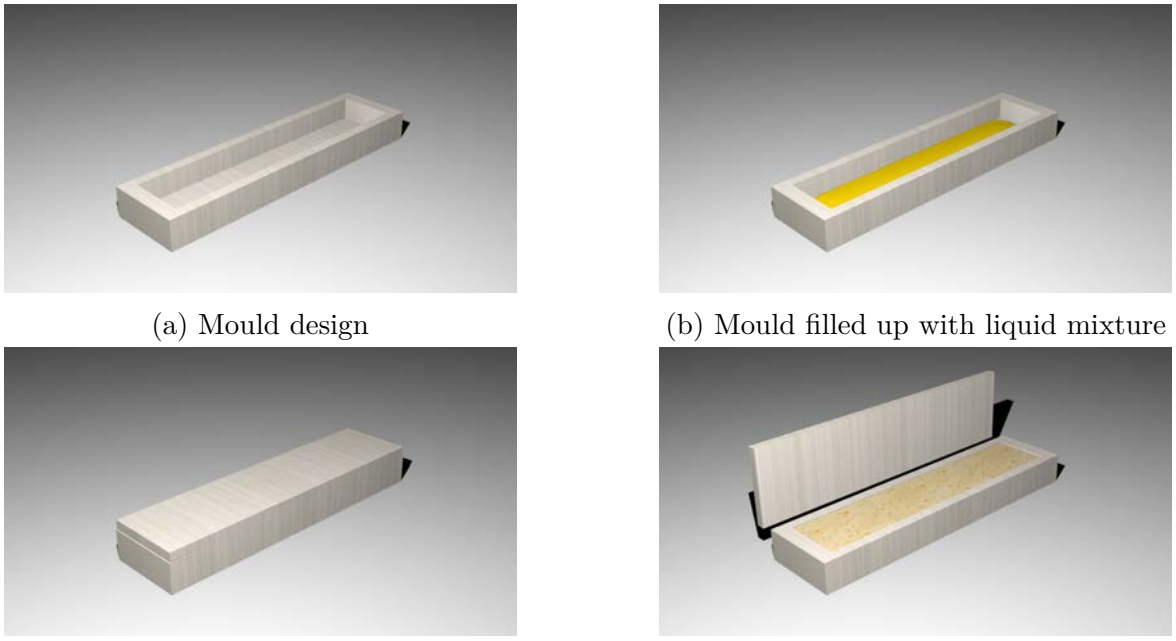

(a) Mould design

(b) Mould filled up with liquid mixture

(c) Mould close for solidification

(d) Demolding the solid foam plate

Figure 4.9: Fabrication process of the foam plate

4.3.3 Experimental results

Fluid results

The PIV measurements purposed a full understanding of the flow topologies and an extraction of velocity curves. The presence of flow topologies similar to vortex, boundary layer separation, turbulence, etc, impose the use of specific CFD simulation techniques. The velocity curves are used to compare and asses the simulation results.

The inlet velocity was $5m/s$, in the testing channel the Reynolds number was $Re = 6 \cdot 10^5$. Because in such a channel the Reynold number limit was $5 \cdot 10^4$, the flow is therefore classified as turbulent.

The velocity field located on the laser plane (see Figure 4.6) is given in figure 4.10 where the fluid moves from the right to the left. The PIV method allows measuring a temporal evolution of the flow, an instantaneous state is represented in figure 4.10a. Nevertheless the study is completed when the steady states is reached, therefore the rest of the work deals with the average velocity. The velocity field is averaged over a period of $2min$ to be sure that the flow is

stabilized, the results are presented in the figure 4.10b. A stable vortex zone in the upstream zone (at the right of the plate) on the corner between the plate and the bottom is depicted. A boundary layer separation can be observed on the top of the plate, the point of separation is around the middle of the plate. Due to the boundary layer separation a vortex shedding appears (see Figure 4.10a). Finally this vortex shedding lead to a large vortex located in the downstream area just behind the plate.

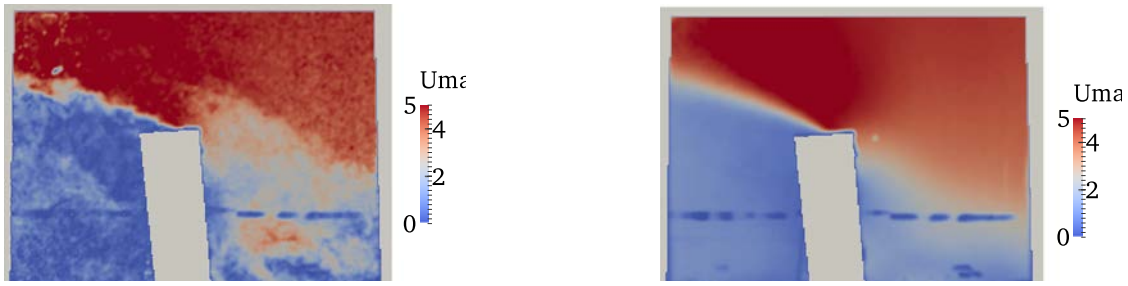

(a) Instantaneous (b) Averaged

Figure 4.10: Experimental velocity observed using P.I.V.

In the figure 4.10 an unattended coloured line is observed and should not be taking into account as it is just a light reflection as it is demonstrated in the figure 4.11. In addition, the irregularities are observed on the curve and are then retrieved.

(a) On the experimental results (b) On the post-treated results

Figure 4.11: Reflection localisation

With the software Paraview the curves showing the velocity evolution regarding the vertical coordinates are plotted and shown in figures 4.12.

In upstream, a zone where the velocity was closed to zero was observed near the bottom wall, it is the boundary layer. Near the structure a vortex is observed with velocity around $2.5m/s$ then the velocity evolve almost linearly until a laminar state which is reached at $40cm$ high when the velocity stayed constant at the inlet velocity, $5m/s$.

In downstream, the boundary layer is no more clear, a small vortex is observed near the bottom

wall with velocities around $0.5m/s$. Before to reach the laminar state, the velocity is almost constant because of the large vortex behind the structure. Contrary to the upstream flow, the laminar state is not observed at the same hight because of the boundary layer separation, farther the sampling position is, higher the free stream state is reached.

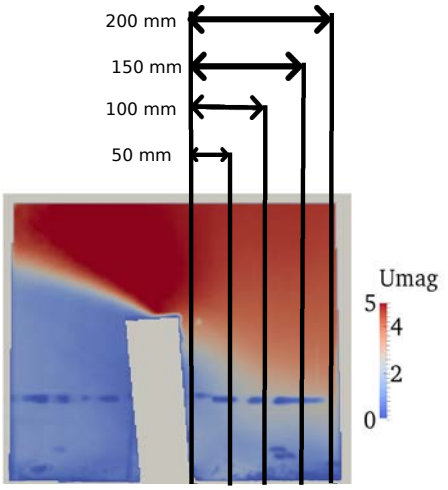

(a) Sampling localisation in upstream

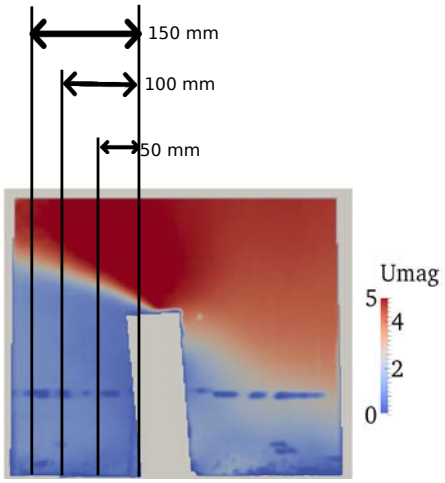

(b) Sampling localisation in downstream

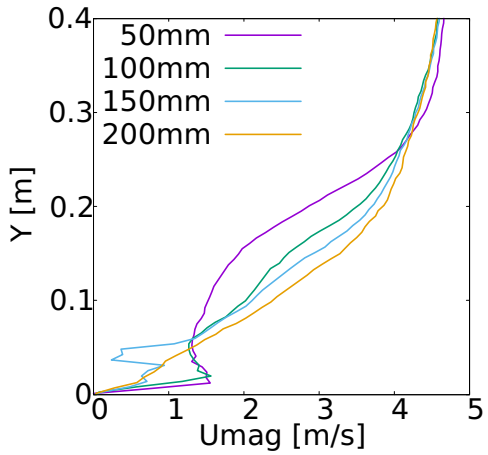

(c) Experimental velocity in upstream

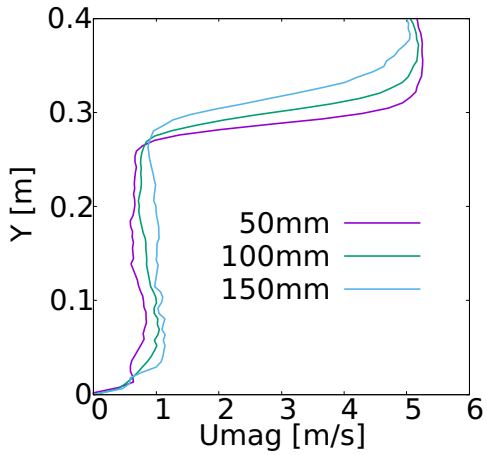

(d) Experimental velocity in downstream

Figure 4.12: P.I.V. velocity

Structure results

The plate is deformed and small vibrations are observed. The plate behaviour can thus be decomposed in two components a average displacement and oscillations around the mean position. Regarding the mean displacement, the oscillations are very small. Any of the intantaneous displacementcan be take as the average displacement without committed important error. The norm of the displacement of the plate top is $11.4mm$.

In this section, the velocity field and the structure displacement has been presented. The flow topology has showed a turbulent behaviour with a boundary layer separation involving vortex shedding. In addition one vortex in upstream and a large recirculation zone in downstream have been observed. The structure has been deformed and has been presented small but high frequency oscillations, thus the mean value has been taken as bending result.
The wind channel experiment claims to validate any fluid-structure coupling codes and especially the coupling solver implemented in this effort. The next section aims to asses the developed coupling solver efficiency against the wind channel test.

4.4 Numerical modelling of the wind channel experience

In order to asses the coupling solver efficiency, the fluid flow as well as the structure have to be separately modelled. Once the users are able to model the two domains some insights have to be given in the input files to identified the wet-boundary and the coupling computation can be launched.
Nonetheless, the foam material used in the wind channel experiment has been obtained by mixing two components where the expansion is restrained in a prescribed volume. A characterization of the same foam made with the same fabrication process parameters is of course not found in the literature. A dedicated characterization procedure is therefore required.
In this section, firstly the soft polyurethane foam is characterized based on three points bending. Subsequently, the modelling of the fluid, the solid and the coupling between the two domains are detailed. Finally, the numerical predictions are compared against the experimental results.

4.4.1 Material

Regarding the literature and the objective of the study, a three point bending test has been chosen. In spite of the three points bending test is a simple test, it appears to be the most relevant as the loading case sustains by the plate in the wind channel test is closed to the bending test.

Method The quasi-static three points bending experiment has been set-up on an Instron E3000 mechanical testing machine. The machine is instrumented by a $1KN$ load cell, the displacements are recorded following the Instron's recommendations at a sample rate of 10

records per second.

The experiment set-up is represented on the figure 4.13a. It is composed of the testing specimen, two cylindrical supports and a cylindrical impactor, all the dimensions are reported in figures 4.13b and 4.13c. The foam have been made in the same conditions as the foam of the wind channel. The two supports are blocked while the impactor displacement is managed by the machine. A quasi-static linear stroke of $25mm$ with a constant velocity of $50mm/min$ is prescribed to the impactor. The reaction forces were recorded by the machine. The experiment is repeated two times to guarantee the repeatability of the tests.

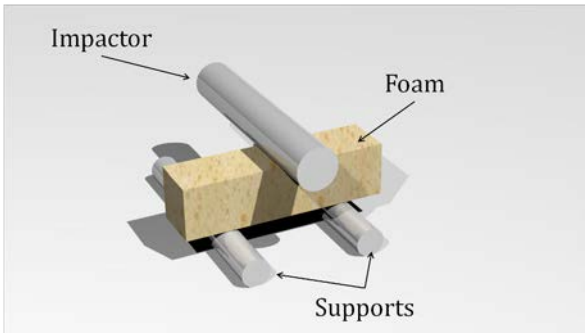

(a) Overview

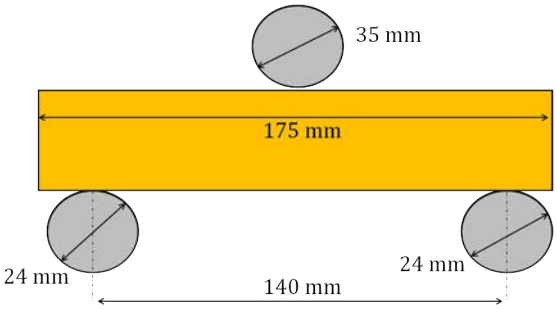

(b) Experimental devices dimensions

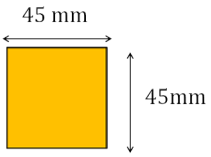

(c) Testing Specimen dimension

Figure 4.13: Three points bending experiment

Figure 4.14 shows the reaction forces on the impactor versus its stroke. It can be noticed that the experiment has been conducted two times and that a good repeatability has been observed. Despite of the large deformations are enforced on the foam specimen, the reaction forces remain low. One can conclude that the experiment may present some geometrical and provably material nonlinearities.

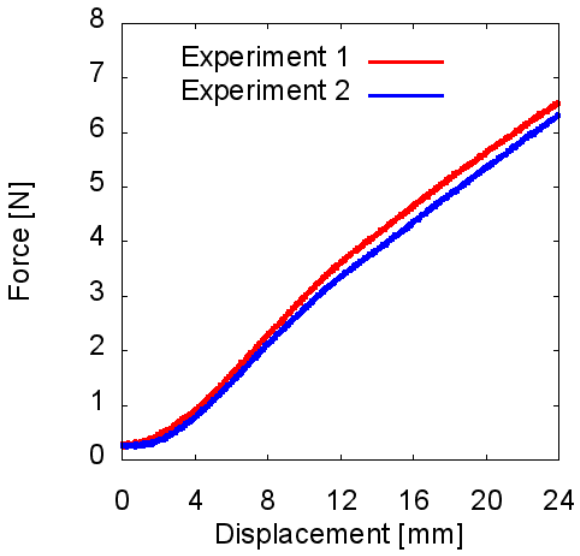

Figure 4.14: Three points bending: experimental reaction force vs stroke

A numerical model are performed on the commercial software LS-Dyna and is shown in figure 4.15. The foam specimen is modelled with 31200 hexahedral elements. The supports and the impactor are considered as rigid bodies with one range of hexahedral element. The contact between the foam and the other part is penalty based. The impactor is loaded with the same velocity as in the experiment. A central difference method is used for the time integration.
The same inverse analysis method which has been used for the gel identification is re-used. In order to identify the parameters of the hyperelastic model, the software LS-OPT is used based on a least square approximation method. The method allows determining for the best set of parameters by minimizing the square of the error between the experimental and numerical curves.

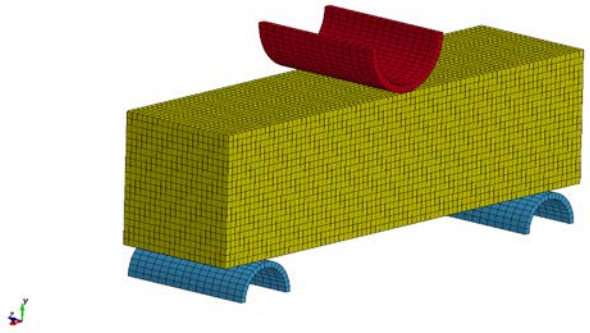

Figure 4.15: Three points bending: finite-element model

Results The results are showed in figures 4.16. Because of the large deformations a hyperelastic Neo-Hookean model is used. The numerical result are in good agreement with the

experimental behaviour with the Neo-Hookean parameter $C1 = 9.7 \cdot 10^{-3} MPa$.

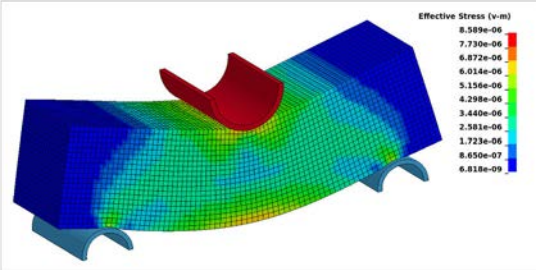

(a) Quantitative: Von-Mises strees

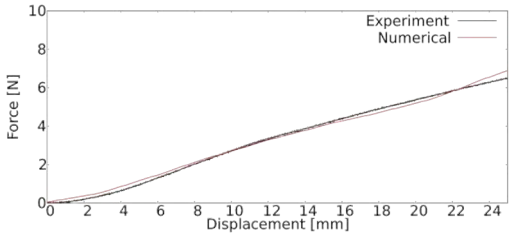

(b) Qualitative: load-displacement

Figure 4.16: Three points bending numerical results

In order to sum-up the present the material characterization section, the material used in the wind channel test is especially elaborating for this application. Indeed, the material model parameters can not be found in the literature. An experimental device has been therefore carried-out to get the experimental behaviour of the used polyurethane foam. Subsequently, a numerical model has been created and based on a least-square method an inverse analysis has allowed to identify the material parameter of a Neo-Hookean model.
At this stage, all the necessary data are available to carry out the fluid-structure coupling simulation of the wind channel with the developed code involving a partitioned scheme between LS-Dyna and OpenFOAM.

4.4.2 Method

In this section the fluid and solid models used in the coupling simulation are presented in terms of modelling assumptions, mesh, and boundary conditions prescription. Subsequently, some insights about the coupling strategy are given.

Fluid model

Geometry Regarding the wind channel benchmark geometry the situation can be assumed to be modelled in two dimensions and is represented in figure 4.17. In order to model a 2D phenomenon, special condition are provided by OpenFOAM. The flow channel is modelled with only one element through the third direction, with a very fine depth regarding the other dimension. The height of the channel is the same than the wind tunnel, i.e. $2m$. The length has to be sufficiently important to allow the stabilization of the boundary layer thickness before the obstacle, therefore it was found to be $2m$ and the depth is $1cm$.

Mesh In computational fluid dynamics the mesh size depicts a great influence on the result mainly if the flow model requires a turbulence model as it is shown in [Ariff et al., 2009]. In such a case a the size of the cells near the walls has to be determine by means of the $Y+$ parameter. The $Y+$ value is a non-dimensional parameter used to find the minimal element size to obtain accurate results near the walls of the computing domain. Its values depend on the Reynold number and the turbulence parameter. In the present case the $Y+$ value is taken equal to 30 following the prescribsions of [Ariff et al., 2009]. Based on the Wall distance Estimation of the website *cfd-online* the first cells near the walls has to measure $4mm$. Thus the whole model was composed of 150800 cells (see Figure 4.17).

Boundary conditions The boundary conditions are representative of the wind tunnel physics. At the bottom and top of the domain, non-slip conditions are enforced, at the inlet a constant and linear velocity of $5m/s$ is prescribed and at the outlet a zero pressure gradient lead the out free.

Because of the high Reynolds number a turbulence model has to be used. A K/ϵ model belonging to the Reynolds Average Navier-Stockes (RANS) field has been chosen. Following the instructions of [Ferziger and Peric, 2012], the initial values of the turbulent kinetic energy k and the turbulent dissipation ϵ are fixed to, $0.034m^2/s^2$ and $0.00705m^2/s^3$ respectively.

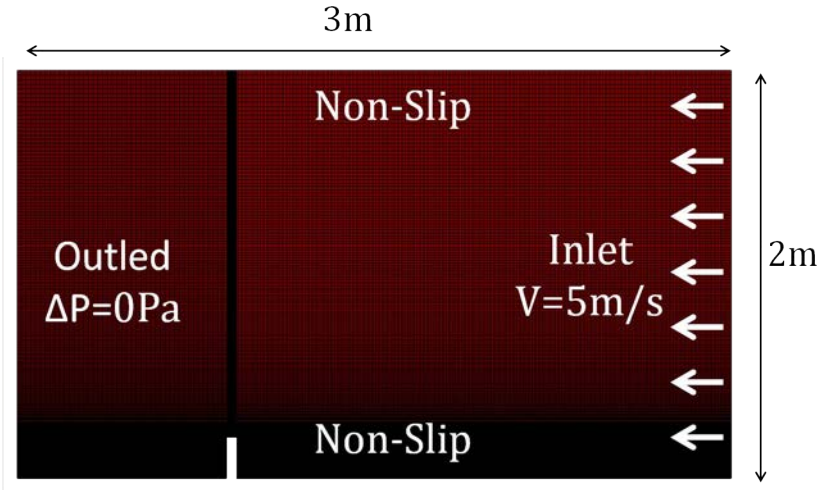

Figure 4.17: Fluid Model

Structure model

Geometry The plate model has to be accommodated to the fluid model so that the boundary fitting and conformed meshes assumptions are respected. Thus the plat depicts the same heigh

of $20cm$ and thickness of $5cm$ as the experiment. Because of the required depth of the fluid model to be in two dimension, the solid model is $1cm$ depth as well (see figure 4.18).

Mesh Regarding the structure's dimensions, 3D solid hexahedre elements are the most relevant. Because such element do not get rotational degree of freedom, a fine discretization is needed to model the plate's bending, 10 elements through the thickness are thus used.
In addition to that the information transfer between the fluid and solid mesh was performed on conforming meshes, i.e. the solid mesh had to fit exactly the fluid mesh. The mesh size are therefore $4mm/4mm/1cm$.

Boundary conditions The experiment is designed in such a way that the boundary conditions are simple. The plate is thus only blocked on the bottom by locked the six degrees of freedom of the nodes. The rest of the model is constraint to be enable to move in the plane of the fluid domain.

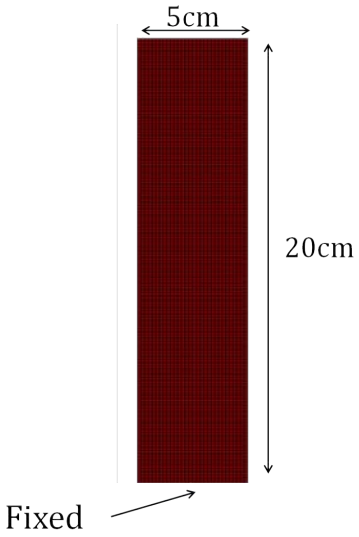

Figure 4.18: Solid Model

Coupling strategy

The interactions between the fluid and the structure are modelled by the strong coupling scheme presented in section 4.2.2. 3000 iterations are required for the fluid computation to reach a steady state, with a time step of $1s$ the computation duration is thus $3000s$. Regarding the plate deformation, the solid computation has to take into account the nonlinearities, the implicit scheme needs 10 steps to deliver accurate results, the solid computational duration is then fixed

to $1s$ with a time step of $0.1s$.
The data exchanges are completed in the fixed points of the coupling scheme. In this situation only one points are required because the dynamical effects modelling are currently not in the scope of this work. After a sensitivity study, the author showed that 7 fixed point iterations lead to stable results.

4.4.3 Results and Discussions

The comparison of the experimental results and the numerical predictions are presented regarding firstly the fluid velocities and then the solid displacement. The comparisons have to point-out the strengths and the weaknesses of the coupling code.

Fluid results

The comparisons of the fluid velocity fields are completed by a qualitative as well as a quantitative results.
The qualitative results allows to compared the global flow topologies, it is presented in figures 4.19. The boundary layer separation is well predicted as well as the large recirculation zone behind the plate. Unfortunately, in up-stream at the bottom of the plate a important vortex is observed in the experience but not in the simulation.
Once the flow topology is understood, the quantitative results 4.20 lead to a finer analysis. Despite the global prediction are in the same range that the experiments, a couple of points are mismatched.
In up-stream, two linked problems are pointed-out, the boundary layer and the upper velocity. Regarding the boundary layer, from the furthest to the closest of the plate the boundary layer is not accurately predicted. In the experiment a clear boundary layer is well established whereas it is not in the simulation. Accordingly, the predictions of the vortex and the upper velocity are not in good agreement because of the not established boundary layer.
In down-stream the numerical predictions fit better the experiment and thus confirm the previous conclusions. Indeed, the overall behaviours are in accordance, additionally the small vortex in the corner at the bottom of the plate despite it is very small, it is modelled. The great recirculation zone fit the experiment as well. Only one problem remains, the upper velocity are still not in agreement with the experiment. This problem is explain by a modelling problem of the boundary layer separation which depicts a higher angle with the horizontal that the

experiment.

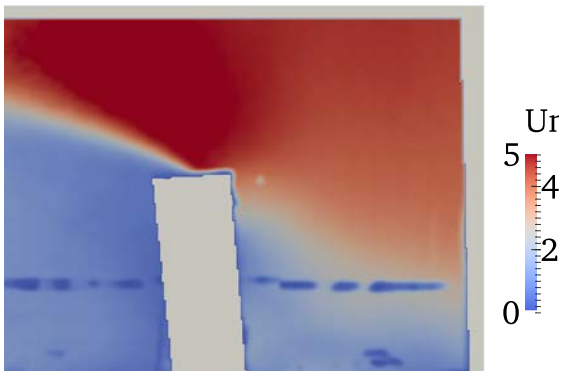

(a) Experiment

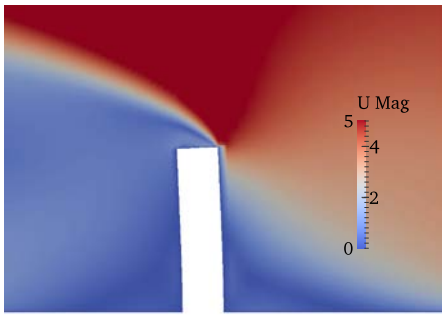

(b) Simulation: Velocity field

(c) Simulation: stream lines

Figure 4.19: Qualitative comparisons of flow topologies

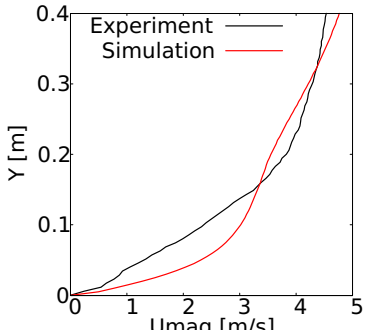

(a) Up-stream velocities, sampling: 200mm

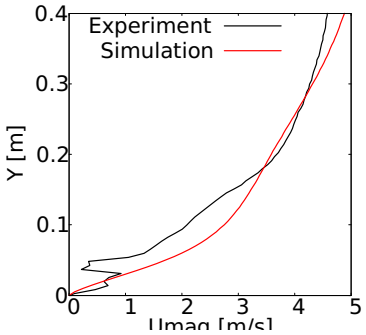

(b) Up-stream velocities, sampling: 150mm

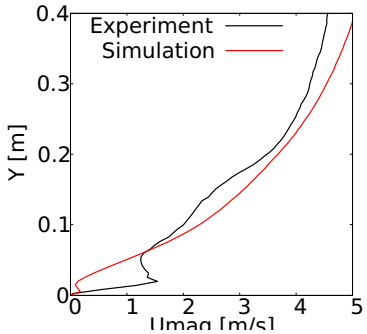

(c) Up-stream velocities, sampling: 100mm

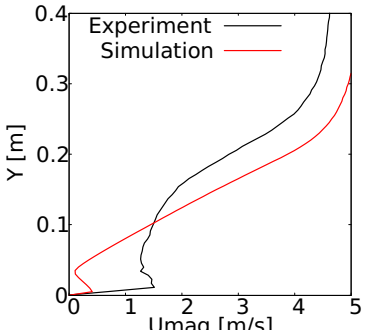

(d) Up-stream velocities, sampling: 50mm

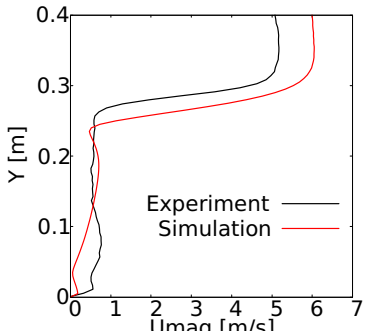

(e) Down-stream velocities, sampling: 50mm

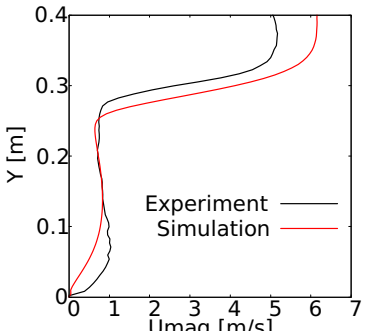

(f) Down-stream velocities, sampling: 100mm

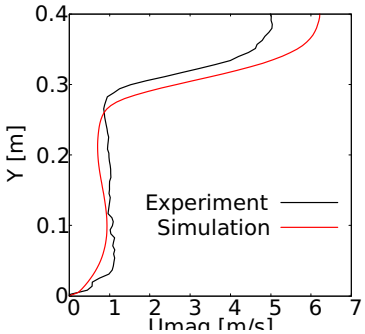

(g) Down-stream velocities, sampling: 150mm

Figure 4.20: Quantitative comparisons

Solid results

The comparison of the solid responses is straightforward, the qualitative comparison is shown in figures 4.21. It can be observed that the that the overall shapes are quit similar.

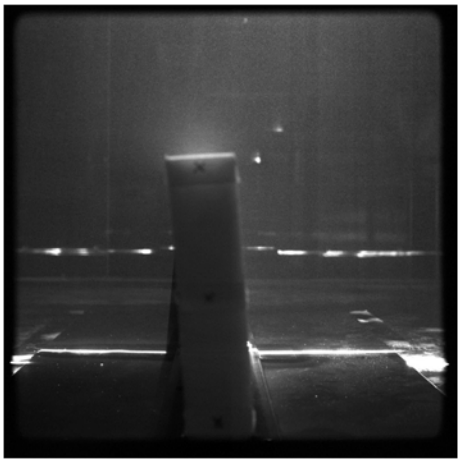

(a) Experiment

(b) Simulation

Figure 4.21: Comparison of solid bending

The bending values are compared in the table 4.2. It is observed that the coupling code provides a bending close to the experiment.

Fluid velocity	L(cm)		X(cm)		Y(cm)	
	Exp.	Num.	Exp.	Num.	Exp.	Num.
$5m/s$	1.14	1.28	1.13	1.27	0.16	0.17

Table 4.2: Solid bending comparison

Discussions

The previous comparisons provide various critical remarks about the first developments of the coupling code.

Dealing with the wind channel test, the coupling solver is stable and the convergence criterion is enable to stop the simulation. Although the mesh up-date procedure is not a simple task, the RBF implemented procedure depicts a sufficient level of accuracy and is readily managed by the users. The fluidic and structural results have lead to conclude to a good overall agreement. Indeed, the general behaviour of the fluid velocity is well predicted. The pressures over the whole structure surface should be thus in the range of the experiment but can not be validated. Accordingly, the structure bending is quiet close to the expectations.

Nevertheless, several drawbacks have been observed. The main drawback is about the velocity

mismatched between the experiment and the modelling. It has been demonstrated that it comes from a lack of accuracy in the modelling of the boundary layer unless the the used of turbulence model and wall functions.
To conclude this discussion, before to be enable to provide all the remarks about the developed coupling solver, the fluid modelling has to be deeply investigated.

4.5 Conclusion

The objective of this chapter has been to develop a solver enable to realise fluid-structure interactions coupling modelling, a coupling solver has been therefore developed in C++ language. The coupling solver links the structural code LS-Dyna and the fluidic solver OpenFOAM. Based on the literature survey a partitioned iterative coupling scheme has been chosen to be implemented. The partitioned iterative scheme depicts the advantage to maximise the tracking interface accuracy and the coupling's convergence.
Once the coupling solver has been implemented, it must be validated against experimental results. Based on the literature survey, it has been shown that few experimental tests are available or are not well adapted for the validation of codes. It has made the decision to create a new experimental test especially devoted to the code validation. The test has been carried-out in a wind channel and imposed the bending of a plate under the effects of an constant air flow. The velocity field measured by a PIV device and the plate bending measured by camera are used to perform the validations.
The comparisons of the numerical predictions against experimental results have led to conclude to a good overall agreement. But it has been observed that the velocity mismatched between the experiment and the modelling because of a non adapted boundary layer modelling. A solution to overcome the problem is to impose in the inlet on the modelling domain the velocity retrieved near the plate when the boundary layer is already fully established. An other appealing parameter for the validation is the pressure applied on the structure by the flow. The pressure measurements had been carried-out in the wind channel test by means of dynamical kulite sensors. Unfortunately, the pressure measurements is a very sensible operation and correct pressure signal has still not been obtained.
To conclude the first version of the developed code provides promising results, now it requires additional improvements and enhancements so as to be more versatile and powerful. The exper-

imental test for the validation of any fluid-structure interactions solver has shown its usefulness. Now it requires to perform new pressure measurements to be enable to provide a full package of results for the scientific community interesting about the coupling solver development.

5 Conclusion

The purpose of this work was to improve the biofidelity of the human body models. In this work, it has been highlighted that the traumatic brain injury remains a social burden. One of the challenges is to get a better understanding of the brain injury mechanisms. In order to overcome this issue numerical models appear to be an interesting manner. This study aims to improve the human head model biofidelity by enhancing its behaviour with the include of fluid structure interactions. Nevertheless, the modelling of interactions between viscous corporal fluids and soft matter as the brain remains a challenge. Therefore, a particular interest has been given to the fluid-structure interactions between a soft structure and a viscous fluid.

The first chapter intends to review the modelling techniques available in the literature to treat the fluid-structure interactions issues. It has been shown that the main difficulties arise from the important behaviour differences between the fluid and the solid media. Once the governing equations of the fluid and the solid have been detailed, the transfer of the velocity and stresses trough the wet-boundary surface was is investigated. This transfer showed a great importance and was monitored by coupling equations which have been presented. Indeed, if the coupling equations are not respected by the numerical schemes, the energy balance could not be equilibrated and as consequence instabilities appeared. Therefore, the coupling scheme has to be well adapted to each specific phenomenon. The two main families of coupling schemes are the monolithic and the partitioned scheme. The monolithic solved all the equations in an unique framework where the coupling equations are implicitly involved, while the partitioned scheme used a fluid and a solid solver as black boxes and allows the data transfer to realize the coupling problem. Despite, the monolithic scheme is appealing regarding its robustness and performance, it required very high computational implementation skills, it is not flexible

and difficult to update. It has therefore not been used in this investigation and the partitioned scheme was preferred. Dealing with partitioned scheme two points have to be well undertaken to assure the coupling equations respect: the spatial coupling and the temporal coupling.
The spatial coupling assures the coupling through the wet-boundary. The discretizations of the fluid and solid are thus to be adapted. If the fluid and structure grids respect their own physical boundaries, a clear wet-boundary appear and the situation is called Boundary-fitting. Otherwise if the fluid grid is Cartesian and the solid grid is superposed on it, the situation is called Non-Boundary fitting and the wet-boundary interface tracking becomes a real challenge.
The temporal coupling manages the frequency of data exchange between the fluid and solid solvers. If the data is exchanged only once per time step, the coupling is considered as explicit. Nevertheless in order to respect the coupling equations or in order to overcome the added mass effects, a loop structure has to be used and the data transfer must be done several time per time step until a convergence criteria is reached.
Finally in this first chapter a review of the fluid structure interaction applications and validation tests have been performed. It has been observed that several coupling codes are being validated against numerical tests but unfortunately very few experimental validation tests are available.
Regarding this first chapter, because the fluid assessment requires a good accuracy mainly near the wet-boundary a boundary fitting method was used and because the involving flow is viscous (corporal fluid), the load case is dynamic (impact) and the material is soft (brain), an implicit temporal coupling is required.

The second chapter aims to demonstrate the key role of the fluid-structure interactions in the brain injury onset by means of an experimental device. The experiment has been a physical model of a human head involving a brain substitute embedded in a rigid vessel sustained a dynamical load case. Between the gel and the vessel a water layer might be inserted leading to two versions, one without water and an other including water interface. Indeed, the experiments have been used at two stages: the version without water has been used to characterize a soft silicon gel Sylgard 527 gel largely used as brain substitute in the literature. The version including water interface has claimed to carried-out the first simulations of the experimental test to assess the ability to model the fluid-structure interactions with a commercial partitioned coupling solver LS-Dyna ICFD.

The comparison of the experimental results of the version with and without water has highlighted that the cerebrospinal fluid has a great influence on the brain behaviour. Based on indentation and relaxation experiments the gel has been characterized thanks to three hyperelastic models. The new models have been validated using the version without the water interface of the dynamical experiment. Although, the previous characterized gel models have been used for the model including water interface, it was not possible to achieve convergence. Because of the dynamical load cases which cannot be treated using the implicit time integration fluid solver and the close fluid and solid densities leading to instabilities. Accordingly, it has been decided to develop an in-house coupling code.

The purpose of the third chapter is the development of a coupling code where the ultimate goal has been to model the previous dynamical physical head model including water interface. Based on the literature review conclusions a partitioned coupling scheme between the two well known fluid and solid solvers respectively OpenFOAM and LS-Dyna is the most suitable choice. It consisted in a middleware written in C++ which accomplish the data transfer between the two black boxes. In order to respect as much as possible the coupling equations an implicit coupling algorithm has been developed monitored by convergence criteria based on the internal energy. The accommodation of the fluid grid on the deformed structure mesh was performed by means of a Radius Based Function function.

This baseline implementation had to be validated against experiments prior undertaking any further developments. Nonetheless based on the literature review, no experimental test were really available, thus it has been decided to carry-out an experimental test especially designed for the fluid-structure algorithm validation. This validation consisted in a simple plate made of a soft polyurethane foam which is bent by means of an steady-state air flow of $5m/s$ in a wind channel. The fluid velocity fields have been measured by means of a Particle Image Velocimetry device. The structure deflection has been tracked by high speed camera.

The objective has been to model this experiment. As, the soft polyurethane foam has been made in the laboratory, there was no material data available to describe its behaviour. A three-point bending test has been thus carried-out to characterize the material using three hyperelastic models.

The previously implemented coupling code was based on the steady-state turbulent flow algorithm SIMPLE from OpenFOAM and the nonlinear implicit solid solver LS-Dyna. The

coupling code has shown a good overall agreement for the fluid velocities and the plate deflection assessment but was not able to assess very accurately the boundary layer.

To sum-up the completed works, it has been demonstrated than the fluid plays a key role in the human head behaviour. A substitute of the brain has been fairly characterized and subsequently used to assess the modelling ability of a commercial code to model a fluid-structure phenomenon involving viscous fluid and very soft material. Unfortunately, as the commercial solver was not able to perform the fluid-structure modelling due to high accelerations, it has been decided to develop an in-house code. The first step of this code has been successfully implemented and a validation experimental test has been carried out. The developed code could not be fully validated and has led to various perspectives to improve so the physical head model to be modelled successfully.

The presented investigation had led to several perspectives. The wind channel test has to be further investigated to be accurately model the velocity of $5m/s$. The wind channel test has been carried out for higher inlet velocity up to $12m/s$ leading to higher plate deflection. The modelling of the higher fluid velocity should assess the validity of the RBF mesh-update procedure for higher deformations. Currently, the coupling code is limited to conformed meshes, it is a very cumbersome limitation the real finite elements models are of complex geometries and the computational time may be unnecessary high. A procedure to enable the treatment of a non-conforming mesh should be developed based on the literature review.
Once the coupling code is validated for the cases where the fluid flows around the structure, the converse way has to be investigated, i.e. where the solid motion enforces the fluid motion as in the sloshing cases. At this stage the physical head model with water can be used to assess the accuracy of the in-house coupling code.
The wind channel test is a promising validation experiment. But it has to be improvedn using pressure sensors in order to measure accurately the pressure applied on the plate.
The global objective of this work was to improve the human body modelling. Therefore, the in-house coupling code will thus be used for biomechanical problems with more realistic and complex geometries and material properties. Some problems such as the head impact or the automotive crash with pregnant woman could be some situations which are in the scope of this work.

Bibliography

[Aghajari and Schäfer, 2015] Aghajari, N. and Schäfer, M. (2015). Efficient shape optimization for fluid–structure interaction problems. *Journal of Fluids and Structures*, 57:298–313.

[Aletti et al., 2016] Aletti, M., Gerbeau, J.-F., and Lombardi, D. (2016). A simplified fluid–structure model for arterial flow. application to retinal hemodynamics. *Computer Methods in Applied Mechanics and Engineering*, 306:77–94.

[Angot et al., 1999] Angot, P., Bruneau, C.-H., and Fabrie, P. (1999). A penalization method to take into account obstacles in incompressible viscous flows. *Numerische Mathematik*, 81(4):497–520.

[Appleby-Thomas et al., 2014] Appleby-Thomas, G., Hazell, P., Sheldon, R., Stennett, C., Hameed, A., and Wilgeroth, J. (2014). The high strain-rate behaviour of selected tissue analogues. *Journal of the mechanical behavior of biomedical materials*, 33:124–135.

[Aquelet et al., 2006] Aquelet, N., Souli, M., and Olovsson, L. (2006). Euler–lagrange coupling with damping effects: Application to slamming problems. *Computer methods in applied mechanics and engineering*, 195(1):110–132.

[Ariff et al., 2009] Ariff, M., Salim, S. M., and Cheah, S. C. (2009). Wall y+ approach for dealing with turbulent flow over a surface mounted cube: part 1—low reynolds number. In *Proceedings of the 7th International Conference on CFD in the Minerals and Process Industries, Melbourne, Australia*, pages 9–11.

[Asgharpour et al., 2014] Asgharpour, Z., Baumgartner, D., Willinger, R., Graw, M., and Peldschus, S. (2014). The validation and application of a finite element human head model for frontal skull fracture analysis. *Journal of the mechanical behavior of biomedical materials*, 33:16–23.

[Auperrin, 2009] Auperrin, A. (2009). *Caractérisation tissulaire pour la détermination du comportement de l'os crânien: essais mécaniques et imagerie médicale.* PhD thesis, Université de Valenciennes et du Hainaut-Cambresis.

[Azar et al., 2000] Azar, F. S., Metaxas, D. N., Miller, R. T., and Schnall, M. D. (2000). Methods for predicting mechanical deformations in the breast during clinical breast biopsy. *Center for Human Modeling and Simulation*, page 102.

[Baaijens, 2001] Baaijens, F. P. (2001). A fictitious domain/mortar element method for fluid-structure interaction. *International Journal for Numerical Methods in Fluids*, 35(7):743–761.

[Babu and Reddy, 1980] Babu, P. T. and Reddy, D. (1980). Fluid-structure interaction response analysis of floating nuclear plants including the effects of mooring. *Ocean Engineering*, 7(6):707–741.

[Baker, 1992] Baker, S. P. (1992). *The injury fact book*. Oxford University Press, USA.

[Banks et al., 2014] Banks, J. W., Henshaw, W. D., and Schwendeman, D. W. (2014). An analysis of a new stable partitioned algorithm for fsi problems. part i: Incompressible flow and elastic solids. *Journal of Computational Physics*, 269:108–137.

[Bazilevs et al., 2013] Bazilevs, Y., Hsu, M.-C., and Bement, M. (2013). Adjoint-based control of fluid-structure interaction for computational steering applications. *Procedia Computer Science*, 18:1989–1998.

[Beckert and Wendland, 2001] Beckert, A. and Wendland, H. (2001). Multivariate interpolation for fluid-structure-interaction problems using radial basis functions. *Aerospace Science and Technology*, 5(2):125–134.

[Belytschko, 1980] Belytschko, T. (1980). Fluid-structure interaction. *Computers & Structures*, 12(4):459–469.

[Belytschko and Schumann, 1980] Belytschko, T. and Schumann, U. (1980). Fluid-structure interactions in light water reactor systems. *Nuclear Engineering and Design*, 60(2):173–195.

[Bradshaw et al., 2001] Bradshaw, D., Ivarsson, J., Morfey, C., and Viano, D. C. (2001). Simulation of acute subdural hematoma and diffuse axonal injury in coronal head impact. *Journal of Biomechanics*, 34(1):85–94.

[Brands et al., 2002] Brands, D. W., Bovendeerd, P. H., and Wismans, J. (2002). On the potential importance of non-linear viscoelastic material modelling for numerical prediction of brain tissue response: test and application. In *SAE CONFERENCE PROCEEDINGS P*, pages 103–122.

[Brennen, 1982] Brennen, C. (1982). A review of added mass and fluid inertial forces. Technical report, DTIC Document.

[Brennen, 2013] Brennen, C. E. (2013). *Cavitation and bubble dynamics*. Cambridge University Press.

[Bruneau and Saad, 2006] Bruneau, C.-H. and Saad, M. (2006). The 2d lid-driven cavity problem revisited. *Computers & Fluids*, 35(3):326–348.

[Bry, 2015] Bry, R. (2015). *Contribution à l'étude de la variabilité des propriétés mécaniques de l'os cortical diaphysaire d'un os porteur (fémur) et non-porteur (humérus)*. PhD thesis, Université de Valenciennes et du Hainaut-Cambresis.

[Casadei and Potapov, 2004] Casadei, F. and Potapov, S. (2004). Permanent fluid–structure interaction with non-conforming interfaces in fast transient dynamics. *Computer methods in applied mechanics and engineering*, 193(39):4157–4194.

[Causin et al., 2005] Causin, P., Gerbeau, J.-F., and Nobile, F. (2005). Added-mass effect in the design of partitioned algorithms for fluid–structure problems. *Computer methods in applied mechanics and engineering*, 194(42):4506–4527.

[Cernak, 2005] Cernak, I. (2005). Animal models of head trauma. *NeuroRx*, 2(3):410–422.

[Charmetant, 2011] Charmetant, A. (2011). *Approches hyperélastiques pour la modélisation du comportement mécanique de préformes tissées de composites*. PhD thesis, INSA de Lyon.

[Cobb et al., 2013] Cobb, B. R., Urban, J. E., Davenport, E. M., Rowson, S., Duma, S. M., Maldjian, J. A., Whitlow, C. T., Powers, A. K., and Stitzel, J. D. (2013). Head impact exposure in youth football: elementary school ages 9–12 years and the effect of practice structure. *Annals of biomedical engineering*, 41(12):2463–2473.

[Codina et al., 2009] Codina, R., Houzeaux, G., Coppola-Owen, H., and Baiges, J. (2009). The fixed-mesh ale approach for the numerical approximation of flows in moving domains. *Journal of Computational Physics*, 228(5):1591–1611.

[Czerner et al., 2015] Czerner, M., Fellay, L. S., Suárez, M. P., Frontini, P. M., and Fasce, L. A. (2015). Determination of elastic modulus of gelatin gels by indentation experiments. *Procedia Materials Science*, 8:287–296.

[De Boer et al., 2007] De Boer, A., Van Zuijlen, A., and Bijl, H. (2007). Review of coupling methods for non-matching meshes. *Computer methods in applied mechanics and engineering*, 196(8):1515–1525.

[De La Torre et al., 2013] De La Torre, O., Escaler, X., Egusquiza, E., and Farhat, M. (2013). Experimental investigation of added mass effects on a hydrofoil under cavitation conditions. *Journal of Fluids and Structures*, 39:173–187.

[Debongnie, 1986] Debongnie, J.-F. (1986). On a purely lagrangian formulation of sloshing and fluid-induced vibrations of tanks. *Computer methods in applied mechanics and engineering*, 58(1):1–18.

[Delille, 2002] Delille, C. (2002). *Contribution à l'identification de lois matérielles de l'os du crâne humain en quasi-statique à partir d'expérimentations et de simulations numériques.* PhD thesis, Valenciennes.

[Delille, 2007] Delille, R. (2007). *Contribution à la compréhension du comportement mécanique de l'os du crâne humain sous différents moyens de conservation et de sollicitation.* PhD thesis, Université de Valenciennes et du Hainaut-Cambresis.

[Demartini et al., 2004] Demartini, L. C., Vielmo, H. A., and Möller, S. (2004). Numeric and experimental analysis of the turbulent flow through a channel with baffle plates. *Journal of the Brazilian Society of Mechanical Sciences and Engineering*, 26(2):153–159.

[Demirdžić and Martinović, 1993] Demirdžić, I. and Martinović, D. (1993). Finite volume method for thermo-elasto-plastic stress analysis. *Computer methods in applied mechanics and engineering*, 109(3):331–349.

[Donea et al., 1982] Donea, J., Giuliani, S., and Halleux, J. (1982). An arbitrary lagrangian-eulerian finite element method for transient dynamic fluid-structure interactions. *Computer methods in applied mechanics and engineering*, 33(1):689–723.

[Donea et al., 2004] Donea, J., Huerta, A., Ponthot, J.-P., and Rodríguez-Ferran, A. (2004). *Arbitrary Lagrangian–Eulerian Methods.*

[Du Buat, 1786] Du Buat, P. (1786). Principes d'hydraulique, 2 vols, new edn.

[Duan et al., 2012] Duan, Z., An, Y., Zhang, J., and Jiang, H. (2012). The effect of large deformation and material nonlinearity on gel indentation. *Acta Mechanica Sinica*, 28(4):1058–1067.

[Durbin et al., 2001] Durbin, P., Majumdar, S., and Iaccarino, G. (2001). Rans solvers with adaptative structured boundary non conforming grids. *Annual Research Briefs*, pages 353–364.

[El Baroudi et al., 2012] El Baroudi, A., Razafimahery, F., and Rakotomanana-Ravelonarivo, L. (2012). Three-dimensional modal analysis of an idealized human head including fluid–structure interaction effects. *Acta Mechanica*, 223(9):1899–1915.

[Fackrell, 2011] Fackrell, S. (2011). Study of the added mass of cylinders and spheres.

[Fadlun et al., 2000] Fadlun, E., Verzicco, R., Orlandi, P., and Mohd-Yusof, J. (2000). Combined immersed-boundary finite-difference methods for three-dimensional complex flow simulations. *Journal of Computational Physics*, 161(1):35–60.

[Farhat et al., 2001] Farhat, C., Geuzaine, P., and Grandmont, C. (2001). The discrete geometric conservation law and the nonlinear stability of ale schemes for the solution of flow problems on moving grids. *Journal of Computational Physics*, 174(2):669–694.

[Farhat and Lesoinne, 2000] Farhat, C. and Lesoinne, M. (2000). Two efficient staggered algorithms for the serial and parallel solution of three-dimensional nonlinear transient aeroelastic problems. *Computer methods in applied mechanics and engineering*, 182(3):499–515.

[Farhat et al., 1998] Farhat, C., Lesoinne, M., and Le Tallec, P. (1998). Load and motion transfer algorithms for fluid/structure interaction problems with non-matching discrete interfaces: Momentum and energy conservation, optimal discretization and application to aeroelasticity. *Computer methods in applied mechanics and engineering*, 157(1):95–114.

[Farhat et al., 2006] Farhat, C., Van der Zee, K. G., and Geuzaine, P. (2006). Provably second-order time-accurate loosely-coupled solution algorithms for transient nonlinear computational aeroelasticity. *Computer methods in applied mechanics and engineering*, 195(17):1973–2001.

[Ferziger and Peric, 2012] Ferziger, J. H. and Peric, M. (2012). *Computational methods for fluid dynamics*. Springer Science & Business Media.

[Fontenier et al., 2016] Fontenier, B., Hault-Dubrulle, A., Drazetic, P., Fontaine, C., and Naceur, H. (2016). On the mechanical characterization and modeling of polymer gel brain substitute under dynamic rotational loading. *Journal of the Mechanical Behavior of Biomedical Materials*.

[Förster et al., 2006] Förster, C., Wall, W. A., and Ramm, E. (2006). The artificial added mass effect in sequential staggered fluid-structure interaction algorithms. In *ECCOMAS CFD 2006: Proceedings of the European Conference on Computational Fluid Dynamics, Egmond aan Zee, The Netherlands, September 5-8, 2006*. Delft University of Technology; European Community on Computational Methods in Applied Sciences (ECCOMAS).

[Förster et al., 2007] Förster, C., Wall, W. A., and Ramm, E. (2007). Artificial added mass instabilities in sequential staggered coupling of nonlinear structures and incompressible viscous flows. *Computer methods in applied mechanics and engineering*, 196(7):1278–1293.

[Ghia et al., 1982] Ghia, U., Ghia, K. N., and Shin, C. (1982). High-re solutions for incompressible flow using the navier-stokes equations and a multigrid method. *Journal of computational physics*, 48(3):387–411.

[Glowinski et al., 1999] Glowinski, R., Pan, T.-W., Hesla, T. I., and Joseph, D. D. (1999). A distributed lagrange multiplier/fictitious domain method for particulate flows. *International Journal of Multiphase Flow*, 25(5):755–794.

[Glowinski et al., 2141] Glowinski, R., Pan, T.-W., Hesla, T. I., Joseph, D. D., and Periaux, J. (2141). A distributed lagrange multiplier/fictitious domain method for the simulation of flow around moving rigid bodies: application to particulate flow. *Computer Methods in Applied Mechanics and Engineering*, 184(2):241–267.

[Gomes, 2011] Gomes, J. M. P. (2011). *Fluid-structure interaction-induced oscillation of flexible structures in uniform flows*. PhD thesis, Universitätsbibliothek der Universität Erlangen-Nürnberg.

[Greenshields and Weller, 2005] Greenshields, C. J. and Weller, H. G. (2005). A unified formulation for continuum mechanics applied to fluid structure interaction in flexible tubes. *International Journal for Numerical Methods in Engineering*, 64(12):1575–1593.

[Gu et al., 2012] Gu, L., Chafi, M. S., Ganpule, S., and Chandra, N. (2012). The influence of heterogeneous meninges on the brain mechanics under primary blast loading. *Composites Part B: Engineering*, 43(8):3160–3166.

[Halgrin, 2009] Halgrin, J. (2009). *Influence des paramètres architecturaux sur le comportement mécanique de l'os trabéculaire*. PhD thesis, Université de Valenciennes et du Hainaut-Cambresis.

[Hallquist et al., 2006] Hallquist, J. O. et al. (2006). Ls-dyna theory manual. *Livermore software Technology corporation*, 3:25–31.

[Hault-Dubrulle, 2007] Hault-Dubrulle, A. (2007). *Contribution à l'amélioration des connaissances des phénomènes d'interaction fluide/structure à l'intérieur de la boîte crânienne soumise à une sollicitation dynamique: études expérimentale et numérique*. PhD thesis, Valenciennes.

[Heil et al., 2008] Heil, M., Hazel, A. L., and Boyle, J. (2008). Solvers for large-displacement fluid–structure interaction problems: segregated versus monolithic approaches. *Computational Mechanics*, 43(1):91–101.

[Hirt et al., 1974] Hirt, C., Amsden, A. A., and Cook, J. (1974). An arbitrary lagrangian-eulerian computing method for all flow speeds. *Journal of Computational Physics*, 14(3):227–253.

[Hovnanian, 2012] Hovnanian, J. (2012). *Méthode de frontières immergées pour la mécanique des fluides. Application à la simulation de la nage.* PhD thesis, Université Sciences et Technologies-Bordeaux I.

[Huang et al., 2016] Huang, W., Jia, B., Zhang, W., Huang, X., Li, D., and Ren, P. (2016). Dynamic failure of clamped metallic circular plates subjected to underwater impulsive loads. *International Journal of Impact Engineering*, 94:96–108.

[Huang et al., 2013] Huang, X., Valero, C., Egusquiza, E., Presas, A., and Guardo, A. (2013). Numerical and experimental analysis of the dynamic response of large submerged trash-racks. *Computers & Fluids*, 71:54–64.

[Hubner et al., 2004] Hubner, B., Walhorn, E., and Dinkler, D. (2004). A monolithic approach to fluid structure interaction using space time finite elements. *Computer Methods in Applied Mechanics and Engineering*, 193:2087–2104.

[Hughes, 1980] Hughes, T. J. (1980). Recent developments in computer methods for structural analysis. *Nuclear Engineering and Design*, 57(2):427–439.

[Hughes et al., 1981] Hughes, T. J., Liu, W. K., and Zimmermann, T. K. (1981). Lagrangian-eulerian finite element formulation for incompressible viscous flows. *Computer methods in applied mechanics and engineering*, 29(3):329–349.

[Huihao et al., 2014] Huihao, W., Hongsheng, Z., Bo, C., Linghui, L., Guoqing, D., and Yinyu, S. (2014). Fluid-structure interaction analysis on blood flow and arterial wall of vertebral arteries during cervical (physiological) activities. *Journal of Orthopaedic Translation*, 4(2):223.

[Hussain et al., 2011] Hussain, M., Abid, M., Ahmad, M., Khokhar, A., and Masud, A. (2011). A parallel implementation of ale moving mesh technique for fsi problems using openmp. *International Journal of Parallel Programming*, 39(6):717–745.

[Iafrati et al., 2015] Iafrati, A., Grizzi, S., Siemann, M., and Montañés, L. B. (2015). High-speed ditching of a flat plate: Experimental data and uncertainty assessment. *Journal of Fluids and Structures*, 55:501–525.

[Iii et al., 1999] Iii, J. N., Newman, P., Iii, A. T., and Hou, G.-W. (1999). Efficient nonlinear static aeroelastic wing analysis. *Computers & fluids*, 28(4):615–628.

[Ivarsson et al., 2000] Ivarsson, J., Viano, D. C., Lövsund, P., and Aldman, B. (2000). Strain relief from the cerebral ventricles during head impact: experimental studies on natural protection of the brain. *Journal of Biomechanics*, 33(2):181–189.

[Iwamoto et al., 2007] Iwamoto, M., Nakahira, Y., Tamura, A., Kimpara, H., Watanabe, I., and Miki, K. (2007). Development of advanced human models in thums. In *Proc. 6th European LS-DYNA Users' Conference*, pages 47–56.

[Jaiman et al., 2016] Jaiman, R., Pillalamarri, N., and Guan, M. (2016). A stable second-order partitioned iterative scheme for freely vibrating low-mass bluff bodies in a uniform flow. *Computer Methods in Applied Mechanics and Engineering*, 301:187–215.

[Ji et al., 2014] Ji, S., Ghadyani, H., Bolander, R. P., Beckwith, J. G., Ford, J. C., McAllister, T. W., Flashman, L. A., Paulsen, K. D., Ernstrom, K., Jain, S., et al. (2014). Parametric comparisons of intracranial mechanical responses from three validated finite element models of the human head. *Annals of biomedical engineering*, 42(1):11–24.

[Jin et al., 2011] Jin, X., Yang, K. H., and King, A. I. (2011). Mechanical properties of bovine pia–arachnoid complex in shear. *Journal of biomechanics*, 44(3):467–474.

[Klug et al., 2013] Klug, C., Sinz, W., Brenn, G., and Feist, F. (2013). Experimental sphere in sphere testing for the validation of a numerical cerebrospinal fluid model. *IRCOBI, Gothenburg*, pages 483–496.

[Koobus and Farhat, 1999] Koobus, B. and Farhat, C. (1999). Second-order time-accurate and geometrically conservative implicit schemes for flow computations on unstructured dynamic meshes. *Computer Methods in Applied Mechanics and Engineering*, 170(1):103–129.

[Küttler and Wall, 2008] Küttler, U. and Wall, W. A. (2008). Fixed-point fluid–structure interaction solvers with dynamic relaxation. *Computational Mechanics*, 43(1):61–72.

[La Mantia, 2012] La Mantia, Mand Dabnichki, P. (2012). Added mass effect on flapping foil. *Engineering Analysis with Boundary Elements*, 36(4):579–590.

[Lesoinne and Farhat, 1996] Lesoinne, M. and Farhat, C. (1996). Geometric conservation laws for flow problems with moving boundaries and deformable meshes, and their impact on aeroelastic computations. *Computer methods in applied mechanics and engineering*, 134(1):71–90.

[Leveque and Li, 1994] Leveque, R. J. and Li, Z. (1994). The immersed interface method for elliptic equations with discontinuous coefficients and singular sources. *SIAM Journal on Numerical Analysis*, 31(4):1019–1044.

[LeVeque and Li, 1997] LeVeque, R. J. and Li, Z. (1997). Immersed interface methods for stokes flow with elastic boundaries or surface tension. *SIAM Journal on Scientific Computing*, 18(3):709–735.

[Li et al., 2016] Li, L., Henshaw, W., Banks, J., Schwendeman, D., and Main, A. (2016). A stable partitioned fsi algorithm for incompressible flow and deforming beams. *Journal of computational Physics*.

[Li and Lai, 2001] Li, Z. and Lai, M.-C. (2001). The immersed interface method for the navier–stokes equations with singular forces. *Journal of Computational Physics*, 171(2):822–842.

[Liu et al., 2014] Liu, J., Jaiman, R. K., and Gurugubelli, P. S. (2014). A stable second-order scheme for fluid–structure interaction with strong added-mass effects. *Journal of Computational Physics*, 270:687–710.

[Liu et al., 2009] Liu, K., VanLandingham, M. R., and Ovaert, T. C. (2009). Mechanical characterization of soft viscoelastic gels via indentation and optimization-based inverse finite element analysis. *Journal of the Mechanical Behavior of Biomedical Materials*, 2(4):355–363.

[Lombardi et al., 2013] Lombardi, M., Parolini, N., and Quarteroni, A. (2013). Radial basis functions for inter-grid interpolation and mesh motion in fsi problems. *Computer Methods in Applied Mechanics and Engineering*, 256:117–131.

[Ma et al., 2010] Ma, J., Wittek, A., Singh, S., Joldes, G. R., Washio, T., Chinzei, K., and Miller, K. (2010). Accuracy of non-linear fe modelling for surgical simulation: study using soft tissue phantom. In *Computational Biomechanics for Medicine*, pages 29–41. Springer.

[Ma et al., 2015] Ma, R., Chang, X., Zhang, L., He, X., and Li, M. (2015). On the geometric conservation law for unsteady flow simulations on moving mesh. *Procedia Engineering*, 126:639–644.

[Mangani and Bianchini, 2007] Mangani, L. and Bianchini, C. (2007). Heat transfer applications in turbomachinery. In *Proceedings of the OpenFOAM International Conference*.

[Marchi et al., 2009] Marchi, C. H., Suero, R., and Araki, L. K. (2009). The lid-driven square cavity flow: numerical solution with a 1024 x 1024 grid. *Journal of the Brazilian Society of Mechanical Sciences and Engineering*, 31(3):186–198.

[Margolin, 1997] Margolin, L. (1997). Introduction to " an arbitrary lagrangian–eulerian " computing method for all flow speeds. *Journal of Computational Physics*, 135(2):198–202.

[Matthies et al., 2006] Matthies, H. G., Niekamp, R., and Steindorf, J. (2006). Algorithms for strong coupling procedures. *Computer methods in applied mechanics and engineering*, 195(17):2028–2049.

[Matthies and Steindorf, 2002] Matthies, H. G. and Steindorf, J. (2002). Partitioned but strongly coupled iteration schemes for nonlinear fluid–structure interaction. *Computers & structures*, 80(27):1991–1999.

[Mayeur, 2013] Mayeur, O. (2013). *Personnalisation géométrique et mécanique multi-échelles du thorax humain*. PhD thesis, Université de Valenciennes et du Hainaut-Cambresis.

[Michler et al., 2004] Michler, C., Hulshoff, S. J., van Brummelen, E. H., and de Borst, R. (2004). A monolithic approach to fluid structure interaction. *Computers & Fluids*, 33:839–848.

[Mihalik et al., 2012] Mihalik, J. P., Guskiewicz, K. M., Marshall, S. W., Blackburn, J. T., Cantu, R. C., and Greenwald, R. M. (2012). Head impact biomechanics in youth hockey: comparisons across playing position, event types, and impact locations. *Annals of biomedical engineering*, 40(1):141–149.

[Miller, 2005] Miller, K. (2005). Method of testing very soft biological tissues in compression. *Journal of biomechanics*, 38(1):153–158.

[Misra et al., 2007] Misra, S., Okamura, A. M., and Ramesh, K. (2007). Force feedback is noticeably different for linear versus nonlinear elastic tissue models. In *EuroHaptics Conference, 2007 and Symposium on Haptic Interfaces for Virtual Environment and Teleoperator Systems. World Haptics 2007. Second Joint*, pages 519–524. IEEE.

[Mittal and Iaccarino, 2005] Mittal, R. and Iaccarino, G. (2005). Immersed boundary methods. *Annu. Rev. Fluid Mech.*, 37:239–261.

[Moerman et al., 2009] Moerman, K. M., Holt, C. A., Evans, S. L., and Simms, C. K. (2009). Digital image correlation and finite element modelling as a method to determine mechanical properties of human soft tissue in vivo. *Journal of biomechanics*, 42(8):1150–1153.

[Mok and Wall, 2001] Mok, D. and Wall, W. (2001). Partitioned analysis schemes for the transient interaction of incompressible flows and nonlinear flexible structures. *Trends in computational structural mechanics, Barcelona*.

[Morriss et al., 2008] Morriss, L., Wittek, A., and Miller, K. (2008). Compression testing of very soft biological tissues using semi-confined configuration—a word of caution. *Journal of biomechanics*, 41(1):235–238.

[Neishlos et al., 1981] Neishlos, H., Israeli, M., and Kivity, Y. (1981). Stability of some explicit difference schemes for fluid-structure interaction problems. *Computers & Structures*, 13(1):97–101.

[Ogden, 1972] Ogden, R. (1972). Large deformation isotropic elasticity-on the correlation of theory and experiment for incompressible rubberlike solids. In *Proceedings of the Royal Society of London A: Mathematical, Physical and Engineering Sciences*, volume 326, pages 565–584. The Royal Society.

[Palchesko et al., 2012] Palchesko, R. N., Zhang, L., Sun, Y., and Feinberg, A. W. (2012). Development of polydimethylsiloxane substrates with tunable elastic modulus to study cell mechanobiology in muscle and nerve. *PloS one*, 7(12):e51499.

[Pasquariello et al., 2016] Pasquariello, V., Hammerl, G., Örley, F., Hickel, S., Danowski, C., Popp, A., Wall, W. A., and Adams, N. A. (2016). A cut-cell finite volume–finite element coupling approach for fluid–structure interaction in compressible flow. *Journal of Computational Physics*, 307:670–695.

[Patankar and Spalding, 1972] Patankar, S. V. and Spalding, D. B. (1972). A calculation procedure for heat, mass and momentum transfer in three-dimensional parabolic flows. *International journal of heat and mass transfer*, 15(10):1787–1806.

[Peskin, 1972] Peskin, C. S. (1972). Flow patterns around heart valves: a numerical method. *Journal of computational physics*, 10(2):252–271.

[Peskin and Printz, 1993] Peskin, C. S. and Printz, B. F. (1993). Improved volume conservation in the computation of flows with immersed elastic boundaries. *Journal of computational physics*, 105(1):33–46.

[Piperno et al., 1995] Piperno, S., Farhat, C., and Larrouturou, B. (1995). Partitioned procedures for the transient solution of coupled aroelastic problems part i: Model problem, theory and two-dimensional application. *Computer methods in applied mechanics and engineering*, 124(1):79–112.

[Qiang et al., 2011] Qiang, B., Greenleaf, J., Oyen, M., and Zhang, X. (2011). Estimating material elasticity by spherical indentation load-relaxation tests on viscoelastic samples of finite thickness. *IEEE transactions on ultrasonics, ferroelectrics, and frequency control*, 58(7):1418–1429.

[Rajaratnam and Nwachukwu, 1983] Rajaratnam, N. and Nwachukwu, B. A. (1983). Flow near groin-like structures. *Journal of Hydraulic Engineering*, 109(3):463–480.

[Ramm et al., 1998] Ramm, E., Wall, W., and in der Kontinuumsmechanik;, S. U. S. .-M. (1998). Fluid-structure interaction based upon a stabilized (ale) finite element method. In *4th World Congress on Computational Mechanics: New Trends and Applications, CIMNE, Barcelona*, pages 1–20.

[Razzaq, 2011] Razzaq, M. (2011). *Finite element simulation techniques for incompressible fluid structure interaction with applications to bioengineering and optimization*. PhD thesis.

[Ricard et al., 2010] Ricard, C., Claudet, I., and Lasbeur, L. (2010). Enquête permanente sur les accidents de la vie courante. *Maladies chroniques et traumatismes*.

[Rivlin, 1948] Rivlin, R. (1948). Large elastic deformations of isotropic materials. iv. further developments of the general theory. *Philosophical Transactions of the Royal Society of London A: Mathematical, Physical and Engineering Sciences*, 241(835):379–397.

[Roberts et al., 2012] Roberts, J., Harrigan, T., Ward, E., Taylor, T., Annett, M., and Merkle, A. (2012). Human head–neck computational model for assessing blast injury. *Journal of Biomechanics*, 45(16):2899–2906.

[Rungen, 2004] Rungen, P. (2004). *Enrichissement des modèles physique et numérique de la tête en vue de mieux représenter la cinématique cérébrale lors d'un choc*. PhD thesis, Valenciennes.

[Ryzhakov et al., 2010] Ryzhakov, P. B., Rossi, R., Idelsohn, S. R., and Onate, E. (2010). A monolithic Lagrangian approach for fluid structure interaction problems. *Computational Mechanics*, 46:883–899.

[Saboori and Sadegh, 2011] Saboori, P. and Sadegh, A. (2011). Material modeling of the head's subarachnoid space. *Scientia Iranica*, 18(6):1492–1499.

[Salathé and Rosseau, 2015] Salathé, M. and Rosseau, T. (2015). La sécurité routiè en france. Technical report, Observatoire national interministériel de la sécurité routière.

[Samuelides and Frieze, 1989] Samuelides, E. and Frieze, P. (1989). Fluid-structure interaction in ship collisions. *marine Structures*, 2(1):65–88.

[Schwarz et al., 2016] Schwarz, S., Kempe, T., and Fröhlich, J. (2016). An immersed boundary method for the simulation of bubbles with varying shape. *Journal of Computational Physics*, 315:124–149.

[Seo and Mittal, 2011] Seo, J. H. and Mittal, R. (2011). A sharp-interface immersed boundary method with improved mass conservation and reduced spurious pressure oscillations. *Journal of computational physics*, 230(19):7347–7363.

[Shangguan and Lu, 2004] Shangguan, W.-B. and Lu, Z.-H. (2004). Experimental study and simulation of a hydraulic engine mount with fully coupled fluid–structure interaction finite element analysis model. *Computers & Structures*, 82(22):1751–1771.

[Smith et al., 2000] Smith, M. J., Cesnik, C. E., and Hodges, D. H. (2000). Evaluation of some data transfer algorithms for noncontiguous meshes. *Journal of Aerospace Engineering*, 13(2):52–58.

[Söding, 2001] Söding, H. (2001). How to integrate free motions of solids in fluids. In *4th Numerical Towing Tank Symposium, Hamburg*.

[Song et al., 2013] Song, M., Lefrançois, E., and Rachik, M. (2013). A partitioned coupling scheme extended to structures interacting with high-density fluid flows. *Computers & Fluids*, 84:190–202.

[Sterenborg et al., 2014] Sterenborg, J., van Zuijlen, A., and Bijl, H. (2014). Experimental benchmark of a free plunging wing with imposed flap oscillations. *Journal of Fluids and Structures*, 49:338–359.

[Suliman et al., 2015] Suliman, R., Oxtoby, O. F., Malan, A., and Kok, S. (2015). A matrix free, partitioned solution of fluid–structure interaction problems using finite volume and finite element methods. *European Journal of Mechanics-B/Fluids*, 49:272–286.

[Thomas and Lombard, 1979] Thomas, P. and Lombard, C. (1979). Geometric conservation law and its application to flow computations on moving grids. *AIAA journal*, 17(10):1030–1037.

[Thomas et al., 2015] Thomas, R. F., Debra, H., and Grant, B. (2015). Report to congress on traumatic brain injury in the united states: Epidemiology and rehabilitatio. Technical report, Centers for Disease Control and Prevention.

[Toohey et al., 2016] Toohey, K., Kalyanam, S., Palaniappan, J., and Insana, M. (2016). Indentation analysis of biphasic viscoelastic hydrogels. *Mechanics of Materials*, 92:175–184.

[Troshin et al., 2015] Troshin, V., Seifert, A., Sidilkover, D., and Tadmor, G. (2015). Proper orthogonal decomposition of flow-field in non-stationary geometry. *Bulletin of the American Physical Society*, 60.

[Tseng and Ferziger, 2003] Tseng, Y.-H. and Ferziger, J. H. (2003). A ghost-cell immersed boundary method for flow in complex geometry. *Journal of computational physics*, 192(2):593–623.

[Ucar et al., 2006] Ucar, T., Tanriover, G., Gurer, I., Onal, M. Z., and Kazan, S. (2006). Modified experimental mild traumatic brain injury model. *Journal of Trauma and Acute Care Surgery*, 60(3):558–565.

[Udaykumar et al., 2001] Udaykumar, H., Mittal, R., Rampunggoon, P., and Khanna, A. (2001). A sharp interface cartesian grid method for simulating flows with complex moving boundaries. *Journal of Computational Physics*, 174(1):345–380.

[Vandenbulcke, 2015] Vandenbulcke, F. (2015). *Caractérisation et modélisation multi-échelle du comportement mécanique à la rupture du membre scapulaire sous sollicitations dynamiques*. PhD thesis, Université de Valenciennes et du Hainaut-Cambresis.

[Wall, 1999] Wall, W. A. (1999). *Fluid-struktur-interaktion mit stabilisierten finiten elementen*. PhD thesis, Institut für Baustatik, Universität Stuttgart.

[Wall et al., 1999] Wall, W. A., Mok, D. P., and Ramm, E. (1999). Partitioned analysis approach of the transient coupled response of viscous fluids and flexible structures. In *Solids, structures and coupled problems in engineering, proceedings of the European conference on computational mechanics ECCM*, volume 99.

[Wick, 2013] Wick, T. (2013). Coupling of fully eulerian and arbitrary lagrangian–eulerian methods for fluid-structure interaction computations. *Computational Mechanics*, 52(5):1113–1124.

[Wick, 2014] Wick, T. (2014). Flapping and contact fsi computations with the fluid–solid interface-tracking/interface-capturing technique and mesh adaptivity. *Computational Mechanics*, 53(1):29–43.

[Winslow, 1963] Winslow, A. (1963). Equipotential zoning of two-dimentional meshes. *Lawrence Livermore Laboratory*, Report UCRL-7312.

[Wood et al., 2010] Wood, C., Gil, A., Hassan, O., and Bonet, J. (2010). Partitioned block-gauss–seidel coupling for dynamic fluid–structure interaction. *Computers & structures*, 88(23):1367–1382.

[Wu and Lin, 2015] Wu, W. and Lin, Q. (2015). A 3-d implicit finite-volume model of shallow water flows. *Advances in Water Resources*, 83:263–276.

[Xu and Wang, 2006] Xu, S. and Wang, Z. J. (2006). An immersed interface method for simulating the interaction of a fluid with moving boundaries. *Journal of Computational Physics*, 216(2):454–493.

[Yan and Pangestu, 2011] Yan, W. and Pangestu, O. D. (2011). A modified human head model for the study of impact head injury. *Computer methods in biomechanics and biomedical engineering*, 14(12):1049–1057.

[Ye et al., 1999] Ye, T., Mittal, R., Udaykumar, H., and Shyy, W. (1999). An accurate cartesian grid method for viscous incompressible flows with complex immersed boundaries. *Journal of computational physics*, 156(2):209–240.

[Yu, 2005] Yu, Z. (2005). A dlm fd method for fluid flexible body interactions. *Journal of Computational Physics*, 207(1):1–27.

[Yvin, 2014] Yvin, C. (2014). *Interaction fluide-structure pour des configurations multi-corps. Applications aux liaisons complexes, lois de commande d'actionneur et systemes souples dans le domaine maritime.* PhD thesis.

[Zeng and Scovazzi, 2016] Zeng, X. and Scovazzi, G. (2016). A variational multiscale finite element method for monolithic ale computations of shock hydrodynamics using nodal elements. *Journal of Computational Physics*, 315:577–608.

[Zilliacus, 2014] Zilliacus, S. (2014). Fluid-structure interaction and adina. *Comput Struct. v17*, pages 763–773.

[Zoghi-Moghadam and Sadegh, 2010] Zoghi-Moghadam, M. and Sadegh, A. M. (2010). Equivalent fluid model for csf and sas trabeculae using head/brain damping. *International Journal of Biomedical Engineering and Technology*, 4(3):195–210.